Evaluation of the Load-Bearing Mechanisms in Coupling Beams and Shear Walls based on DICMeasurements

Auteur : Langer, Mathias
Promoteur(s) : Mihaylov, Boyan
Faculté : Faculté des Sciences appliquées
Diplôme : Master en ingénieur civil des constructions, à finalité
Année académique : 2018-2019
URI/URL : http://hdl.handle.net/2268.2/6753

Université de Liège - Faculté des Sciences Appliquées

Année académique 2018-2019

Evaluation of the Load-Bearing Mechanisms in Coupling Beams and Shear Walls based on DIC Measurements

Travail de fin d'études réalisé en vue de l'obtention du grade de Master en Ingénieur Civil des Constructions par Mathias Langer

Jury:
B. I. Mihaylov - ULiège (supervisor)
V. Denoël - ULiège
J.-P. Jaspart - ULiège
S. Bousias - University of Patras, Greece

Acknowledgments

I would like to thank several people that accompanied me during the last four months.

First of all, I would like to express my gratitude to my adviser Boyan Mihaylov for having introduced me to the topic. He helped me all along with a lot of useful comments, sometimes philosophical citations, remarks and encouragement. He was always available for discussions and advises.
Furthermore, I would like to thank Renaud Franssen, who introduced me to his PhD work and his experimental program.
I also thank the Construction Engineering Research Group of Hasselt University, especially Hervé Degée and Dan Dragan, whom the material and support for the tests in University of Liège have been hired from.
In addition, I would like to thank the University of Patras (Greece), in particular the Structures Laboratory team with Stathis Bousias and Elias Strepelias of the Civil Engineering Department for their collaboration, especially the executing of the experiments on coupling beams and the processing of the experimental data.
I also thank the other jury members for their interest and attention.

I am also grateful for the overall good atmosphere in the department, especially the encouragement and the sorrow sharing among colleagues.

A special thank goes to my loved ones, especially Franca, my parents and brother and sister, who have supported me throughout the last 4 months, who endured my moods and worries and who always believed in me. Without their support, I would not have achieved the final result.

Abstract

Title	Evaluation of the Load-Bearing Mechanisms in Coupling Beams and Shear Walls Based on DIC Measurements
Author	Mathias Langer, Master Ingénieur Civil des Constructions
Academic year	2018-2019
Adviser	Boyan I. Mihaylov

This work presents two applications of Digital Image Correlation in tests on short coupling beams and shear walls. This type of reinforced concrete members are typically subjected to high shear forces and are susceptible to shear failures along diagonal cracks.

The general principles of DIC and their practical application are studied and described. Based on DIC analysis, the kinematics of the two reinforced concrete members are illustrated and compared to a two-degree-of-freedom kinematic model for short coupling beams and to a three-degree-of-freedom kinematic model for shear-dominated walls in order to assess their performance. It is shown that the kinematic model underestimates the deformations of the beam, while the wall's deformation patterns are well predicted.

Methods to evaluate the load-bearing mechanisms based on DIC are also presented. For aggregate interlock, three different crack models are used to determine the shear transferred through the critical crack based on crack opening and slip. The shear carried by the critical loading zone is evaluated through constitutive stress-strain relations for the concrete. It is shown that sum of all contributions from shear mechanisms gives a shear force of the same order of magnitude as the measured applied shear force. In the coupling beam, about 45% of the applied shear force is estimated to be resisted by transverse reinforcement, 35% by the critical loading zones, and 20% is transferred through aggregate interlock. The shear wall was only provided with a few stirrups and their contribution was only about 16%, the aggregate interlock contribution was 8%, while the critical loading zone carried about 76% of the applied shear force. These results represent a first valuable insight into how shear is shared among different mechanisms and can be used to inform and improve models for the shear behavior of non-slender reinforced concrete members.

Résumé

Titre	Étude des méchanismes de résistance dans des poutres de couplage et des murs de cisaillement grâce à des mesures DIC.
Auteur	Mathias Langer, Master Ingénieur Civil des Constructions
Année académique	2018-2019
Promoteur	Boyan I. Mihaylov

Ce travail présente l'application de la méthode "Digital Image Correlation" sur un essai sur une poutre de couplage courte (short coupling beam) et sur un essai sur un mur de cisaillement (shear wall). Ces éléments en béton armé sont typiquement soumis à des forces de cisaillement importantes et peuvent subir des ruptures par cisaillement le long de fissures diagonales.

Les principes généraux de DIC et leur application sont étudiés et présentés. Les cinématiques des deux éléments en béton armé, basées sur DIC, sont illustrées et comparées à un modèle cinématique à deux degrés de liberté pour la poutre de couplage et à un modèle à trois degrés de liberté pour des murs de cisaillement afin d'évaluer leur performance. On montre que le modèle cinématique sous-estime les déformations de la poutre, tandis que la déformation du mur est bien prédite.

Des méthodes pour quantifier des mécanismes de résistance à partir de mesures DIC sont également présentées. En ce qui concerne l'imbrication des granulats dans les fissures, trois modèles sont utilisés pour déterminer, à partir de l'ouverture de la fissure et de son glissement, le transfert de cisaillement à travers la fissure critique. Le transfert de cisaillement dans la zone critique de chargement est évalué sur base de relations constitutives contrainte-déformation du béton. Il est montré que la somme des contributions des différents mécanismes est du même ordre de grandeur que la force de cisaillement appliquée. Pour la poutre de couplage, 45% de la force appliquée est estimée reprise par les étriers, 35% par la zone critique de chargement et 20% par la fissure critique grâce à l'imbrication des granulats. Le mur de cisaillement contenait seulement une petite quantité d'étriers de sorte que le cisaillement repris par ces armatures transversales n'était que de 16%. L'imbrication des granulats contribue pour 8% à la résistance au cisaillement et les 76% restants sont repris par la zone critique de chargement. Ces résultats donnent une première idée concrète de la répartition du cisaillement entre les différents mécanismes de résistance. Les modèles décrivant le comportement en cisaillement des éléments non-élancés peuvent être améliorés sur base de ces résultats.

Contents

1 Introduction **19**
- 1.1 Short coupling beams in buildings . . . 19
- 1.2 Short shear walls . . . 19
- 1.3 Shear mechanisms in coupling beams and walls . . . 19
- 1.4 DIC background . . . 21
  - 1.4.1 Setup . . . 23
  - 1.4.2 Processing . . . 24
  - 1.4.3 Strain calculation . . . 24
- 1.5 Thesis objectives . . . 25
- 1.6 Thesis outline . . . 25

2 Experimental campaigns & DIC systems **27**
- 2.1 Test on shear wall . . . 27
  - 2.1.1 Test specimen . . . 27
  - 2.1.2 DIC system . . . 30
- 2.2 Test on coupling beam . . . 36
  - 2.2.1 Test specimen . . . 36
  - 2.2.2 DIC system . . . 42

3 Shear behavior of short coupling beams and walls **43**
- 3.1 Deformation patterns . . . 43
  - 3.1.1 2PK model for short coupling beams . . . 43
  - 3.1.2 3PK model for walls . . . 45
- 3.2 Shear mechanisms . . . 47
  - 3.2.1 Critical loading zone . . . 49
  - 3.2.2 Aggregate interlock . . . 56
  - 3.2.3 Stirrups . . . 65

4 Results: Short Wall **67**
- 4.1 Global observed behavior . . . 68
- 4.2 Validation of DIC measurements . . . 73
  - 4.2.1 Processing of DIC data . . . 73
  - 4.2.2 Comparison with DT and LED measurements . . . 74
- 4.3 Comparison with kinematic model . . . 79
  - 4.3.1 Processing of DIC data . . . 79
  - 4.3.2 Measured geometry and DOFs of kinematic model . . . 80
  - 4.3.3 Comparison of displacement fields . . . 81
  - 4.3.4 Comparison of crack displacements . . . 87
- 4.4 Mechanisms of shear resistance . . . 88

4.4.1 Aggregate interlock . . . 88
4.4.2 Critical loading zone . . . 91
4.4.3 Stirrups . . . 97
4.4.4 Total shear force . . . 97

5 Results: Coupling Beam **99**
5.1 Global observed behavior . . . 99
5.2 Validation of DIC measurements . . . 100
5.2.1 Processing of DIC data . . . 103
5.2.2 Comparison with DT measurements . . . 107
5.3 Comparisons with kinematic model . . . 112
5.3.1 Measured geometry and DOFs of kinematic model . . . 113
5.3.2 Comparison of displacement fields . . . 113
5.3.3 Comparison of crack displacements . . . 115
5.4 Mechanisms of shear resistance . . . 117
5.4.1 Aggregate interlock . . . 117
5.4.2 Critical loading zone . . . 120
5.4.3 Stirrups . . . 124
5.4.4 Total shear force . . . 125

6 Conclusion **127**
6.1 Future work . . . 129

A Crack kinematics methodology **131**

List of Figures

1.1 Entire coupled wall system. 20
1.2 Shear failure of a short coupling beam. 20
1.3 Bridge with wall-type pier. 21
1.4 Shear failure of a pier. 22
1.5 Free-body equilibrium and internal forces in a cantilever (without transverse reinforcement) subjected to a point load Q. V_{agg} = aggregate interlock contribution, V_{RS} = concrete residual strength contribution, V_C = compression chord and arching action, $V_{D,tens.}$ = dowelling action (Cavagnis, Ruiz, & Muttoni, 2018). 22

2.1 Longitudinal reinforcement. 27
2.2 Transverse reinforcement. The stirrups in the test had a diameter of 8 mm. 28
2.3 Test setup. 29
2.4 Instrumentation (DT sensors, LED targets) of the wall, with tension side view. 30
2.5 Instrumentation (DT sensors, LED targets) of the wall, with compression side view. 31
2.6 Experimental setup of DIC. 31
2.7 Recorded picture during the calibration process. 33
2.8 Step 1 of calibration process : Define experimental setup. 33
2.9 Comparison between raw and corrected image. 34
2.10 Strain uncertainties for different subset sizes (colorscale ranging from -0.00024 to 0.00097). 36
2.11 Geometry of test specimen. 37
2.12 Reinforcement of specimen. 38
2.13 Global view of the test setup. 39
2.14 Planned instrumentation of the coupling beam. 40
2.15 Implemented instrumentation of the coupling beam. 41
2.16 Photographs from the experimental setup (front view). 41
2.17 Instrumentation on the back face (without speckles) of the specimen. 42

3.1 Two-parameter kinematic model for short coupling beams (B. Mihaylov, Liu, & Lobet, 2018). 44
3.2 2PK model for coupling beams. 44
3.3 3PK model for shear-dominated walls. (a) DOF $\varepsilon_{t,avg}$; (b) DOF Δ_c; (c) DOF Δ_{cx}; (d) deformed shape (B. I. Mihaylov, Hannewald, & Beyer, 2016). 47

3.4 Shear mechanisms in short coupling beams. V_{ci} = aggregate interlock; V_{CLZ} = shear carried in critical loading zone; V_d = dowel action of longitudinal reinforcement; V_s = tension in the stirrups (B. Mihaylov, Liu, & Lobet, 2018). 47
3.5 Free-body diagram with applied horizontal shear force and horizontal components of internal stresses. 48
3.6 Free-body equilibrium and internal forces in a RC member (Cavagnis, Ruiz, & Muttoni, 2018). 49
3.7 Schematic of typical stress state close to CLZ. σ_1 (maximum principal stress) and σ_2 (minimum principal stress) acting along principal stress directions. τ_{xy} (shear stress) and σ_y (normal stress) acting on horizontal plane. 50
3.8 Constant Strain Triangle (Ponthot, 2016). 50
3.9 Mohr's Circle representation (left) for a general strain state in x-y coordinates (right). Source : https://www.efunda.com/formulae/solid_mechanics/mat_mechanics/mohr_circle_usage_strain.cfm 52
3.10 Comparison between general axis (X-Y) and principal axis (Xp-Yp). Source : https://www.efunda.com/formulae/solid_mechanics/mat_mechanics/mohr_circle_usage_strain.cfm 52
3.11 (a) Stress-strain diagram for concrete; (b) Kupfer's failure criterion (Kupfer, Hilsdorf, & Rusch, 1969) and adopted one (Cavagnis, Ruiz, & Muttoni, 2018). 55
3.12 Different laws used for $f_{c,eff}$ in function of the principal tensile strain for $f_c = 30\ MPa$. The biaxial failure criterion refers to the simplified bilinear law based on Kupfer's failure surface, the uniaxial compression law refers to Popovics (1973) and the compression softening law refers to Vecchio and Collins (1986). 56
3.13 Mohr's circle representation of a stress state. Source: https://www.efunda.com/formulae/solid_mechanics/mat_mechanics/mohr_circle_usage.cfm 57
3.14 Aggregate interlock stresses: normal stresses σ_{ag} and tangential stresses τ_{ag}. 57
3.15 Grid of targets in experimental setups (Campana, Anastasi, Ruiz, & Muttoni, 2013), cropped. 58
3.16 Calculation of crack kinematics; (a) undeformed configuration; (b) deformed configuration. 59
3.17 (a) Contact zone between aggregate and cement matrix and aggregate interlock stresses; (b) Projections areas according to the kinematics proposed by Walraven (Cavagnis, Ruiz, & Muttoni, 2018). 60
3.18 Definitions and notations of the CDM (Li, Maekawa, & Okamura, 1989). 61
3.19 Contact density of each direction (Li, Maekawa, & Okamura, 1989). . 62
3.20 Effective ratio of contact area K, model and measured (Li, Maekawa, & Okamura, 1989). 62
3.21 Relationship between shear stress v_{ci} and normal stress f_{ci} (Calvi, Bentz, & Collins, 2017). 64
3.22 Free-body diagram of aggregate at contact point at loading (Calvi, Bentz, & Collins, 2017). 64

3.23 Relationship between crack geometry and crack stresses (Calvi, Bentz, & Collins, 2017). 65
3.24 Interlock stresses (shear stress τ defined positive, compressive normal stress σ defined negative) according to the the Pure Mechanics Crack Model (PMCM), Contact Density Model (CDM) and Two-Phase Model (TPM) in function of slip and crack width (w). Maximum aggregate size = 16 mm, concrete compressive strength f_c = 30 MPa. 66

4.1 Evolution of applied horizontal load. 68
4.2 Load-displacement curve. 69
4.3 Crack pattern at two different load steps. 70
4.4 Pictures taken by DIC system before, during and after failure, within a span of 1,5 seconds. The top and bottom photographs correspond to the camera focusing respectively on the top and bottom part of the wall. 71
4.5 Specimen after failure. 72
4.6 Location of points used to compare DIC measurements to DT measurements. 74
4.7 Numbering of LED targets. 75
4.8 LED target positions on theoretical position grid. 76
4.9 Comparison between DIC (subset = 51 px, step = 13 px), DT and LED at load step B9, before failure, in absolute values. 78
4.10 Longitudinal reinforcement of the wall. 80
4.11 Deformation patterns at peak. 82
4.12 Secondary movements accounted for in DIC. From left to right: initial position, slip foundation-floor, slip at interface wall-foundation, pull-out, rotation of foundation. 83
4.13 Vertical strains ε_y with a colorbar representing negative values (compression) in black. 84
4.14 Deformation patterns at peak. 85
4.15 Comparison of displacement fields at peak (deformed positions of DIC subtracted by deformed positions of kinematic model). 86
4.16 Free-body diagram of a wall with applied horizontal shear force and horizontal components of internal stresses. 88
4.17 Zoom on crack (plot of maximum principal strain). $*$ = end points of crack, + = crack point, bullets in blue, green, red, yellow = P1 to P4. 89
4.18 Crack width (white) and slip (red) [mm]. 90
4.19 Stress contributions to total shear force transferred in the crack for PMCM model. 91
4.20 Maximum principal strains. 92
4.21 Principal strains in disturbed area (CLZ) at the bottom left of the wall. 93
4.22 Shear stresses τ_{xy} for V_{CLZ}, based on the biaxial failure criterion. . . . 93
4.23 Maximum principal strains ε_1 in zone, with $\varepsilon_1 \geq \varepsilon_{cr}$ being colored in black. 94
4.24 Evolution of V_{CLZ} along the y-axis according to the 3 proposed models. 95

4.25 Principal stresses ($\sigma_1 = s1$ and $\sigma_2 = s2$) and horizontal shear stress $\tau_{xy} = txy$ at plane of maximum V_{CLZ} according to compression-softening model. 95
4.26 Principal compressive strain/stress directions in CLZ. 96

5.1 Load-displacement response of the short coupling beam. 100
5.2 Test specimen (opposite side of DIC frame) at a horizontal load of 452 kN and a horizontal displacement of 6.74 mm. 101
5.3 Last photograph of the time-lapse (end of test) at a horizontal load of 312 kN and a horizontal displacement of 24.1 mm. 102
5.4 Mean vertical displacement of top block. 102
5.5 Region of interest within the dimensions of the specimen (black lines). 103
5.6 Relative displacement of two data points (DIC) representing the sensor POT66. 105
5.7 Horizontal displacement field before and after discontinuity. 106
5.8 Effect of filtering DIC data in the post-peak region. The deformation corresponds to the relative displacement between two points on either side of the crack. 107
5.9 Implemented instrumentation of the coupling beam. 108
5.10 Comparison between DT and DIC for POT66. 108
5.11 Comparison between DT and DIC for POT59. 109
5.12 Comparison between DT and DIC for the web expansion. 110
5.13 Comparison between DT and DIC for SPR-POT5. 110
5.14 Comparison of absolute vertical displacement of point below crack, between DT and DIC. 111
5.15 Displacement fields at peak. 112
5.16 Deformation patterns at peak. 114
5.17 Secondary movements accounted for in DIC. From left to right: initial position, slip bottom block-floor, slip at interface beam-bottom block, pull-out. 115
5.18 Deformation patterns at peak. 116
5.19 Comparison of displacement fields at peak (deformed positions of DIC subtracted by deformed positions of kinematic model). 116
5.20 Possible missing deformation in 2PKT. 117
5.21 Free-body diagram with applied horizontal shear force and horizontal components of internal stresses. 118
5.22 Crack width and slip computed from DIC at peak. 119
5.23 Stress contributions to total shear force transferred in the crack for CDM model. 120
5.24 Strain fields. 121
5.25 ε_y strain field. Negative (compressive) strains are represented in black. 122
5.26 Test specimen (opposite side of DIC frame) close to peak force. . . . 122
5.27 Shear stresses τ_{xy} in the top right corner (left figure) and in the bottom left corner (right figure). 123
5.28 Evolution of shear in CLZ along height. 124
5.29 Evolution of shear in CLZ along height. 124

5.30 Stresses along chosen planes (max. principal strain s1 = σ_1; minimum principal strain s2 = σ_2; shear stress txy = τ_{xy}) computed with compression-softening law. 125

A.1 Modelled crack segment and rigid body displacement. The arrows are displacement vectors (e.g. output of DIC analysis). 132
A.2 Schematic for crack opening w and slip s calculation. 133

List of Tables

2.1 Properties of the shear wall. 29
2.2 Properties of the short coupling beam. 37

4.1 Mean deviation in percent [%] between DIC and DT data for different subsets (and steps) [px]. 79

Chapter 1

Introduction

1.1 Short coupling beams in buildings

Short coupling beams provide coupling of shear walls in coupled wall systems as illustrated in Fig. 1.1. They are commonly present due to openings in walls for windows and doors. Since they typically feature small aspect ratios (a/h, with a being the shear span and h being the depth of the beam), they are referred to as *short* coupling beams. Their application in coupled wall structures results in a stiff system with large lateral resistance. Consequently they work in double curvature with high shear stresses. Therefore, they are susceptible to shear failures. An example of a failure of a coupling beam is shown in Fig. 1.2. Since their aspect ratio is small, they can be considered as deep members and the classical plane-sections-remain-plane hypothesis does not apply.

1.2 Short shear walls

Short shear walls are often used as wall-type bridge piers in bridges, as illustrated in Fig. 1.3.

They usually work under a combination of axial load and high shear. As a consequence, they are susceptible to brittle shear failures. Fig. 1.4 shows an example of such a failure. For this type of deep reinforced concrete member, the classical plane-sections-remain-plane hypothesis does not apply.

1.3 Shear mechanisms in coupling beams and walls

In order to sustain the applied shear force, different shear mechanisms are discussed in literature. The most discussed shear mechanisms are:

- Aggregate interlock
- Compression zone
- Dowel action
- Shear reinforcement

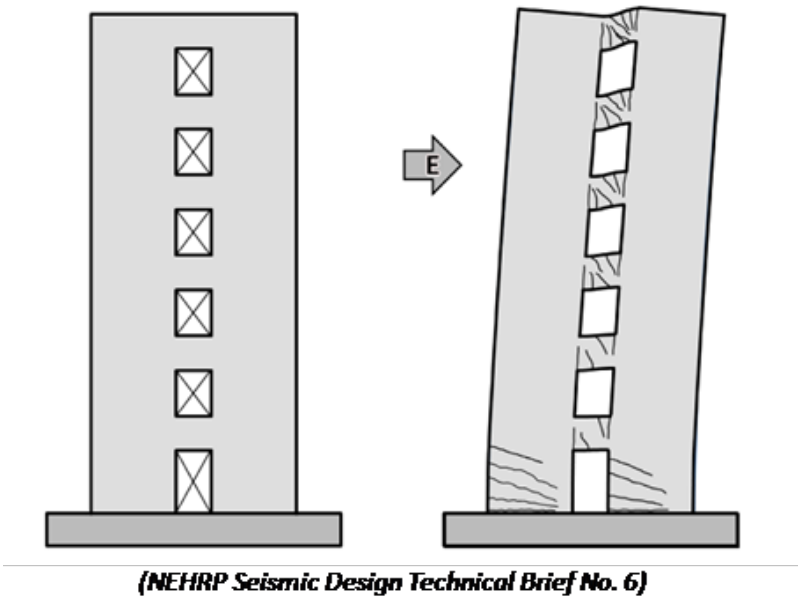

Figure 1.1: Entire coupled wall system.

Figure 1.2: Shear failure of a short coupling beam.

Figure 1.3: Bridge with wall-type pier.

For slender beams and walls many models exist considering one of these actions as governing. Few models account for a combination of mechanisms or all mechanisms. Cavagnis, Ruiz, and Muttoni (2018), for example, take into consideration all previously cited mechanisms as well as the residual tensile strength, as shown in a free-body diagram in Fig. 1.5. The ongoing discussion and the various propositions lead to the question: Which models are correct?

For short members, no model exists that accounts for all shear mechanisms except kinematic-based theory for coupling beams and walls. The kinematic model for coupling beams is referred to as 2PKT and the kinematic model for shear walls is referred to as 3PKT. They are based on 2 and 3 degrees of freedom respectively that describe a simplified deformation pattern.
There is a need for validation and refinement of the kinematics as well as for an experimental evaluation of shear mechanisms in order to possibly improve the model. Digital Image Correlation provides new possibilities for answering these questions.

1.4 DIC background

Digital Image Correlation (DIC) is a technique that is used to track deformations of a specimen under loading. This technique is typically used during tests in laboratories, where a specimen is loaded and the engineers are interested in the displacement field of the specimen.

Figure 1.4: Shear failure of a pier.

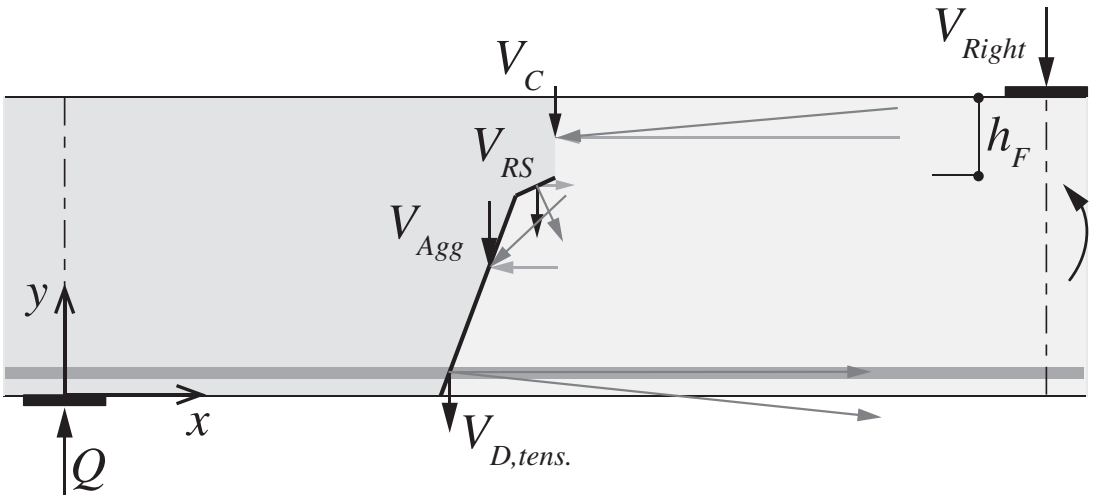

Figure 1.5: Free-body equilibrium and internal forces in a cantilever (without transverse reinforcement) subjected to a point load Q. V_{agg} = aggregate interlock contribution, V_{RS} = concrete residual strength contribution, V_C = compression chord and arching action, $V_{D,tens.}$ = dowelling action (Cavagnis, Ruiz, & Muttoni, 2018).

In order to get the displacement field as a function of time or loading, cameras must take photos at a certain frequency (e.g. 2 Hz) during the loading so that the evolution of the deformation is recorded.

DIC becomes more and more popular among researchers and a wide range of software is available, sharing the main principles. The technical development in terms of high resolution cameras as well as high storage hard drives enables scientists and engineers to use the technique for many applications at different scales.

General principles that are valid for most DIC applications are presented in the following.

1.4.1 Setup

Digital Image Correlation is nowadays a convenient way to follow a deformation during lab tests. The technique requires generally high resolution digital cameras to take a series of images and a computer to process and evaluate the data. It should be noted that the resulting data from DIC can be very large. First of all, depending on the duration of the test and the frequency of photograph recording, the number of photographs can be large. Furthermore, processed data requires a lot of space too. External hard drives are therefore required in many applications.

Based on the images, a software tries to track observable changes in those images in order to derive a displacement or deformation field. The DIC can only measure deformations on the surface of the element (Lavision, 2015).

The processing of the recorded photographs consists mainly in comparing the digital images at different stages of deformation. More precisely, blocks of pixels, defined by a "subset size", are defined in the reference image. The software tries to determine their respective locations in a deformed configuration, such that a displacement information is obtained.
One must make sure that the blocks are unique so that the processing works effectively. The common way to achieve random blocks of pixels is to create a random pattern on the specimen by producing dark, preferentially black, speckles of 3-5 pixels in size on a white surface in order to achieve a high contrast. The pattern should be non-repetitive, isotropic and high-contrast (Correlated Solutions, 2009).

DIC requires proper lighting and surface preparation. Therefore, dust particles on the camera chip as well as light reflections causing bright spots should be avoided. Those optical errors lead to undesired results. Generally speaking, the specimen should be lightened in the most uniform way, without causing dark shadows and leaving dark areas. Adapted light sources are needed.
Furthermore, heat waves must be avoided. They may distort the image, which can cause major errors in the results. Heat waves can be produced by hot objectives, but also by light sources. The choice of the type and amount of light source must be carefully chosen (Correlated Solutions, 2014a).

1.4.2 Processing

The processing of the photographs is performed based on a set of important notions and quantities. The most important DIC parameters commonly used in DIC software are the following:

- *Mask* : The mask defines the region of interest (ROI), the parts of the image that will be processed. The resulting displacement field is only defined in this region.
- *Seeding points/Seeds*: Those are points defined in the masks/ROI and represent starting points for the algorithm to determine the deformation.
- *Correlation mode*: It defines the reference for the deformation computation. The mode "relative to first" is commonly used. The deformation of each image is then calculated with respect to the first image of the sequence (Lavision, 2015).
- *Subset size*: The software assigns a mesh of small windows, called subsets, across the image. The subset size defines, in pixels, the size of those windows. To evaluate the displacement of a specific data point, the subset will be used to correctly locate the point in a deformed configuration.
  A clear recommendation for the subset size does not really exist. It can require some iterations to get this option right. The manual for the software tool *Ncorr* states that the smallest subset which does not lead to noisy displacement data should be chosen. Generally, larger subsets may have a smoothing effect (Blaber & Antoniou, 2017). However, larger subsets contain more information and are more unique. Subsets can also overlap, which makes them not completely independent from each other (Correlated Solutions, 2014b).
- *Step size*: The step size defines the grid spacing of the data points (Lavision, 2015). For most applications, a good rule of thumb is to choose the step size to be roughly 1/4 of the subset size, in order to get relatively independent and non-repetitive data (Correlated Solutions, 2014b).

1.4.3 Strain calculation

DIC software usually offers an option to compute strains. Strains involves differentiation. Strain calculation is thus very sensitive to noise. In fact, noise that is present in displacement fields will cause magnified errors in the strain field (Blaber & Antoniou, 2017). DIC software usually employ methods to avoid an amplification of noise during strain calculation.
Lavision (2015) and Correlated Solutions (2014b) describe in their documentation that smoothing filters are employed for this effect. A smoothing area can be selected in the parameters. In practice, if you use a small step size then you'll want to use a larger "strain filter", defining the "smoothing area". For a large step size a smaller strain filter is recommended (Correlated Solutions, 2014b).

The fundamental strain calculation in a software called *Vic-3D* uses an algorithm normally used in Finite Element Analysis software (Correlated Solutions, n.d.). For

each data point, 3 neighboring data points are used to compute strains. More precisely, with the surrounding data points, a local mesh of triangles is created and the the strain for one data point is obtained by interpolating the strain tensor of the triangles of interest. In case of small triangles, strain tensors are noisy and the smoothing should be applied. Those strains are smoothened using low-pass filters (Correlated Solutions, 2009).

Blaber and Antoniou (2017) compute strains from displacement data by using a least square plane fit to a group of data points. A strain calculation parameter is the radius of a circle including the data points to fit the plane to. By this method, displacement gradients are determined, which, in turn, are used in strain calculation.

In conclusion, strain calculation is a tricky operation, especially because differentiation leads to amplified noise. Different programs use different methods to deal with strain calculation.

1.5 Thesis objectives

Two experimental studies with two different DIC systems will be described. The experimental program about short coupling beams was initiated by Professor Boyan Mihaylov. The tests were performed in the University of Patras. A second experimental program about shear walls at the University of Liège is conducted by PhD student Renaud Franssen. In the framework of this thesis, these two studies, more precisely the first test of each experimental campaign, is used to address the following objectives:

- Discuss best practices for performing DIC measurements.
- Analyze DIC data from the two tests.
- Study the deformation patterns and validate the kinematic models of the 2PKT and 3PKT.
- Use measured kinematics along failure planes together with local constitutive models to evaluate the mechanisms of shear resistance.

1.6 Thesis outline

The master thesis is structured into different chapters.

In chapter 2, the test on the shear wall and on the coupling beam are described in terms of test specimen properties and DIC setup.

In chapter 3, the shear behavior of short walls and short coupling beams is described. The kinematic model for both members, 3PKT and 2PKT, are presented. Local constitutive models to evaluate the load-bearing mechanisms based on DIC measurements are explained.

Chapter 4 focuses on the test of the shear wall. The global behavior is described in terms of load-displacement response and at failure. Furthermore, the data from DIC analysis will be compared with other measurements in order to validate the DIC. The kinematics of the wall at failure from DIC is compared to the 3PKT deformation pattern. Finally, the shear-resisting mechanisms, namely aggregate interlock, critical loading zone and stirrups, are computed.

Chapter 5 is related to the test of the coupling beam. The same points as in chapter 4 are discussed in this section.

Chapter 2

Experimental campaigns & DIC systems

2.1 Test on shear wall

2.1.1 Test specimen

Geometry and reinforcement

The wall has a rectangular cross-section with a depth of 1500 mm and a width of 230 mm. The wall is 2300 mm high. Two reinforced concrete blocks are rigidly connected to the wall at its top and bottom. The vertical and horizontal force are applied on the top block.

The wall is reinforced by a series of longitudinal reinforcing bars as shown in Fig. 2.1. A small amount of transverse reinforcement has been placed : 4 stirrups of $\phi 8$ every 600 mm. A global view of the reinforcement is represented in Fig. 2.2.

Material properties

Concrete The first specimen of the series of experiments was cast with ordinary concrete. Tests on cylindrical concrete samples presented a strength of about 53

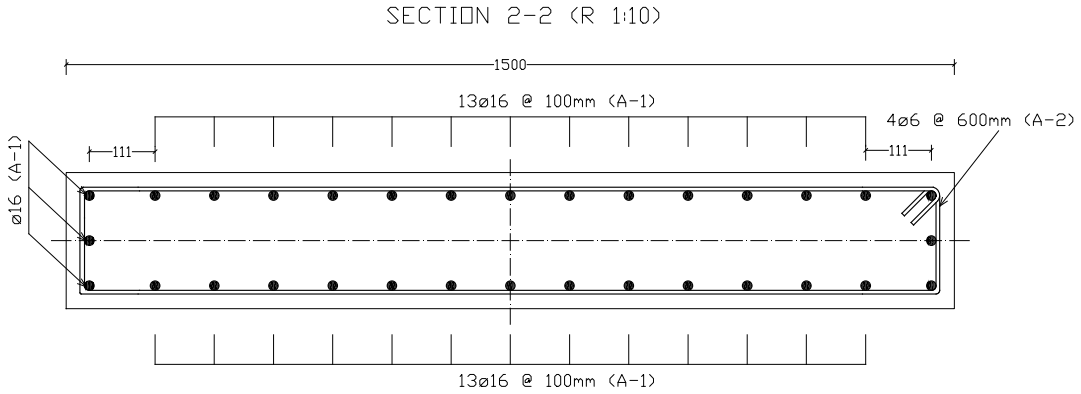

Figure 2.1: Longitudinal reinforcement.

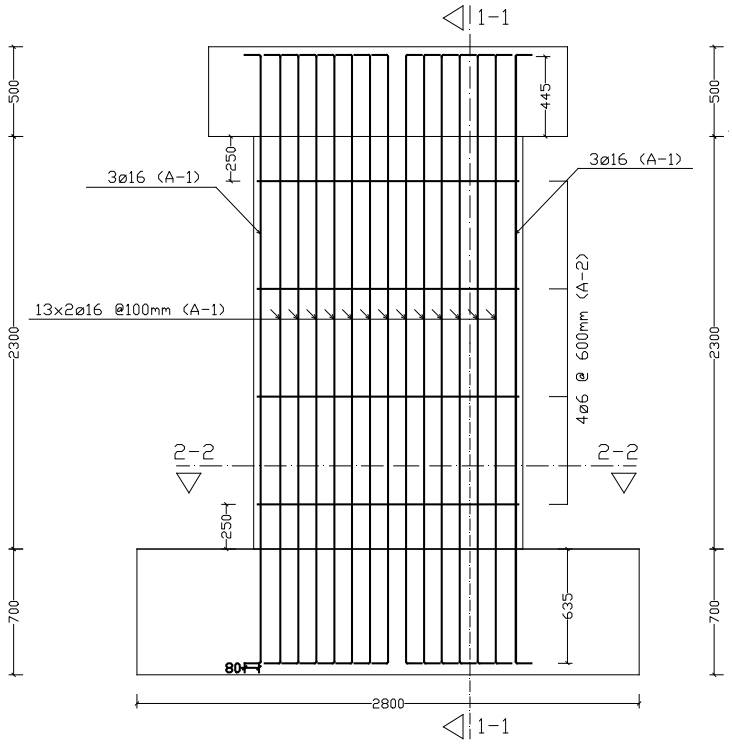

Figure 2.2: Transverse reinforcement. The stirrups in the test had a diameter of 8 mm.

MPa. Young's modulus was estimated at 32000 MPa. The maximum aggregate size is 16 mm.

Steel Tests on stirrups revealed a yield strength of $f_y = 540\ MPa$ and an ultimate tensile strength of $f_u = 640\ MPa$. The strain at peak stress is $\varepsilon_u = 6.5\%$. The longitudinal reinforcement has a yield strength of $f_y = 530\ MPa$ and an ultimate strength of $f_u = 620\ MPa$. The strain at peak stress is $\varepsilon_u = 8\%$.

All geometrical and material properties of the test specimen are summarized in Tab. 2.1.

Loading and boundary conditions

The specimen is fixed at the bottom and can freely move at the top. The foundation is anchored in the slab of the laboratory. The axial force is applied by 6 steel bars, 3 on either side, that are connected to a steel member on top of the wall. By pulling on these steel bars from below the floor, they compress the wall through the steel member. The horizontal load is applied by a jack, as can be seen in Fig. 2.3.

Instrumentation

One face of the wall is prepared with a speckle pattern, while the opposite face and the sides are equipped with displacement transducers (potentiometers) and LED sensors. The instrumentation is depicted in Fig. 2.4 and 2.5. Blue instrumentation elements are mostly displacement transducers (DT), whereas the circles distributed

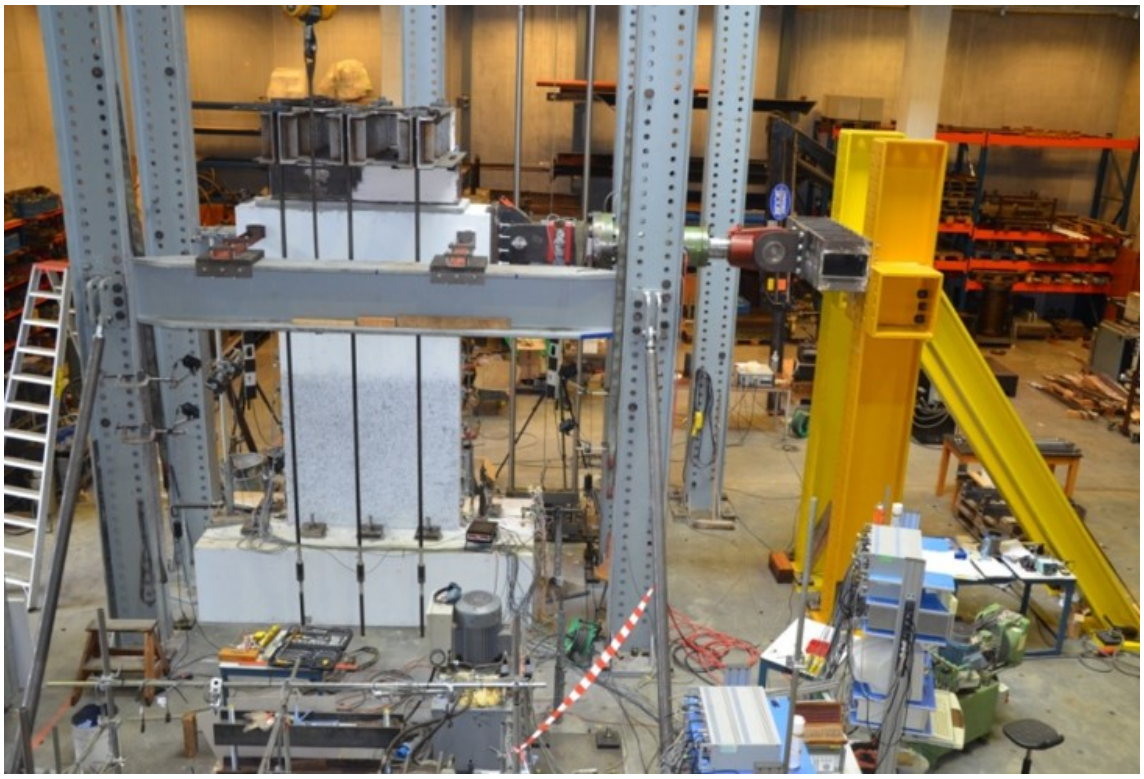

Figure 2.3: Test setup.

b $[mm]$	h $[mm]$	d $[mm]$	a $[mm]$	a/h $[-]$	ρ_l $[\%]$	$\rho_{l,web}$ $[\%]$	f_y $[MPa]$	ρ_v $[\%]$	f_{yv} $[MPa]$	f'_c $[MPa]$
230	1500	1088	2550	1.7	1.86	1.86	530	0.04	540	53

b = width of wall cross-section; h = depth of wall section ; d = effective depth of section;
a = M/V - wall height subjected to shear; a/h = aspect ratio;
$\rho_l = 2A_s/bh$ = ratio of longitudinal reinforcement; $\rho_{l,web}$ = ratio of longitudinal web reinforcement;
f_y = yield strength of longitudinal reinforcement; ρ_v = ratio of transverse reinforcement;
f_{yv} = yield strength of transverse reinforcement; f'_c = concrete cylinder strength

Table 2.1: Properties of the shear wall.

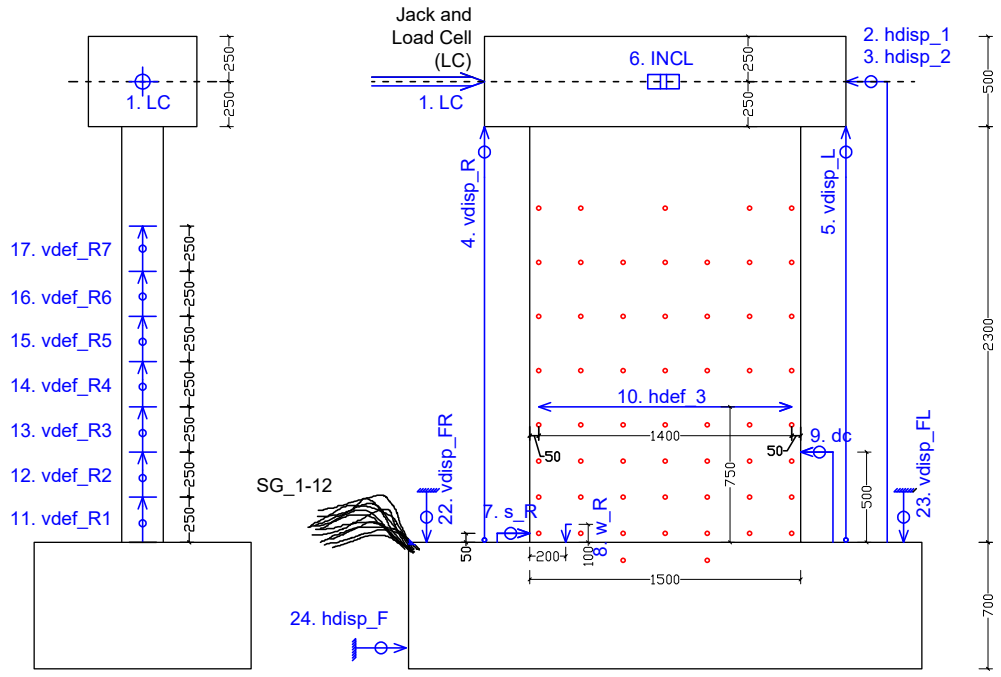

Figure 2.4: Instrumentation (DT sensors, LED targets) of the wall, with tension side view.

on the wall's face are LED targets.

Displacement transducers, or potentiometers, measure the relative displacement between two points by converting the motion into an electrical signal. A part of the DTs measure global displacements like the horizontal and vertical displacement of the top block with respect to the foundation as well as a possible movement of the foundation. In addition, several other displacements are measured, like a possible crack opening at the base (DT n°8), a possible slip at the base (DT n°7) and the horizontal displacement of the compression side (DT n°9). Their positions are specified in a way such that their measurement is useful for the kinematic model presented in Chapter 3.

The LED system consisting of 54 targets permits to track the displacement of each LED during the experiment and to give an overall information about the displacement field and deformations.

2.1.2 DIC system

The system used for the tests on shear walls is *Davis 8.0.3 (Lavision)*, using 2 cameras partly mapped. One camera focuses on the bottom part of the wall whereas the second camera keeps track of the top part. A part in the middle of the wall is captured by both cameras. As a consequence, the definition of the experimental setup in the calibration settings is not necessarily straightforward. The experimental setup is shown in Fig. 2.6. In addition to the 2 cameras and the box that receives all signals and transmits them to the computer, 2 vertical light sources provide more illumination. They flash every time a picture is recorded.

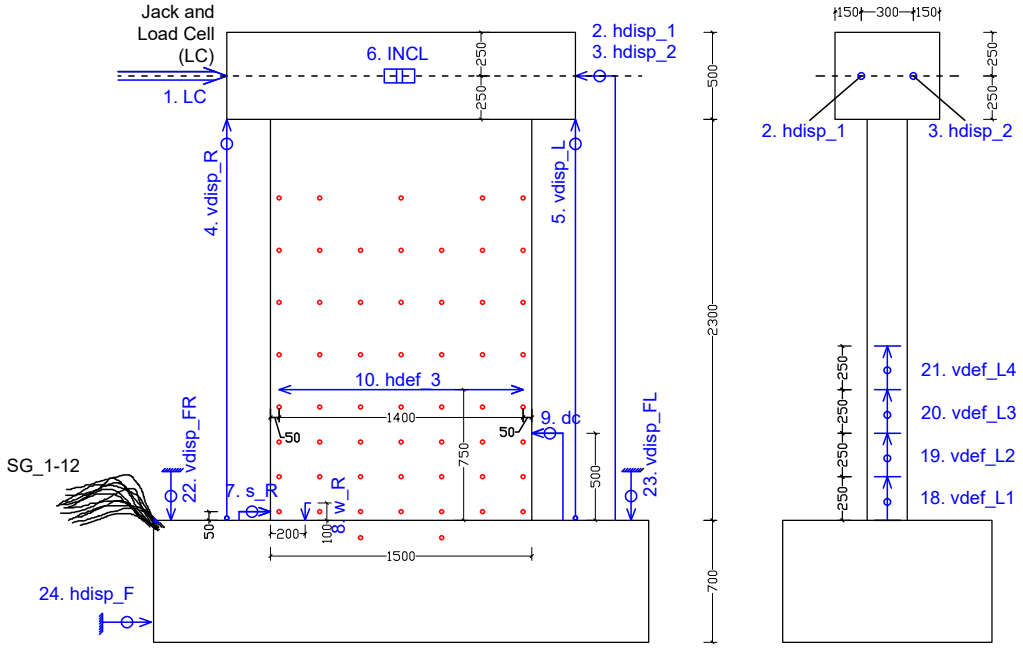

Figure 2.5: Instrumentation (DT sensors, LED targets) of the wall, with compression side view.

Figure 2.6: Experimental setup of DIC.

Calibration

The calibration process is crucial for the processing of the data and the reliability of the results.
A correct calibration should lead to results representing the true dimensions, which is defined by an image scale pixel/mm. The calibration should also correct inherent camera lens distorsions and account for oblique viewing setups. The latter was not negligible in the setup of the tests of the short walls in the University of Liège, since both cameras were fixed on a same rail (see Fig. 2.6) but capturing two different frames at different heights which leads to oblique viewing setups.
From the same point of view, a simple "define scale" operation was not possible since this option would not take into account neither camera lens distortions nor perspective distortions but only determine a pixel/mm scaling (Lavision, 2015). The more complex alternative to the simple "define scale" operation is a perspective calibration correction with use of a calibration plate. A calibration plate, visible in Fig. 2.7, is characterized by a number of parameters, like shape, size and distance between marks, distance between planes.

It can be noted here that the calibration process can take place before a test starts. It consists of taking several pictures with a calibration board, called "views", selecting 3 reference points on the board visible in each picture and do the calibration process according to the software manual. Lavision (2015) recommends 3 views for higher accuracy, while 1 view suffice in general.
An example of a recorded picture during the calibration process can be seen in Fig. 2.7. During the calibration process, the 3 reference points must be selected (circles with cross). The first reference point defined in the first view will define the origin of the calibrated coordinate system.
In software Davis, the calibration can be changed afterwards by selecting other calibration settings but using the same pictures recorded during the first calibration. One can even choose other recordings of the same test.

Before any recording of views, the setup must be defined. The present case of 2 cameras sharing a common area at the middle of the wall is quite special. One has to think about the setting to chose from the different options in step 1 (Fig. 2.8). The setup was neither 2 independent cameras nor 2 stereo cameras (mapped) but rather a mix of both. Both camera frames share a common area, the middle part of the wall so that the coordinate system of both frames should share a common origin, so that they are not independent. Two options could be considered:

- The first option consists of carrying out a calibration for either camera, choosing the option *2 cameras (independent 2D+2D)* with 2 separate coordinate systems. The origin of both coordinate system are situated at different locations. After calibration, one must redefine the origin (option *define origin, maintain calibration*) without changing any calibration parameters. The origin should be selected at a location in the overlapping area so that the same point can be selected for camera 1 and 2.

- The second option will use the *advanced settings* allowing the definition of 2 different coordinate systems. However, during the calibration process, one can

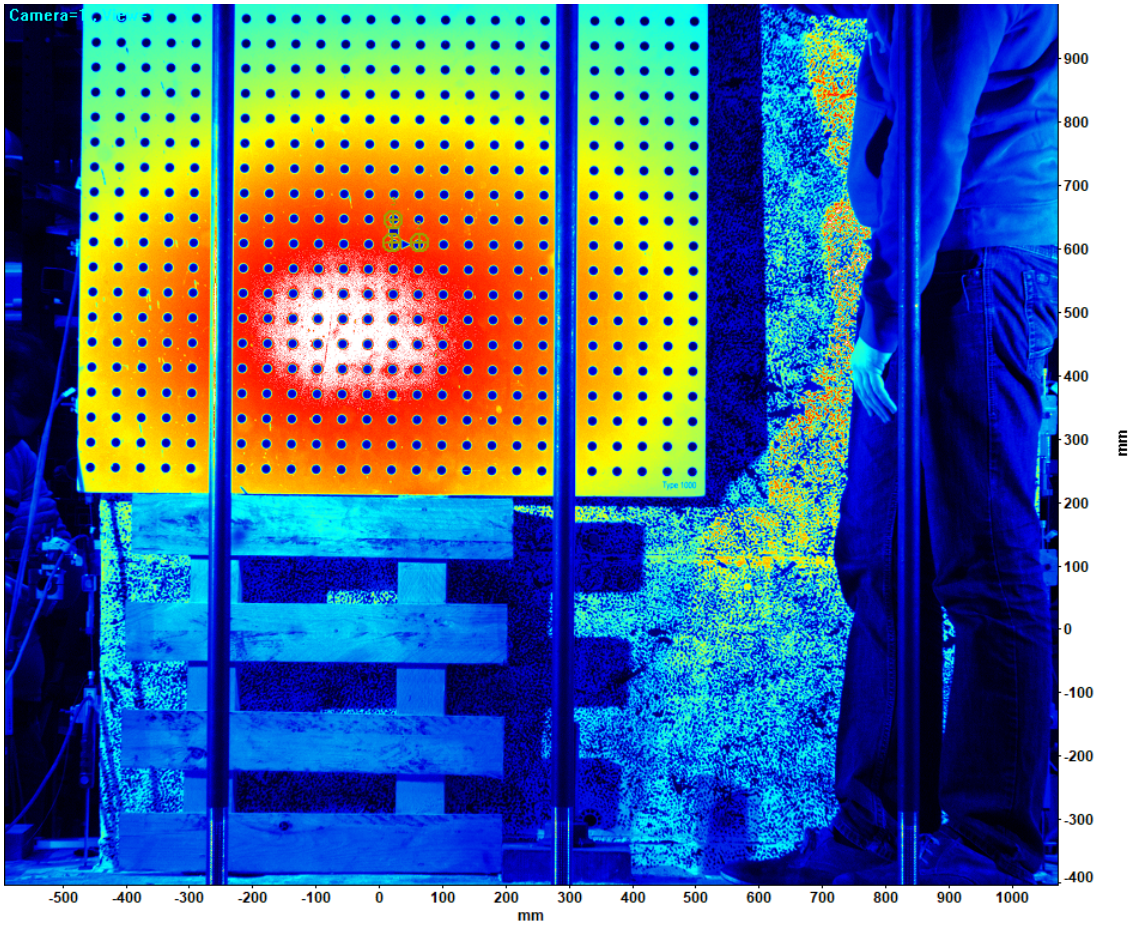

Figure 2.7: Recorded picture during the calibration process.

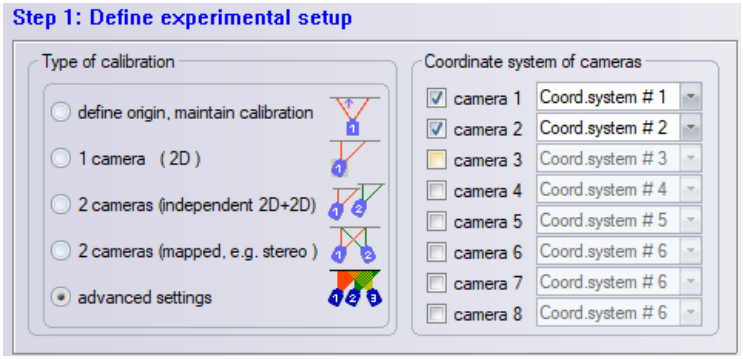

Figure 2.8: Step 1 of calibration process : Define experimental setup.

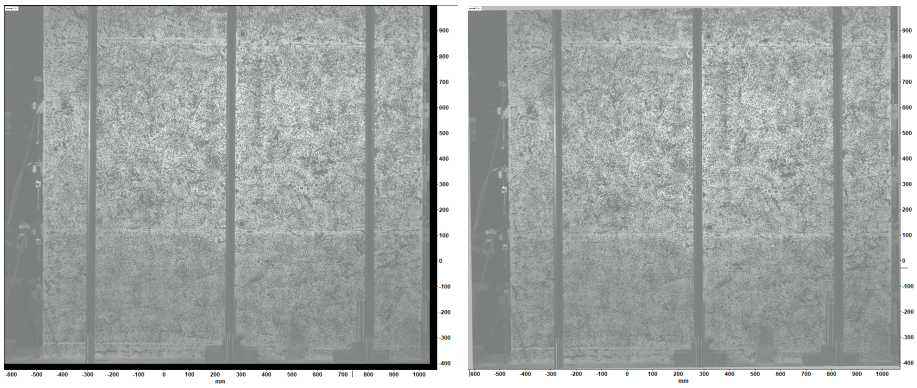

(a) Raw image, without correction. (b) Corrected image.

Figure 2.9: Comparison between raw and corrected image.

select the same origin by using a recorded photograph where the calibration plate is visible in both frames (Lavision, 2015).

It is important to know that the output of the calibration is mainly a scaling of the picture taking into account any varying magnification over the image such as is the case when using a perspective viewing direction, but also distortions introduced by the lens. The scale factor (in pixel/mm) represents the number of pixels that one millimeter contains. A more convenient way to express the scale factor is in mm/px, which defines the size of a pixel in the corrected image.

The calibration can be verified in several ways. One way is to compare the width of the wall in the corrected image with the real dimension. Unfortunately, no measurements were done on the uncracked wall such that a comparison was not possible. However, in order to illustrate the effect of the calibration, one can compare the depth of the wall measured on the corrected image with the measurement on the raw image. As an example, the length of a line close to the top of the shear wall was about 1513 mm in the corrected image, whereas in the original picture, with the same pixel/mm scaling, the distance was only of about 1478,5 mm. The correction has thus a significant effect[1].
Another way to verify the calibration is to take pictures for a rigid body motion, e.g. uniform displacement, and check if the displacement is correct in the calibrated images.

The processing of the recorded pictures gives a displacement field. Each frame will be processed separately, on the basis of its proper calibration and pictures. Both datasets will then be combined[2] and the vector fields will be merged[3] so that one get the displacement field of the whole specimen.

[1]The expected depth should have been 1500 mm. If we consider a general construction precision of 1 cm, the most critical error would be if we consider smallest possible depth of wall of 1490 mm. The calibrated image give a dimension of approximately 1513 mm. The maximum possible error is thus (1513-1490)/1500 = 1,53 %.

[2]The operation "copy and reorganize datasets - merge datasets to multi frame" will combine both datasets.

[3]The operation "merge vectors" will interpolate the displacement field of the top frame in order to match it with the bottom one.

Processing

The test consisted of 9 load steps separated by load stops. The acquisition rate of the DIC setup was relatively high, a picture every half a second (frequency of 2 Hz). The recording was interrupted after each loading interval. To analyze a given load step, the corresponding images should be appended to the reference cycle, which consists of 60 photographs of the specimen without any loading. The displacement field issued by the processing is then calculated with respect to the first processed image, which is a picture showing the unloaded specimen.
For example, in case of the last load step where failure occurred, after appending the corresponding dataset to the reference cycle, the total set of photographs comprise 924 pictures. The following steps are necessary to process such a dataset:

- Select the operation "2D DIC (single camera time series)" from the group "Digital Image Correlation (LSM) - time-series".
- Define the mask by drawing polygons marking the area of the specimen with speckle pattern.
- Select seeding points.
- Define time-series settings: correlation mode and maximal expected displacement (in pixels).
- Define displacement calculation settings: Subset size, step size, calculation mode, activate or not the outlier filter[4] and smoothing filter.

Strain uncertainty

This section is dedicated to practical strain uncertainty evaluation. It should be noted that strain calculations are noisier for small subset sizes, and therefore for small step sizes since the step size is chosen to be proportional ($\sim 1/4$ of subset size). The strain calculation for a subset of 15 pixels is a lot noisier than the strain field for a subset of 51 pixels. This difference can be seen in Fig. 2.10 that depicts maximum principal strains of the specimen in still position, where zero strains would be expected. The maximum principal strains for this configuration give an idea of the strain uncertainty.
While for the larger subset size of 51 pixels (Fig. 2.10a), the strain uncertainty has an order of magnitude of 0.01% with a relative smooth appearance, the strain uncertainty for a smaller subset size (e.g. 15 pixels, Fig. 2.10b) is higher, of an order of magnitude around 0.1%. In Lavision (2015), similar uncertainties were computed for those subset sizes.

[4]If enabled, vectors that deviate too much from their neighboring vectors will be removed from the deformation field (Lavision, 2015).

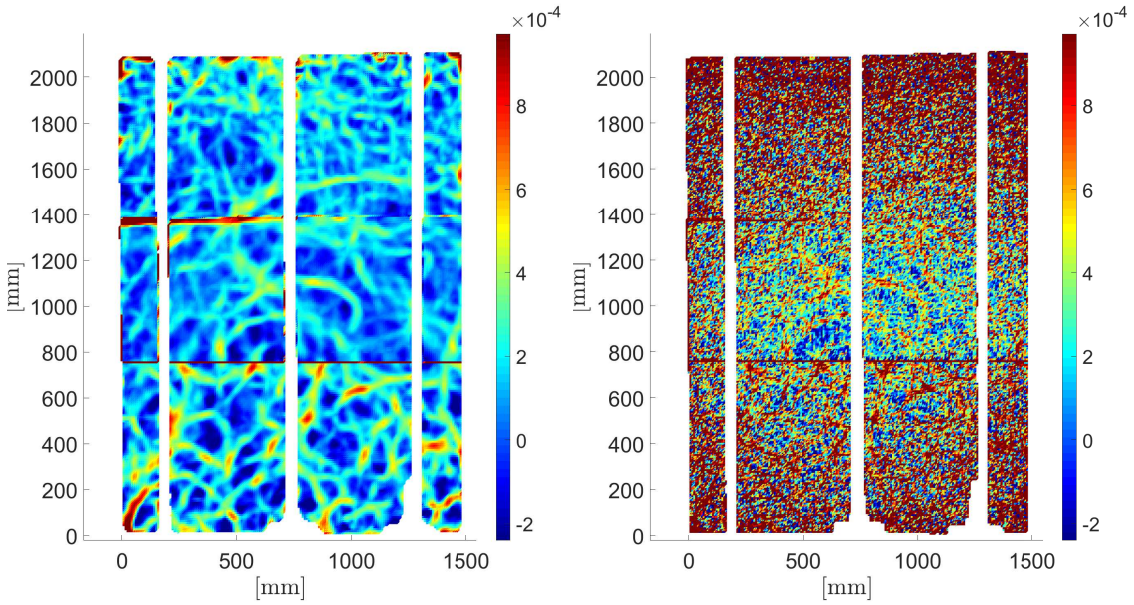

(a) Subset size : 51 pixels.

(b) Subset size : 15 pixels.

Figure 2.10: Strain uncertainties for different subset sizes (colorscale ranging from -0.00024 to 0.00097).

2.2 Test on short coupling beam

2.2.1 Test specimen

Geometry and reinforcement

The geometry of the specimen is shown in Fig. 2.11. It is a short coupling beam, orientated vertically, of a length of 1000 mm, a depth of 800 mm and a width of 140 mm. Two rigid blocks are connected to the beam. The blocks and the beam were not poured at the same time. As a consequence, their material properties are not identical and the connection is not necessarily completely rigid.

The reinforcement of the beam is represented in Fig. 2.12. Four longitudinal reinforcing bars of diameter of 20 mm are located at each side of the beam. A light transverse reinforcement is provided, consisting of stirrups of 8 mm in diameter spaced by 180 mm. The outer ones are only situated 50 mm from the edge. The transverse reinforcement ratio is equal to $\rho_w = 0.399\%$.

Material properties

Concrete The commanded concrete is class C25/30 with an maximum aggregate size of 16 mm.
The material was separately tested for the base block, the top block and the coupling beam on cylindrical specimens (height = 300 mm, diameter = 150 mm). The results are summarized below:

- The base block presented a mean compression resistance of $f_{cm} = 40.7\ MPa$ after 129 days.

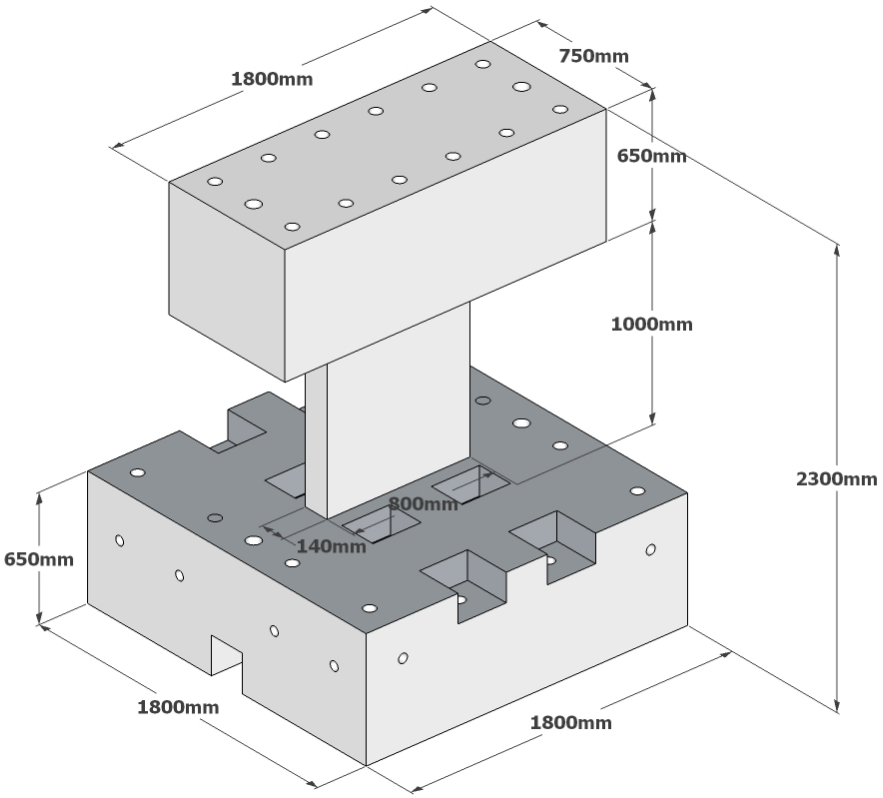

Figure 2.11: Geometry of test specimen.

- The coupling beam had a mean compressive strength of $f_{cm} = 36.4\ MPa$ after 123 days.

- The top block had a mean compressive strength of $f_{cm} = 38.1\ MPa$ after 108 days.

Steel The commanded reinforcement is class S500C. Respectively 3 specimens were tested for the reinforcing bars of diameter 20 mm and the stirrups of diameter 8 mm. For the stirrups, the yield stress is approximately 505 MPa and for the longitudinal reinforcement around 512 MPa.

Geometrical and material properties are summarized in Tab. 2.2.

b	h	d	a	a/d	ρ_l	f_y	ρ_v	f_{yv}	f'_c
$[mm]$	$[mm]$	$[mm]$	$[mm]$	$[-]$	$[\%]$	$[MPa]$	$[\%]$	$[MPa]$	$[MPa]$
140	800	737	1000	1.36	1.22	512	0.40	505	36.4

b = cross-section width; h = total depth of section; d = effective depth of section;
a = shear span; a/d = shear-span-to-effective-depth ratio;
ρ_l = ratio of bottom longitudinal reinforcement;
f_y = yield strength of longitudinal reinforcement; ρ_v = ratio of transverse reinforcement;
f_{yv} = yield strength of stirrups; f'_c = concrete cylinder strength

Table 2.2: Properties of the short coupling beam.

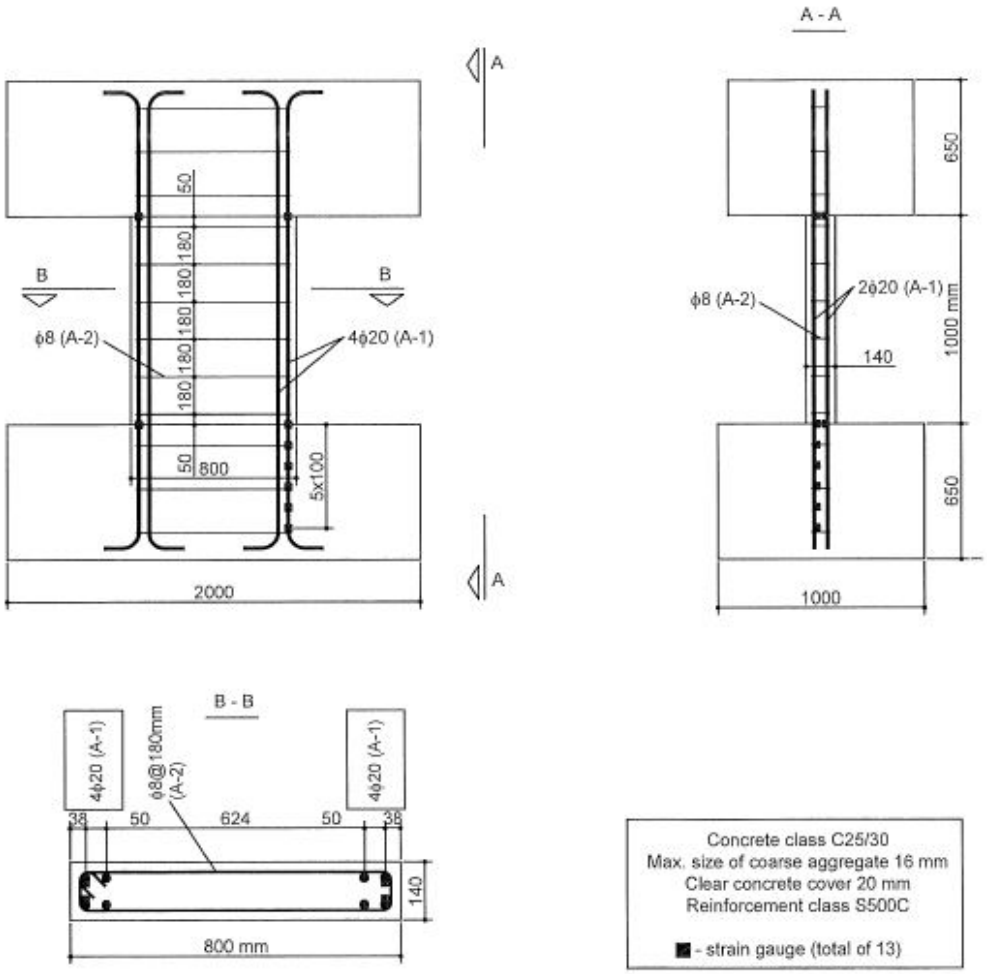

Figure 2.12: Reinforcement of specimen.

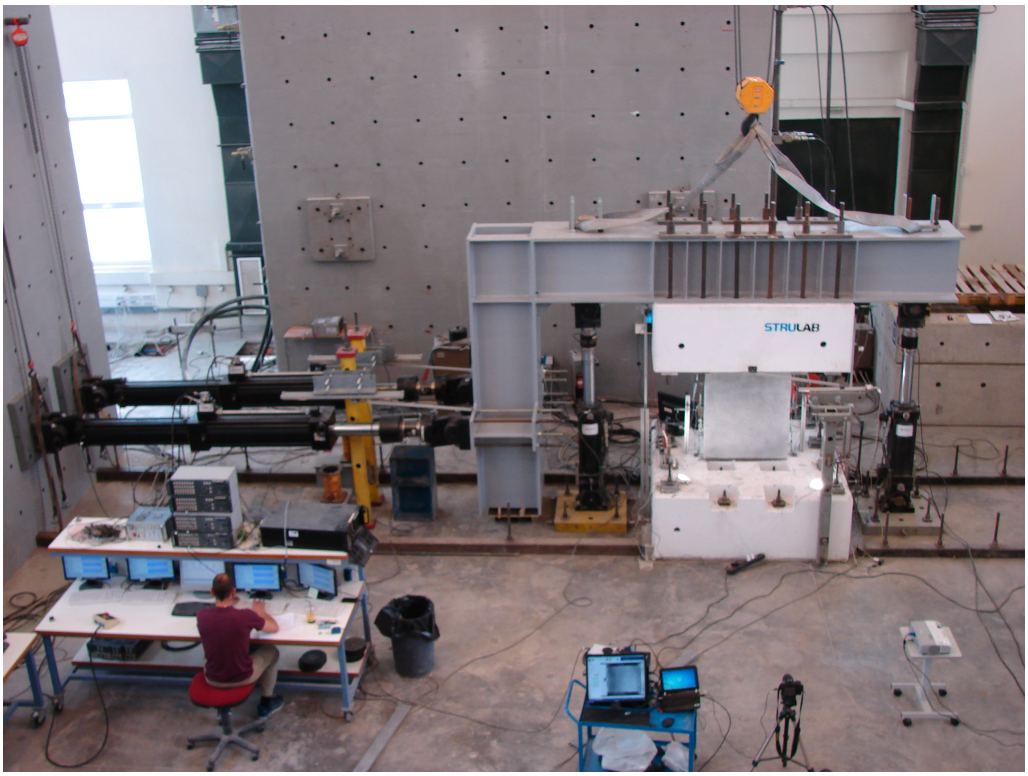

Figure 2.13: Global view of the test setup.

Loading and boundary conditions

Fig. 2.13 shows the global setup of the test. The coupling beam is connected to the rigid blocks, which represent the stiff adjacent walls of a typical short coupling beam. A massive steel member in L-shape is rigidly connected to the top block. The steel member is maneuvered by 4 actuators. Two of them load the steel member horizontally by pulling on it towards a wall. The action from those two horizontal actuators is the driving force of the test. They are loading the vertical part of the steel beam on both sides, distant by 1 meter. They are exactly aligned with the mid-section of the coupling beam. The other two vertical actuators are rather adjusting the orientation of the steel member before and during the test. More precisely, before loading the beam horizontally, the two vertical actuators adjust the steel beam in order to position it horizontally because the instrumentation and the steel member itself induced some movement, especially rotation, of the coupling beam and top block. They are separated by 3 meters. Even though the steel member is relatively massive, the connection of the horizontal and vertical part is not totally rigid.

Instrumentation

Fig. 2.14 depicts the planned instrumentation of sensors. A schematic of the implemented instrumentation is shown in Fig. 2.15 and a photo of the real instrumentation is shown in Fig. 2.17. The two vertical measurement devices between the top and bottom block as well as potentiometers measuring the horizontal displacement of the top block with respect to the bottom block are missing in Fig.2.15 but are visible in Fig. 2.16.

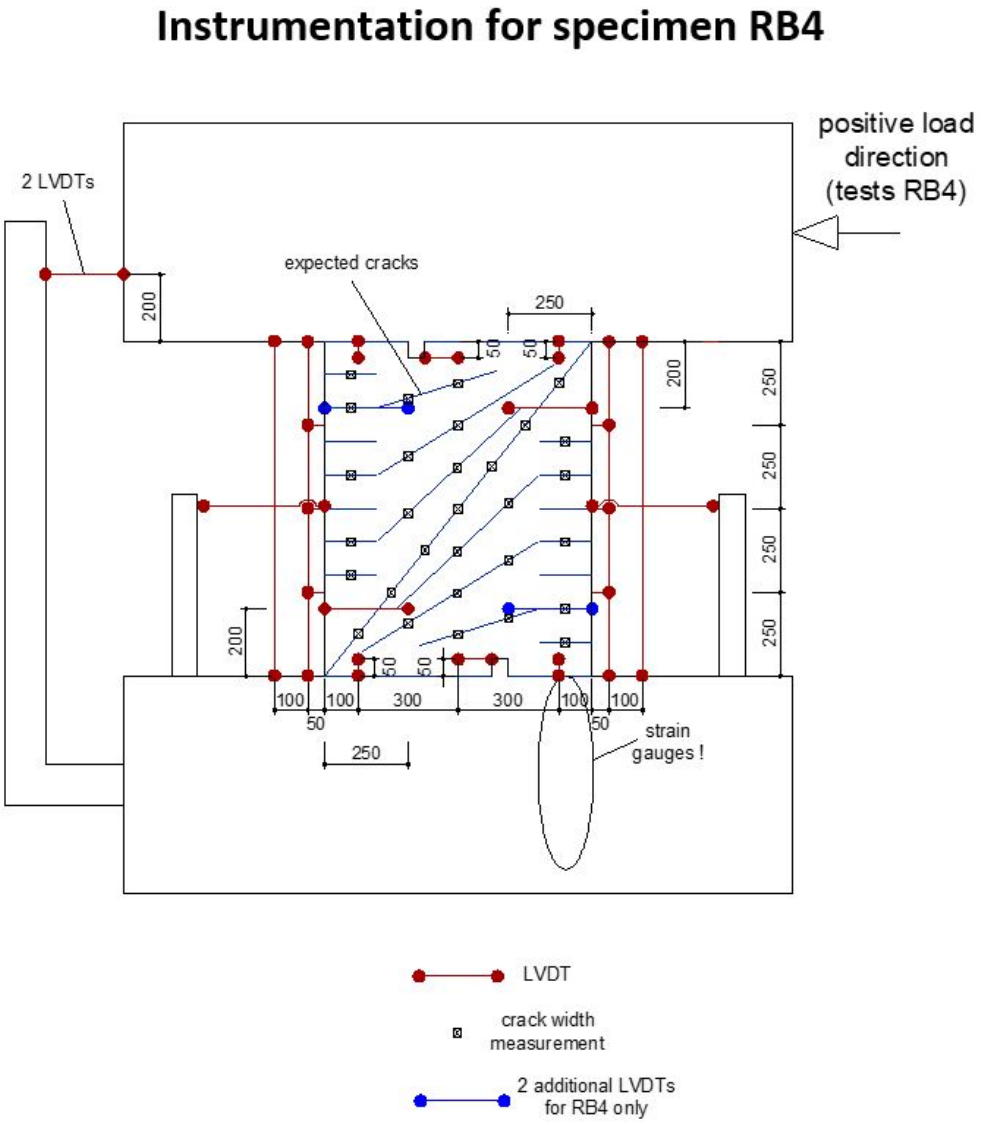

Figure 2.14: Planned instrumentation of the coupling beam.

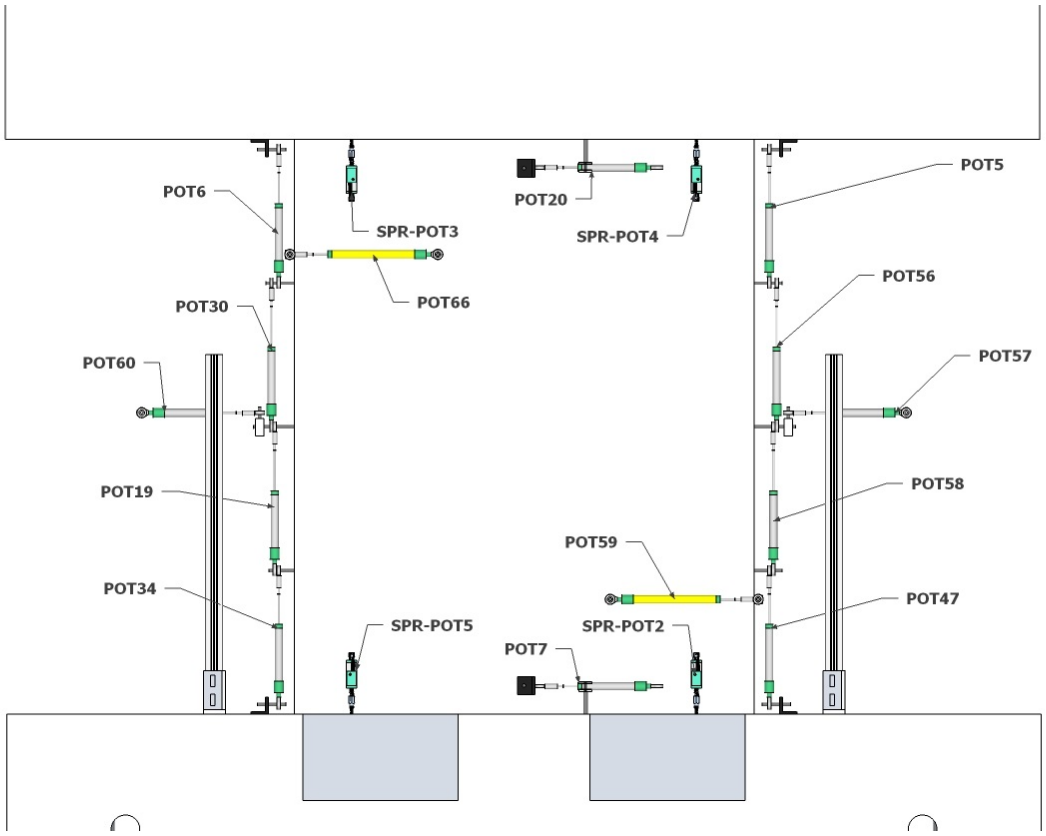

Figure 2.15: Implemented instrumentation of the coupling beam.

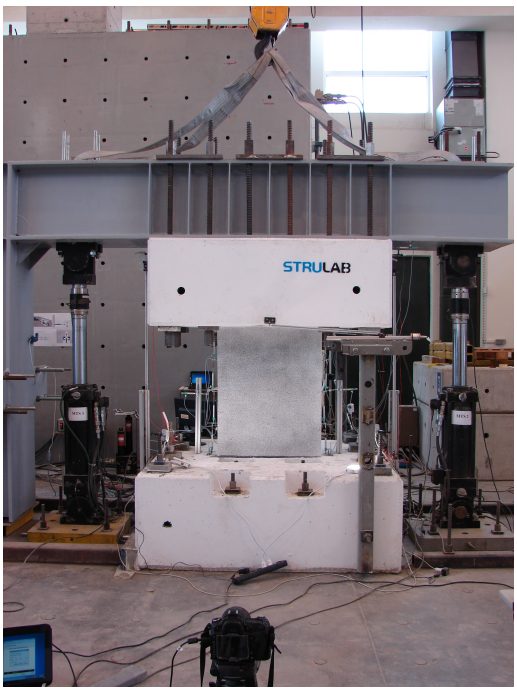

(a) Speckle pattern and DIC system.

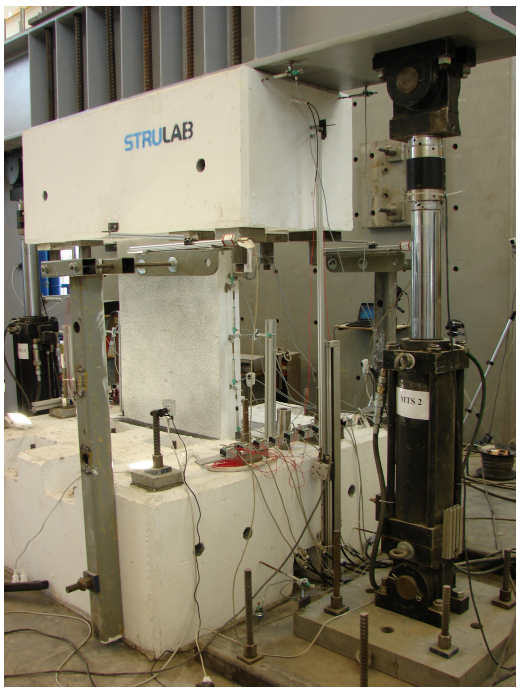

(b) Instrumentation on the front and sides.

Figure 2.16: Photographs from the experimental setup (front view).

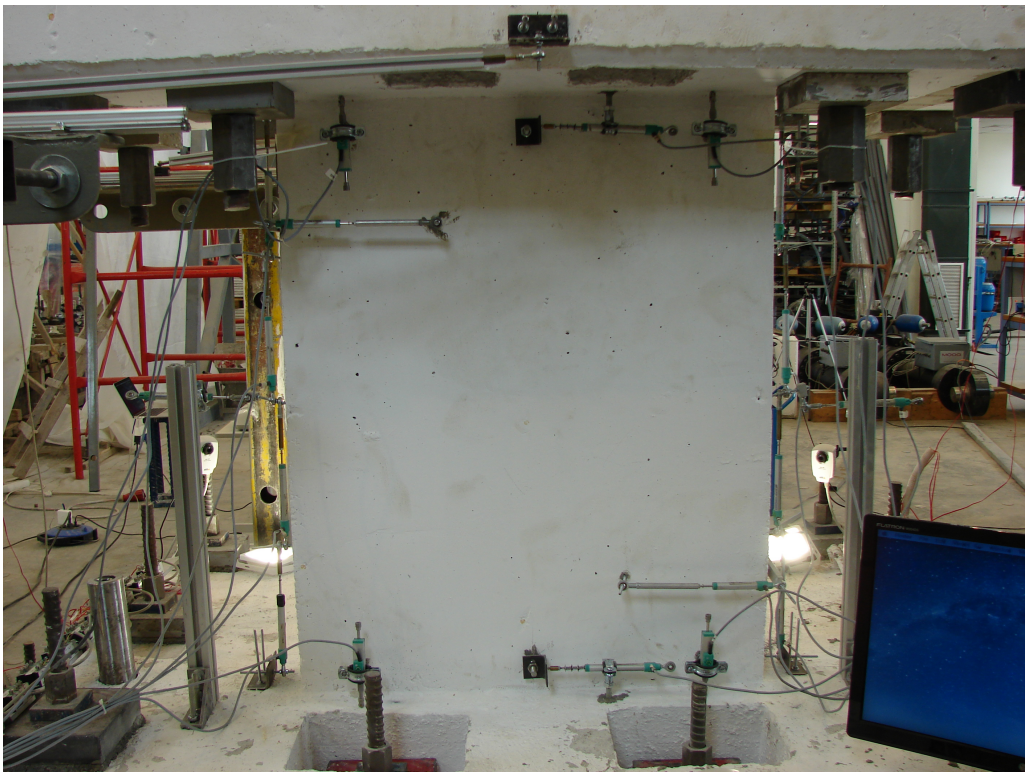

Figure 2.17: Instrumentation on the back face (without speckles) of the specimen.

2.2.2 DIC system

The system used for the tests on the coupling beams in Patras is different. Only one camera records the deformation of the specimen under loading. The specimen is considerably smaller than the shear wall such that the frame is sufficient to capture the whole specimen. The calibration is done with a standard board. The software used for these experiments is *Ncorr*. Since the whole DIC setup including the calibration and the processing of the data was in charge of the laboratory in Patras, only limited information will be provided in this chapter. The main processing parameters are

- type = regular (analysis)
- radius = 30
- spacing = 3
- pixtounits = 0.5157

The subset spacing can be referred to as the step size by considering $step\ size = subset\ spacing + 1 = 4$. The subset radius is referring to a circular subset and not a rectangular one as it is used in *Davis*. The subset radius is 30 which corresponds to, by multiplying by the pixel size of 0.5157 mm/px, 15.47 mm radius.

Pictures were taken every 5 seconds.

Chapter 3

Shear behavior of short coupling beams and walls

3.1 Deformation patterns

In this chapter, kinematic models will be presented. They are capable of describing the deformed shape of a specific element. The kinematic model for short coupling beams uses 2 degrees of freedom (DOF) to describe the deformation pattern, while the model for shear walls uses 3 degrees of freedom. In combination with equilibrium equations and stress-strain relationships, those models are capable of predicting the shear strength and deformation at failure. The components of shear strength are also distinguished and explicitly calculated (B. I. Mihaylov, Bentz, & Collins, 2013).

These models will be used to describe the deformation of the wall and the coupling beam tested in the lab. The DOFs are computed from experimental measurements, mainly displacement transducers. The predicted deformation will then be compared to the actual deformation from DIC. In this way, the prediction can be validated.

3.1.1 2PK model for short coupling beams

Short coupling beams are short members (aspect ratios a/h smaller than 2.5) present in coupled wall structures. They carry high shear stresses and work in double curvature.

Fig. 3.1 gives an overall description of the 2PKT for short coupling beams. The adjacent walls are represented as rigid blocks. The deformation of the beam is described by 2 kinematic parameters (degrees of freedom). The first degree of freedom is the average strain $\varepsilon_{t,avg}$ in the top and bottom longitudinal reinforcement. The second degree of freedom is the transverse displacement Δ_c. The complete deformation is described by the sum of the deformation pattern associated with each of those two DOF as can be seen in Fig. 3.2. The transverse displacement originates from the deformations of concrete in the critical loading zone (CLZ). The critical loading zone can be defined as the zone where concrete crushing occurs. The model is not completely symmetrical due to the formation of the CLZ only at one end of the diagonal crack. According to experimental observations, this compression zone is deeper at one end (B. Mihaylov, Liu, & Lobet, 2018), however, compression

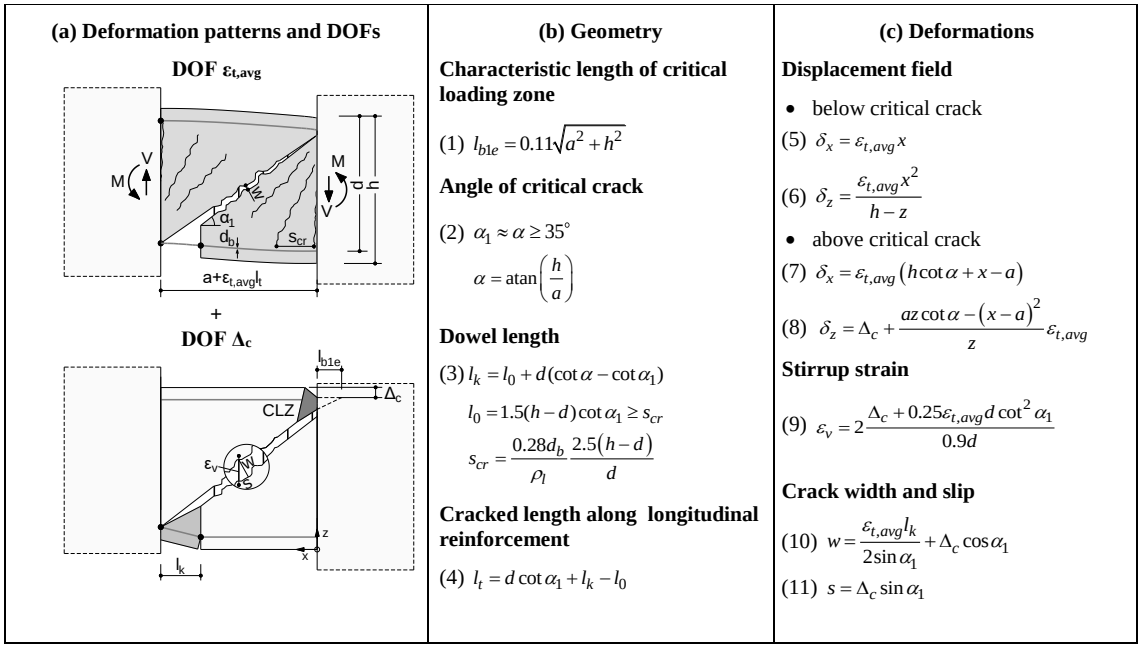

Figure 3.1: Two-parameter kinematic model for short coupling beams (B. Mihaylov, Liu, & Lobet, 2018).

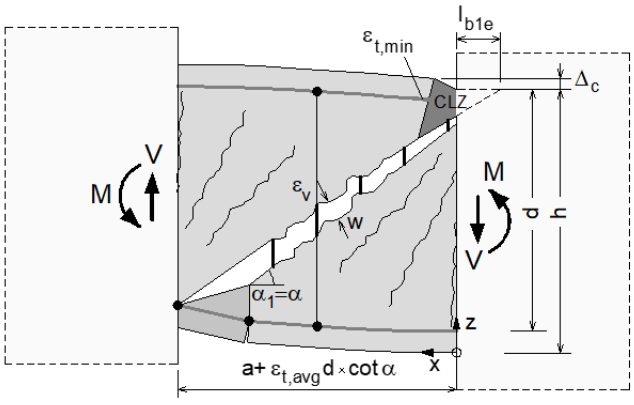

Figure 3.2: 2PK model for coupling beams.

zones are generally found at both ends of the beam.

The deformation pattern associated with the DOF $\varepsilon_{t,avg}$ can be described as follows. When loaded by shear forces, the longitudinal reinforcement elongates. The diagonal crack that formed due to high principal tensile stresses widens. Radial flexural-shear cracks also form. Those cracks delimit a fan of rigid struts on both sides of the diagonal crack. Similarly to the diagonal crack, the cracks of the fan also widen due to the elongation of the longitudinal reinforcement.

The deformation pattern associated with the second DOF Δ_c can be qualified as a more typical shear deformation. Here, the deformations are related to the critical diagonal crack and its ends. While the top end is represented by the CLZ, of a length of l_{b1e}, and its important diagonal compressive stresses, the bottom end is the location where the longitudinal reinforcement is subjected to double curvature, over a length of l_k.

Expressions for the length of the CLZ, the dowel length, the cracked length along longitudinal reinforcement and the angle of the critical crack can be found in Fig. 3.1 (Eq. (1)-(4)). The complete displacement field can then be computed thanks to Eq. (5)-(8), in function of the 2 DOFs.

Eq. (9)-(11) provide expressions to determine the stirrup strain and the crack kinematics, more precisely the crack width and slip, halfway along the crack. Those 3 values are then used to compute the different shear resistance mechanisms across the diagonal crack in function of the 2 DOFs.

Using the equilibrium of the forces on the beam, the values of $\varepsilon_{t,avg}$ and Δ_c can be evaluated and thus, the complete behavior of the beam is predicted.

3.1.2 3PK model for walls

The three-parameter kinematic theory for shear-dominated reinforced concrete walls was published by B. I. Mihaylov, Hannewald, and Beyer (2016). Similarly to the model for short coupling beams, the kinematic model is able to describe the deformation pattern in walls whose aspect ratios is smaller than 3. Based on the kinematic model, the response of these walls is predicted.

The three degrees of freedom (DOF) and their associated deformation are depicted in Fig. 3.3.

The first DOF $\varepsilon_{t,avg}$ is the average tensile strain in the flexural reinforcement below the critical crack. The critical shear crack is modeled as a straight line inclined by an angle of α_1 with respect to the vertical axis. The deformation due to $\varepsilon_{t,avg}$ consists in a rotation of the top rigid block and a cracking pattern below the critical crack. The cracking pattern defines a series of rigid radial struts in form of a fan pinned at point A and delimited by the flexural tensile reinforcement. The struts are assumed to rotate about point A. The rotation is proportional to the elongation of the tensile reinforcement between the foundation and the strut. The

kinematics related to $\varepsilon_{t,avg}$ reflect mainly flexural deformations.

The second DOF Δ_c is the horizontal displacement in the critical loading zone (CLZ). Since the other two DOF are set to zero, the bottom part remains undeformed while the top rigid block translates laterally. This lateral displacement causes a double curvature of the tensile reinforcement over a length l_k. This deformation pattern can be associated with shear deformations.

The third DOF Δ_{cx} corresponds to a vertical displacement of the top block in the CLZ as a result of a rotation of the rigid block about point B. The action of the vertical load drives the block downwards. The bottom fan is not affected by Δ_{cx}, however, the rotation induces a double curvature of the flexural reinforcement.

The superimposition of those 3 deformations gives the total deformation pattern depicted in Fig. 3.3(d).

The displacement of each point in a x-z grid (δ_x and δ_z) can be computed thanks to small displacement kinematics in function of the 3 DOFs. The displacements of the points of the rigid block are given by

$$\delta_x(x,z) = \frac{\varepsilon_{t,avg}\, l_t}{d}(h-z) + \frac{\Delta_{cx}}{d}(h-d-z) \tag{3.1}$$

$$\delta_z(x,z) = \left(\frac{\varepsilon_{t,avg}\, l_t}{d} + \frac{\Delta_{cx}}{d}\right) x + \Delta_c. \tag{3.2}$$

The displacements of the points below the critical crack are given by

$$\delta_x(x,z) = \varepsilon_{t,avg}\, x \tag{3.3}$$

$$\delta_z(x,z) = \frac{\varepsilon_{t,avg}\, x^2}{h-z}. \tag{3.4}$$

The model can also be used to estimate the crack width and slip half-way along the critical shear crack. The crack opening is calculated by

$$w = \left[\frac{\varepsilon_{t,min}\, l_k}{2\,\sin\alpha_1}\frac{h}{d} + \Delta_c\,\cos\alpha_1 + \frac{\Delta_{cx}}{d}\left(\frac{h}{2\,\sin\alpha_1} - d\,\sin\alpha_1\right)\right]\frac{1}{n_{cr}} \tag{3.5}$$

where $\varepsilon_{t,min}$ is the strain in the flexural reinforcement within l_k. The expression in the brackets considers one single dominant diagonal crack. However, in members with considerable reinforcement in the web, the crack opening is distributed among a number (n_{cr}) of cracks.

The slip between the crack faces can be estimated by

$$\Delta_{ci} = \Delta_c\,\sin\alpha_1 + \Delta_{cx}\,\cos\alpha_1 - \Delta_{ci0} \geq 0 \tag{3.6}$$

where Δ_{ci0} represents a certain shortening of the top strut in the fan.

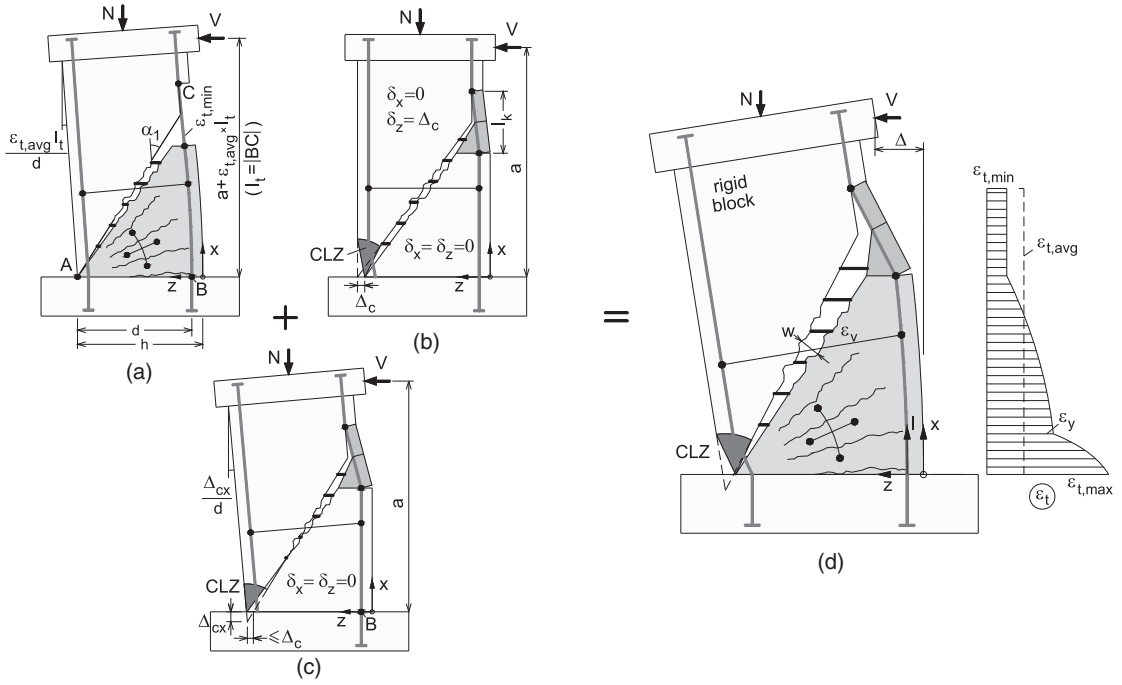

Figure 3.3: 3PK model for shear-dominated walls. (a) DOF $\varepsilon_{t,avg}$; (b) DOF Δ_c; (c) DOF Δ_{cx}; (d) deformed shape (B. I. Mihaylov, Hannewald, & Beyer, 2016).

3.2 Shear mechanisms

As discussed earlier, concrete members carry shear in a complex manner. The shear resisting mechanisms and their proportion are highly discussed and a lot of research is done on this matter.

A free body diagram as shown in Fig. 3.4 helps to identify the mechanisms. The mechanisms in the previously presented kinematic models are (B. Mihaylov et al., 2018):

- Aggregate interlock: local stresses across the critical diagonal crack.

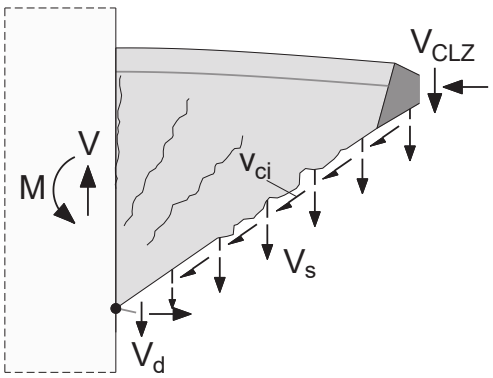

Figure 3.4: Shear mechanisms in short coupling beams. V_{ci} = aggregate interlock; V_{CLZ} = shear carried in critical loading zone; V_d = dowel action of longitudinal reinforcement; V_s = tension in the stirrups (B. Mihaylov, Liu, & Lobet, 2018).

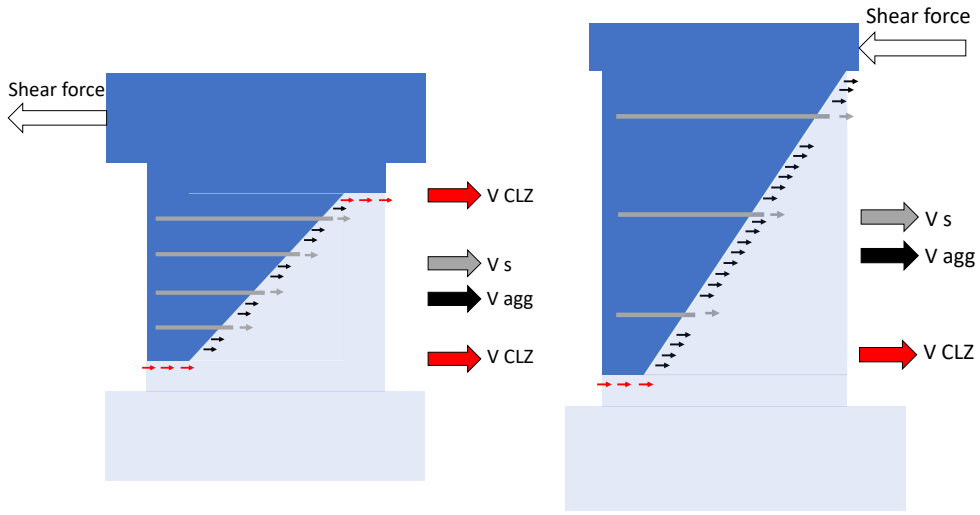

(a) Short coupling beam. (b) Short wall.

Figure 3.5: Free-body diagram with applied horizontal shear force and horizontal components of internal stresses.

- Critical loading zone: Inclined compressive stresses, projected onto the direction of the applied shear force, results in a shear component.

- Tension in the transverse reinforcement (stirrups): The stress in the stirrups in the critical diagonal crack give another shear resisting component.

- Dowel action of the longitudinal reinforcement: This component is associated with the bending of longitudinal reinforcing bars along l_k.

The paper by B. Mihaylov et al. (2018) gives expressions of the shear forces in function of the DOFs Δ_c and $\varepsilon_{t,avg}$.

In this work, shear-transfer actions should be evaluated based on experimental measurements, mostly thanks to the displacement field from the DIC. Such an analysis has already been done for slender reinforced concrete beams without transverse reinforcement by Cavagnis et al. (2018).

In the following, the investigation of the shear-transfer mechanisms is performed by considering the failure planes and the resulting rigid bodies sketched in Fig. 3.5. The internal stresses acting on the rigid body are also illustrated. The total shear force applied on the rigid body can be considered equal to the sum of all horizontal components of the shear-transfer actions: tension in stirrups V_s, agrregate interlock V_{agg} and shear transferred in the critical loading zone V_{CLZ}.

In the following sections, different formulations are given on which the results are based on. The measured kinematics as well as fundamental mechanical models are taken into account in this analysis. The dowel action is neglected in the present work.

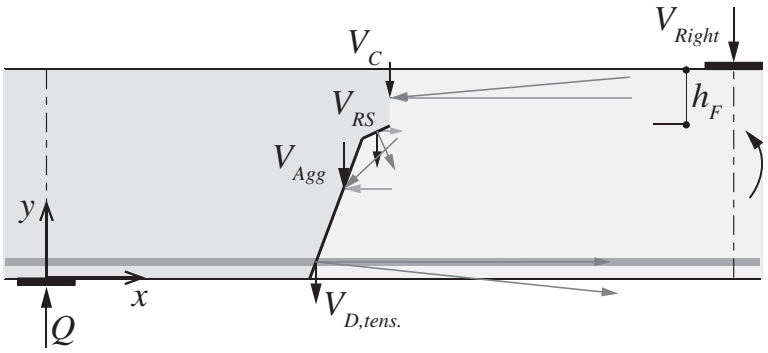

Figure 3.6: Free-body equilibrium and internal forces in a RC member (Cavagnis, Ruiz, & Muttoni, 2018).

3.2.1 Critical loading zone

The shear resisted in the critical loading zone is similar to the "Compression chord and arching action" in the case of more slender members. In the paper by Cavagnis et al. (2018), the contribution of the inclined compression chord and arching action, referred to as V_c (see Fig. 3.6), is calculated based on measured principal strains along a vertical section at the tip of a critical shear crack (of length h_f in Fig. 3.6). In the case of a shear wall and a short coupling beam, the critical diagonal crack get rather dispersed close to the end section. Those zones are highly stressed, which induces distortions and even crushing near failure. The previously described compression chord action for RC members can thus be interpreted as the mechanism carrying shear in the critical loading zone (CLZ) of shear walls and short coupling beams.

The CLZ is not dominated by a single dominant crack but rather by a series of little cracks and high compressive stresses. In order to evaluate the shear force transferred by this mechanism, a horizontal plane must be defined at a suitable height (ordinate). The shear force is then obtained by integrating horizontal shear stresses over this plane. A typical stress state expected in this region is depicted in Fig. 3.7. The definition of the plane in the case of deep members is not straightforward. The general expected trend for a wall or coupling beam as presented in Fig. 3.5 is the following: From top to bottom, the shear transferred along horizontal planes/cuts (V_{CLZ}) becomes smaller because more and more stress is transferred through aggregate interlock. When reaching the disturbed region close to the bottom end section characterized by little cracks, V_{CLZ} is expected to become messy because stresses are more chaotic. Therefore, the ideal free-body diagram (FBD) would be such that the switch from aggregate interlock V_{agg} to V_{CLZ} takes place when the individual crack starts to become rather dispersed resulting in several little cracks. The location of the plane will be discussed for the shear wall and the short coupling beam in their respective chapter.

The calculation of V_{CLZ} is thus performed on the basis of stresses along a horizontal plane. These stresses are obtained by considering principal strains along the plane and by adopting constitutive laws for concrete. The strain and stress calculation are presented in the following.

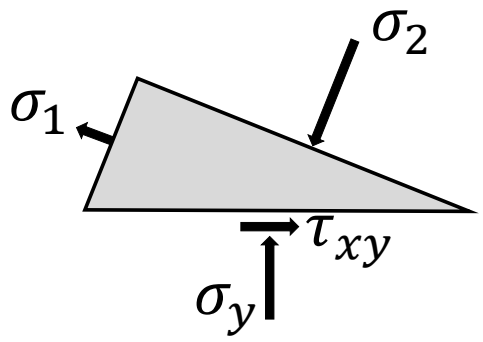

Figure 3.7: Schematic of typical stress state close to CLZ. σ_1 (maximum principal stress) and σ_2 (minimum principal stress) acting along principal stress directions. τ_{xy} (shear stress) and σ_y (normal stress) acting on horizontal plane.

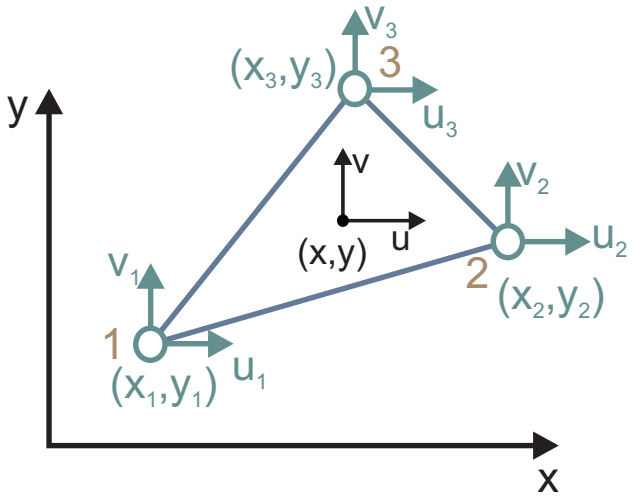

Figure 3.8: Constant Strain Triangle (Ponthot, 2016).

Strain calculation

The strain calculation is not performed in the DIC software. The measured displacement field is directly used to compute strains. The displacement field from DIC is given for points arranged in a regular grid. Those points will be used to form a finite element mesh and to compute the strains for each element. The mesh consists of triangles. The nodes are numbered in such a way that the first node is in the top left corner of the x-y coordinates grid, whereas the last node is the bottom right node. The triangles are defined "Constant Strain Triangles", also called "linear triangular elements", with 3 nodes and 6 DOFs, more precisely 2 DOFs per node: one horizontal and one vertical displacement component (see Fig. 3.8). The fundamental hypothesis of these elements is a linear displacement across the element:

$$u = \alpha_1 + \alpha_2\, x + \alpha_3\, y \tag{3.7}$$

$$v = \beta_1 + \beta_2\, x + \beta_3\, y \tag{3.8}$$

with α_i and β_i being the so-called internal parameters. Developing the strains, we get:

$$\varepsilon_{xx} = \frac{\partial u}{\partial x} = \alpha_2 \tag{3.9}$$

$$\varepsilon_{yy} = \frac{\partial v}{\partial y} = \beta_3 \tag{3.10}$$

$$\gamma_{xy} = 2\,\varepsilon_{xy} = \alpha_3 + \beta_2 \tag{3.11}$$

Those strains are thus constant, hence the name "Constant Strain Triangle".

The area of a triangle is given by

$$A = \frac{1}{2}\,det \begin{bmatrix} 1 & x_1 & y_1 \\ 1 & x_2 & y_2 \\ 1 & x_3 & y_3 \end{bmatrix} \tag{3.12}$$

The finite element formulation gives finally:

$$\begin{Bmatrix} \varepsilon_x \\ \varepsilon_y \\ \gamma_{xy} \end{Bmatrix} = \frac{1}{2A} \begin{bmatrix} y_{23} & 0 & y_{31} & 0 & y_{12} & 0 \\ 0 & x_{32} & 0 & x_{13} & 0 & x_{21} \\ x_{32} & y_{23} & x_{13} & y_{31} & x_{21} & y_{12} \end{bmatrix} \begin{Bmatrix} u_1 \\ v_1 \\ u_2 \\ v_2 \\ u_3 \\ v_3 \end{Bmatrix} \tag{3.13}$$

with $x_{ij} = x_i - x_j$ and $y_{ij} = y_i - y_j$.

Principal strains are obtained with the following equations, based on Mohr's circle:

$$\varepsilon_1 = \frac{\varepsilon_x + \varepsilon_y}{2} + \sqrt{\left(\frac{\varepsilon_x - \varepsilon_y}{2}\right)^2 + \left(\frac{\gamma_{xy}}{2}\right)^2} \tag{3.14}$$

$$\varepsilon_2 = \frac{\varepsilon_x + \varepsilon_y}{2} - \sqrt{\left(\frac{\varepsilon_x - \varepsilon_y}{2}\right)^2 + \left(\frac{\gamma_{xy}}{2}\right)^2} \tag{3.15}$$

A graphical representation of a general strain state is Mohr's Circle shown in Fig. 3.9. As a reminder, γ_{xy} calculated in Eq. (3.13) is called *engineering shear strain* and corresponds to a "total measure" of shear strain in x-y plane such that:

$$\gamma_{xy} = \varepsilon_{xy} + \varepsilon_{yx} = 2\,\varepsilon_{xy} \tag{3.16}$$

where $\varepsilon_{xy} = \varepsilon_{yx}$ is the average of two strains:

$$\varepsilon_{xy} = \frac{1}{2}\left(\frac{\partial v}{\partial x} + \frac{\partial u}{\partial y}\right) \tag{3.17}$$

The principal strain angle θ_p, or principal rotation angle, is obtained with:

$$\theta_p = \frac{1}{2}\,\arctan\left(\frac{\gamma_{xy}}{\varepsilon_x - \varepsilon_y}\right) \tag{3.18}$$

where the angle θ_p is of the same sign as γ_{xy} and $\theta_p \in [-90°, 90°]$. The angle θ_p is represented in Fig. 3.10. It corresponds to half the angle in Mohr's Circle.

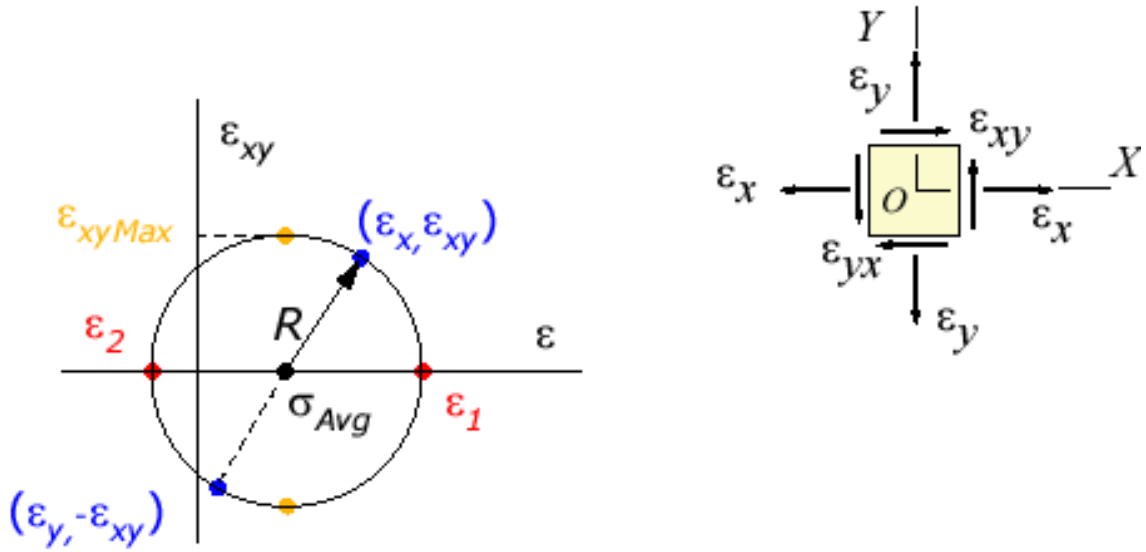

Figure 3.9: Mohr's Circle representation (left) for a general strain state in x-y coordinates (right). Source : https://www.efunda.com/formulae/solid_mechanics/mat_mechanics/mohr_circle_usage_strain.cfm

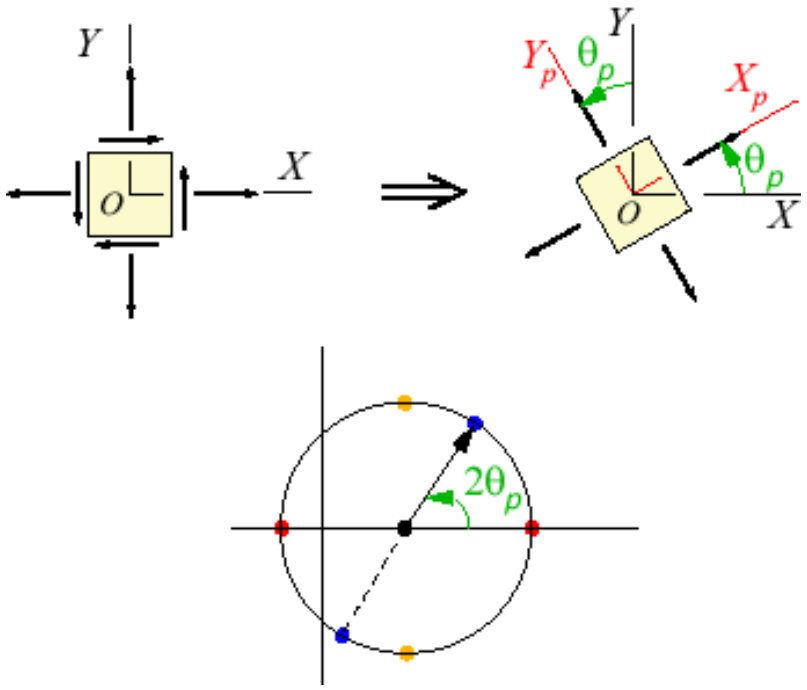

Figure 3.10: Comparison between general axis (X-Y) and principal axis (Xp-Yp). Source : https://www.efunda.com/formulae/solid_mechanics/mat_mechanics/mohr_circle_usage_strain.cfm

Stress calculation

In terms of stresses, one can only compute the average stress over an element thanks to the computed strain.

Constitutive laws are needed for the calculation of stresses. The principal stress directions are supposed to be equal to the principal strain directions defined by the principal strain angle θ_p.

Since concrete is a relatively complex material, different cases need to be accounted for depending on the strain state (Cavagnis et al., 2018).

- If $\varepsilon_1 < 0$ and $\varepsilon_2 < 0$, which can be referred to as biaxial compression, the stress-strain response of concrete in compression according to Popovics (1973) is used, without taking into account any confinement or compression softening. The principal stresses are calculated as follows:

$$\sigma_{1,2} = \frac{n\left(\frac{\varepsilon_{1,2}}{\varepsilon_{c1}}\right)}{n-1+\left(\frac{\varepsilon_{1,2}}{\varepsilon_{c1}}\right)^{nk}} f_c,\ [MPa] \tag{3.19}$$

  where n and k are calculated with

$$n = 0.8 + \frac{f_c}{17},\ [MPa] \tag{3.20}$$

  and

$$k = 0.67 + \frac{f_c}{62},\ [MPa]. \tag{3.21}$$

  The strain at maximum compression is obtained with

$$\varepsilon_{c1} = \frac{f_c}{E_c}\frac{n}{n-1}. \tag{3.22}$$

  The Young's modulus is, according to Eurocode 2,

$$E_c = 22000\left(\frac{f_c}{10}\right)^{0.3},\ [MPa] \tag{3.23}$$

  for quartzite aggregates[1].

- If $\varepsilon_1 \geq 0$ and $\varepsilon_2 \geq 0$, a biaxial tensile state must be considered. Tensile stresses are calculated with a linear-elastic stress-strain curve (Cavagnis et al., 2018). Therefore, before reaching its tensile strength, stresses are computed as $\sigma_{1,2} = E_c\,\varepsilon_{1,2}$. If the strain is higher than the cracking strain ε_{cr}, $\sigma_{1,2} = 0$. The cracking strain is given by $\varepsilon_{cr} = \frac{f_{ct}}{E_c}$ with $f_{ct} = 0.33\sqrt{f_c}, [MPa]$.

[1] If material properties are determined in the lab, the experimentally obtained modulus of elasticity of the concrete will be considered.

- If $\varepsilon_1 \geq 0$ and $\varepsilon_2 < 0$, the maximum principal strain ε_1 can either be $\leq \varepsilon_{cr}$ or $\geq \varepsilon_{cr}$. If $\varepsilon_1 \leq \varepsilon_{cr}$,

$$\sigma_1 = E_c \, \varepsilon_1. \tag{3.24}$$

Otherwise, $\sigma_1 = 0$. The principal compressive stress is calculated according to a stress-strain relationship taking into account the pre- and post-peak behavior (Ruiz, Muttoni, & Gambarova, 2007) (see Fig. 3.11(a)):

$$\sigma_2 = \frac{E_c \, \varepsilon_2}{1 + \left(\dfrac{\varepsilon_2}{\varepsilon_0}\right)^{\alpha}} \tag{3.25}$$

with

$$\varepsilon_0 = \frac{\alpha \, f_{c,eff}}{E_c \, (\alpha - 1)^{(1-1/\alpha)}} \tag{3.26}$$

and

$$\alpha = 0.5 + \frac{f_{c,eff}}{20} + \frac{f_{c,eff}^2}{1500} \tag{3.27}$$

where $f_{c,eff}$ is the effective compressive strength [MPa].
An approach suitable for smeared cracking within the compression zone will be adopted. Indeed, according to Vecchio and Collins (1986), cracked concrete is softer and weaker than concrete in a standard cylinder when subjected to high tensile strains normal to the principal compression direction. The effective compressive strength is therefore reduced due to compression softening effects. The following law proposed by Vecchio and Collins (1986) is used:

$$f_{c,eff} = f_c \frac{1}{0.8 + 170 \, \varepsilon_1} \leq f_c \tag{3.28}$$

The value of the compressive strength from Eq. (3.28) can then be used in Eq. (3.27) and (3.26) to compute σ_2. It is important to note that Eq. (3.28) computes very low values for high tensile strains. If α is less than 1, complex values will be computed for ε_0. This is the case if

$$\frac{f_{c,eff}}{20} + \frac{f_{c,eff}^2}{1500} \leq 0.5 \tag{3.29}$$

or if $f_{c,eff} < 8.94, \ [MPa]$, which, in turn, is the case if

$$\varepsilon_1 > \frac{1}{170} \left(\frac{f_c}{8.94} - 0.8 \right) \tag{3.30}$$

For example, for $f_c = 50, \ [MPa]$, complex values will be computed if $\varepsilon_1 > 0.028$. Those strain values are not unusual in main cracks. However, in the critical loading zone, smaller maximum principal strain values are computed such that the law by Vecchio and Collins is locally applicable.

Two alternative approaches will be used in order to see the impact of the constitutive law on the shear strength calculation (V_{CLZ}):
Cavagnis et al. (2018) express $f_{c,eff}$ for uncracked concrete based on Kupfer's

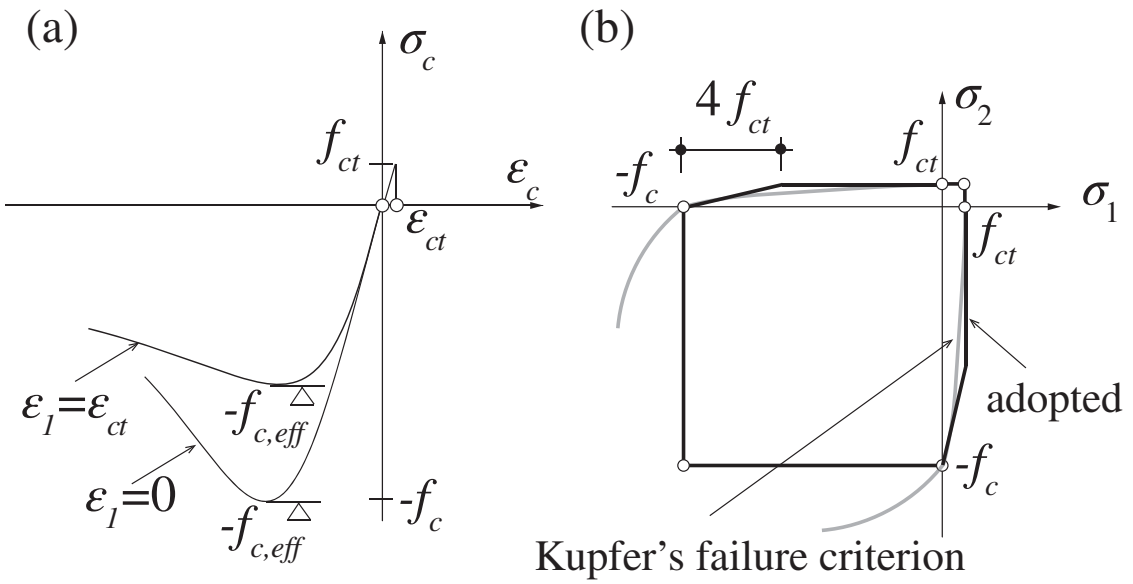

Figure 3.11: (a) Stress-strain diagram for concrete; (b) Kupfer's failure criterion (Kupfer, Hilsdorf, & Rusch, 1969) and adopted one (Cavagnis, Ruiz, & Muttoni, 2018).

biaxial failure surface, accounting for the interaction between tension and compression stresses. Thus, the same criterion is adopted for the critical loading zone, when $\varepsilon_1 \leq \varepsilon_{cr}$. As can be seen in Fig. 3.11(b), the failure surface in the quadrants corresponding to a combination of tension-compression is simplified as a bi-linear law. This law indicates that for σ_1 varying between 0 and f_{ct}, the compressive strength of the concrete in the orthogonal direction $f_{c,eff}$ varies between f_c and $f_c - 4\,f_{ct}$. In regions with $\varepsilon_1 > \varepsilon_{cr}$, $f_{c,eff}$ will be taken equal to $f_c - 4\,f_{ct}$.

The second alternative is an uniaxial compression law for σ_2 disregarding any biaxial effects (Eq. (3.19)).

In Fig. 3.12, the three approaches for the tension-compression regime are illustrated in terms of $f_{c,eff}$.

The use of compression softening equations requires some additional considerations. The compression softening effect is taken into account in the formulation proposed by Vecchio and Collins (1986) because, as suggested by the authors, cracked concrete subjected to high tensile strains is softer and weaker in the compression direction. The compressive strength is therefore reduced. The softening represents a gradual decrease of mechanical resistance due to increased deformation and cracking and it is commonly related to the reinforcement that bridges the cracks and weakens the concrete in the vicinity. However, in the two applications of this thesis, only a small amount of transverse reinforcement is employed. As a consequence, the smeared cracking might be less pronounced and the compression softening law might thus be not well adapted.

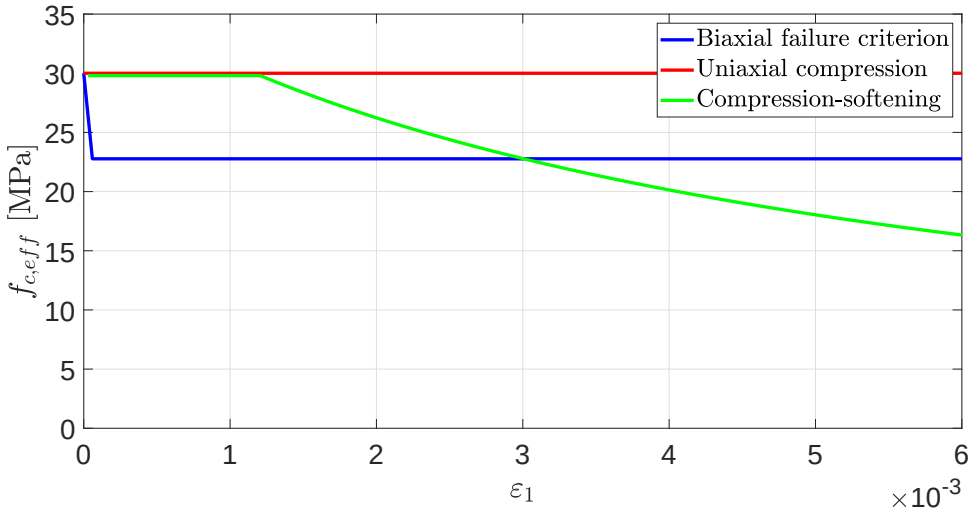

Figure 3.12: Different laws used for $f_{c,eff}$ in function of the principal tensile strain for $f_c = 30\ MPa$. The biaxial failure criterion refers to the simplified bilinear law based on Kupfer's failure surface, the uniaxial compression law refers to Popovics (1973) and the compression softening law refers to Vecchio and Collins (1986).

From the principal strains and principal stress directions, shear stresses can be computed and integrated over a plane defining the critical loading zone. To do so, Mohr's circle representing the stress state is established (Fig. 3.13). The stress corresponding to the origin of the circle is $\sigma_o = \sigma_2 + \dfrac{\sigma_1 - \sigma_2}{2}$ and the radius of the circle is $R = \dfrac{\sigma_1 - \sigma_2}{2}$. Thus, we obtain

$$\sigma_x = \sigma_0 + R\,\cos 2\,\theta_p \tag{3.31}$$

$$\sigma_y = \sigma_0 - R\,\cos 2\,\theta_p \tag{3.32}$$

$$\tau_{xy} = R\,\sin 2\,\theta_p \tag{3.33}$$

V_{CLZ} is then computed by integrating τ_{xy} over the defined plane.

3.2.2 Aggregate interlock

Aggregate interlock is considered to be an important mechanism of shear transfer across cracks. As can be seen in Fig. 3.6, Cavagnis et al. (2018) computed the aggregate interlock in the critical shear crack. A similar approach will be used for the short coupling beam and shear wall.

Several models have been proposed to compute normal and tangential stresses in the crack allowing the transfer of shear forces. Those stresses develop through contact of the two faces on either side of the rough crack. In general, the basis of all these models are the crack kinematics, more precisely the crack width (or opening) and crack slip (or sliding) in the crack. The sliding can induce the aggregate to interlock with the cement matrix of the opposite crack surface. This can result in a

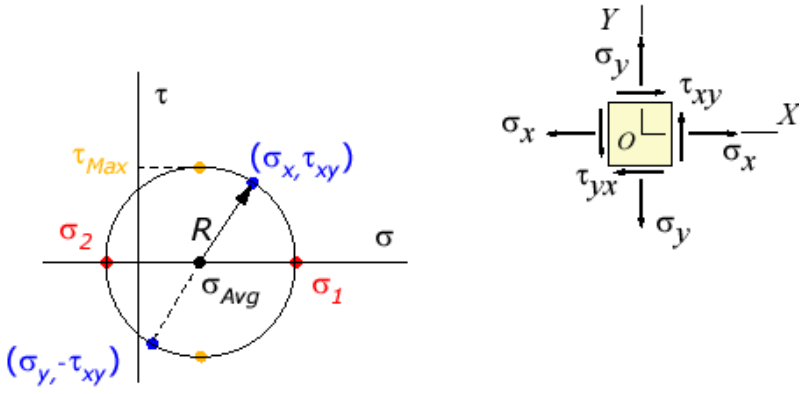

Figure 3.13: Mohr's circle representation of a stress state. Source: https://www.efunda.com/formulae/solid_mechanics/mat_mechanics/mohr_circle_usage.cfm

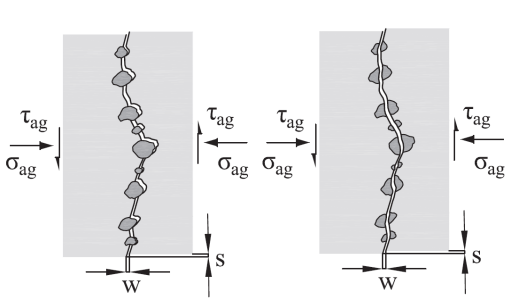

(a) Stresses transferred across a rough crack (left) and smooth crack (right) (Huber, Huber, & Kollegger, 2016).

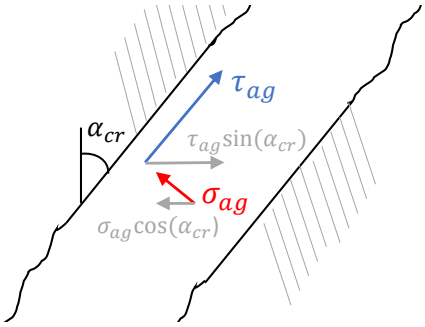

(b) Inclined crack with horizontally projected stress components in case of horizontally applied shear forces.

Figure 3.14: Aggregate interlock stresses: normal stresses σ_{ag} and tangential stresses τ_{ag}.

transfer of stresses across the crack (Huber, Huber, & Kollegger, 2016).

The first step consists in the computation of crack kinematics along the critical shear crack. In the next step, shear and normal stresses are calculated in the crack based on the crack width and the slip.

The resulting shear strength by aggregate interlock V_{agg} is computed by integration of the stresses projected on a plane parallel to the applied shear forces. Fig. 3.14 shows schematic representations of interlock stresses. The shear resistance by aggregate interlock V_{agg} is thus computed as:

$$V_{agg} = b \cdot \left(\int_{crack} \tau_{ag} \, \sin \alpha_{cr} \, \mathrm{d}l - \int_{crack} \sigma_{ag} \, \cos \alpha_{cr} \, \mathrm{d}l \right), \tag{3.34}$$

where b is the width of the element and α_{cr} is the crack angle with respect to the vertical axis.

In the following sections, the calculation of crack kinematics as well as three crack models are presented. V_{agg} will be computed with all three models for comparison.

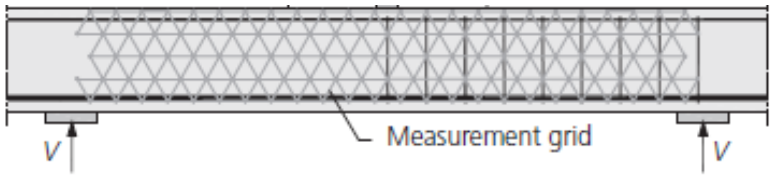

Figure 3.15: Grid of targets in experimental setups (Campana, Anastasi, Ruiz, & Muttoni, 2013), cropped.

Crack kinematics

Cavagnis et al. (2018) approximated the shape of the crack by a polyline, connecting points spaced at maximum 16 mm. They use the approach proposed by Campana, Anastasi, Ruiz, and Muttoni (2013) in order to calculate crack width and slip based on the DIC measurements. The method by Campana et al. (2013) is developed to compute crack kinematics from discrete measurements. The discrete measurements consists of targets arranged as a grid of equilateral elements (see Fig. 3.15). In order to determine the kinematics of the cracks, a rigid body is considered at both sides of the crack. The displacement field of each rigid body is determined by using the coordinates of two targets, as seen in Fig. 3.16. While this method gives reasonable values for slender elements like beams, as analyzed by Cavagnis et al. (2018) and Campana et al. (2013), the same formulation applied on shear walls and coupling beams produced abnormal results. The method might not be suitable for deep members.

Another example from literature for calculation of crack kinematics based on DIC is presented by Huber et al. (2016). They analyzed cracks in reinforced concrete beams. Huber et al. (2016) also idealized the cracks by a polyline, two points being separated by approximately 3 facets. In their case, a facet has a size of 15 pixels. For a given crack, they record about 50 data points. By means of the crack angle and the displacement of two opposite facets, crack opening and crack sliding can be determined. A detailed methodology is not described.

The previous examples from literature were not sufficient or suitable for crack analysis applied on the coupling beam and shear wall. Therefore, a new method was established and will be described in the following:

The first step consists in fragmenting the crack into several crack units. To do so, a polyline is defined with points c (c_x, c_y) in the crack separated by a given vertical distance. For each defined segment, a reference point is defined in the crack similar to point f in Fig. 3.16(a). Four neighboring points $P1$ to $P4$ are selected as well. This is done manually on a plot of maximum principal strains where the cracks are traceable.
The crack angle is determined for each crack unit using the coordinates of the delimiting points (c_x and c_y). Similarly to the method by Campana et al. (2013), the displacement of two rigid bodies on either side of the crack must be determined. For the left rigid body, points $P1$ and $P2$ will determine the displacement field and the displacement of the point in the crack. For the right rigid body, points $P3$ and $P4$ are used to determine the displacement of f with respect to the right body

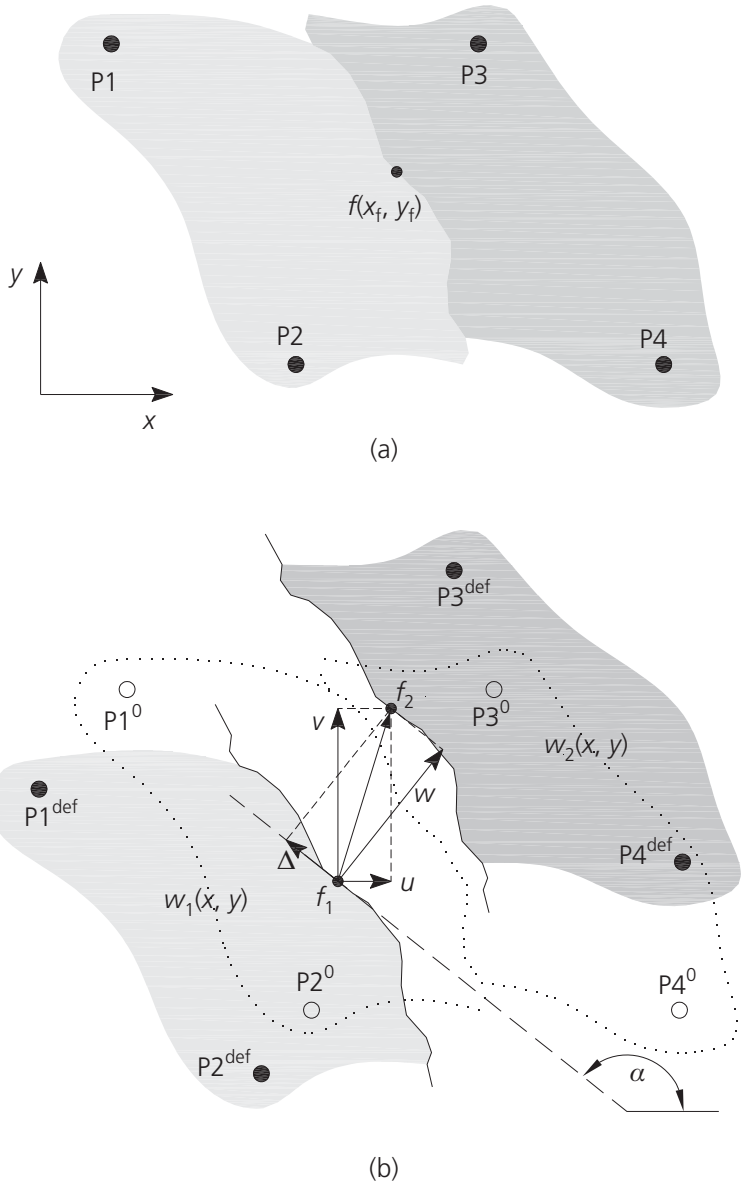

Figure 3.16: Calculation of crack kinematics; (a) undeformed configuration; (b) deformed configuration.

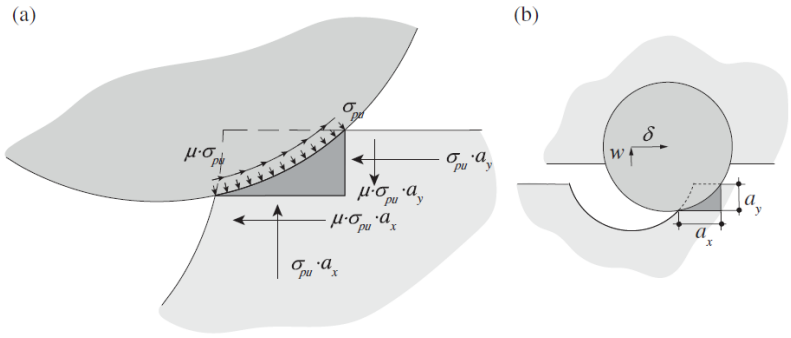

Figure 3.17: (a) Contact zone between aggregate and cement matrix and aggregate interlock stresses; (b) Projections areas according to the kinematics proposed by Walraven (Cavagnis, Ruiz, & Muttoni, 2018).

motion. The complete approach including the calculation of the displacement fields as well as the calculation of crack width and slip is presented in Appendix A.

Two-phase Model

Walraven (1980) established a theory assuming that crack sliding δ only occurs after crack opening w. He considered the concrete to be a two-phase system consisting of a cement matrix and aggregates idealized as rigid spheres (Fig. 3.17). The model, often referred two as two-phase model (TPM) is based on statistical and geometrical considerations of the crack surfaces and the contact areas (Cavagnis et al., 2018). Compressive stresses and shear stresses are computed as follows:

$$\sigma = \sigma_{pu} \left(A_x - \mu \, A_y \right) \tag{3.35}$$

$$\tau = \sigma_{pu} \left(A_y + \mu \, A_x \right) \tag{3.36}$$

with

- σ_{pu} : compressive plastic strength of the cement
- μ : friction coefficient, taken as equal to 0.4
- A_x : average contact area between the cement matrix and the aggregates parallel to the crack surface
- A_y : average contact area between the cement matrix and the aggregates perpendicular to the crack surface

Contact Density Model

Another model allowing to calculate the stress transfer across cracks in concrete is the Contact density model (CDM) proposed by Li, Maekawa, and Okamura (1989).

As can be seen in Fig. 3.18, the complex asperity of a crack is divided into small "contact units" with inclinations θ.

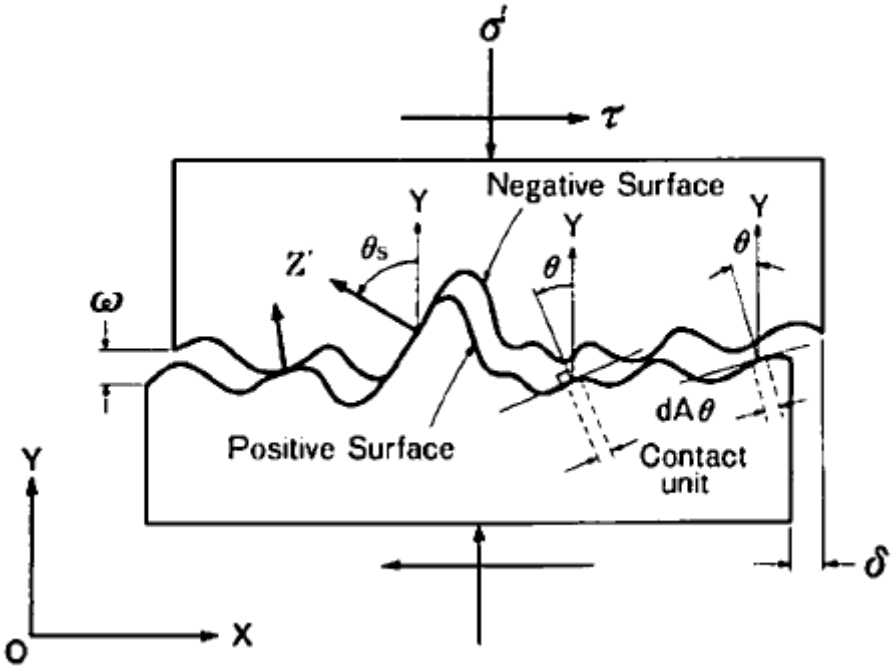

Figure 3.18: Definitions and notations of the CDM (Li, Maekawa, & Okamura, 1989).

Due to a certain crack width and slip, some contact units get in contact and resist shear and compressive stresses.

The Contact Density model is based on two proposals and three assumptions. The two proposals are summarized as follows:

- A crack plane is composed of a number of areas, also called contact units. Those areas are inclined by θ, ranging from $-\frac{\pi}{2}$ to $\frac{\pi}{2}$. The inclinations θ can be described by a contact density probability function $\Omega(\theta)$.
- The contact stress is proposed to be normal to the contact direction θ.

Three assumptions can be described as follows:

- $\Omega(\theta)$ is a trigonometric function, independent on size and grading of aggregates, expressed by $\Omega(\theta) = 0.5 \cos\theta$, shown in Fig. 3.19.
- An elasto-perfectly plastic model is used to compute the contact stress.
- $K(w)$ refers to the effective ratio of contact area and expresses the loss of contact if the crack width w is large compared to the roughness of the crack faces, illustrated in Fig. 3.20.

The contact compressive force Z' (see Fig. 3.18) is defined as the force applied by the positive surface on the negative surface. By multiplying the contact stress with the effective contact area:

$$Z' \, \mathrm{d}\theta = \sigma_{con}(\theta) \, K(w) \, A_t \Omega(\theta) \, \mathrm{d}\theta \tag{3.37}$$

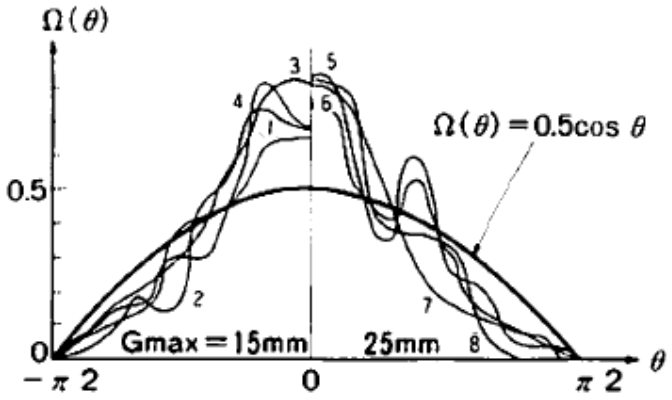

Figure 3.19: Contact density of each direction (Li, Maekawa, & Okamura, 1989).

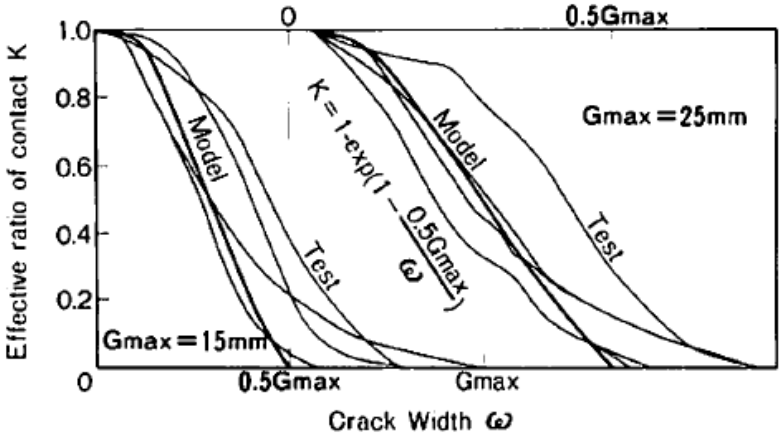

Figure 3.20: Effective ratio of contact area K, model and measured (Li, Maekawa, & Okamura, 1989).

where A_t is the surface area of the crack, considered to be equal to 1.27 times the sectional area of crack plane (crack plane being the X-axis in Fig. 3.18).

By integrating the X and Y-components of Z', we obtain respectively the shear (τ) and normal stresses (σ) transferred in the plane:

$$\tau = \int_{-\frac{\pi}{2}}^{\frac{\pi}{2}} Z'(w, \delta, \theta) \, \sin\theta \, \mathrm{d}\theta \tag{3.38}$$

$$\sigma = \int_{-\frac{\pi}{2}}^{\frac{\pi}{2}} Z'(w, \delta, \theta) \, \cos\theta \, \mathrm{d}\theta \tag{3.39}$$

Pure Mechanics Crack Model

The Pure Mechanics Crack Model (PMCM) proposed by Calvi, Bentz, and Collins (2017) is a simple rational crack behavior model for cracks subjected to cyclic shear and axial loads based on global and local equilibrium, compatibility and stress-strain relationships.
More precisely, the model can be used to predict the behavior of cracks and to estimate the stress-state based on crack measurements.

The constitutive relations used in the model are of particular interest. The models refers to an empirical expression derived by Vecchio and Collins (1986), which has been widely used since then:

$$\nu_{ci} = 0.18 \cdot \nu_{ci,max} + 1.64 \cdot f_{ci} - 0.82 \cdot \frac{f_{ci}^2}{\nu_{ci,max}} \tag{3.40}$$

where $\nu_{ci,max}$ is given by

$$\nu_{ci,max} = \frac{\sqrt{f'_c}}{0.31 + \frac{24 \cdot w}{a_g + 16}}, \tag{3.41}$$

which expresses the shear stress transmitted across a crack. f'_c is the concrete compressive strength [MPa], w is the crack width [mm] and a_g is the maximum aggregate size [mm]. For a given crack width, Eq. (3.40) gives a relation between the compressive stress f_{ci} and the shear stress ν_{ci}. The relationship and the comparison with two experimental tests is illustrated in Fig. 3.21. It can be seen that also tensile normal stresses can be obtained with PMCM.

Another basis of PMCM is the relationship between crack width and crack slip, which defines the crack contact plane (angle α) (see Fig. 3.22 and Eq. (3.42)):

$$\tan(\alpha) = \frac{w}{s} \tag{3.42}$$

As shown in Fig. 3.22, a vertical force ν_{ci} and a horizontal force f_{ci} must be transmitted at the contact point. Eq. (3.43) expresses the evolution of crack stresses as a function of crack geometry. This relation can also be seen in Fig. 3.23. Since a

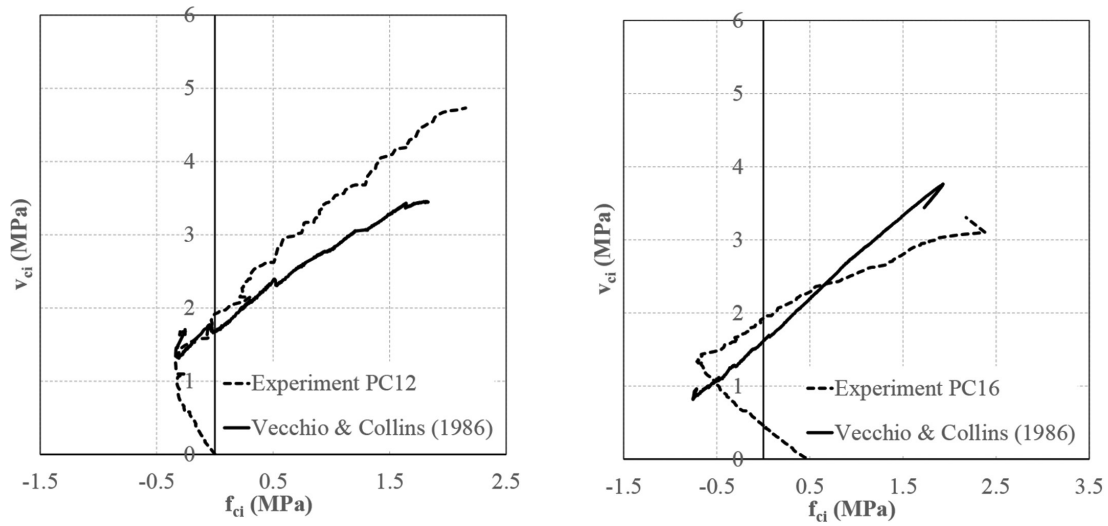

Figure 3.21: Relationship between shear stress v_{ci} and normal stress f_{ci} (Calvi, Bentz, & Collins, 2017).

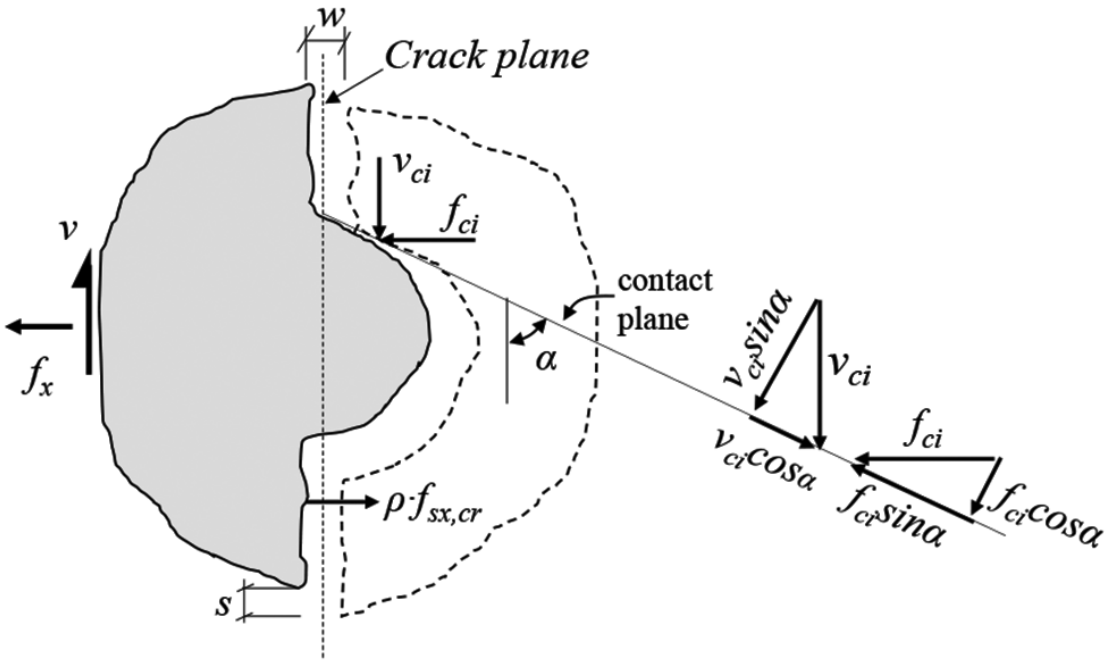

Figure 3.22: Free-body diagram of aggregate at contact point at loading (Calvi, Bentz, & Collins, 2017).

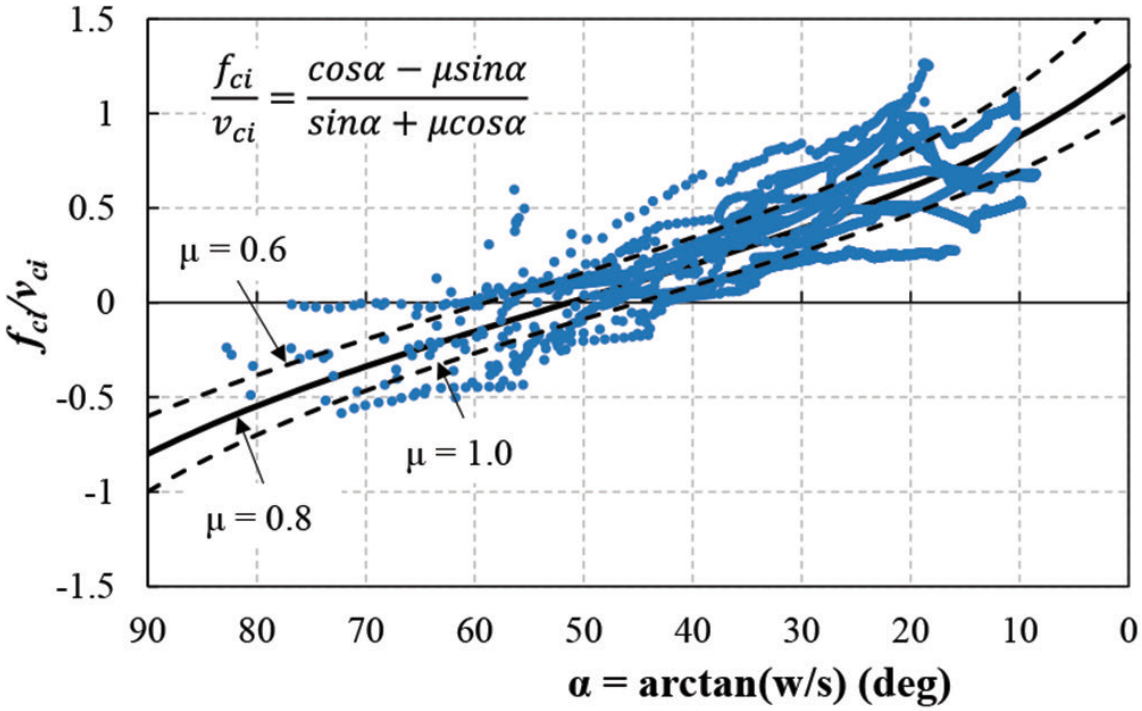

Figure 3.23: Relationship between crack geometry and crack stresses (Calvi, Bentz, & Collins, 2017).

friction coefficient value of 0.8 produces a curve that approximate the experimental results (dots) in a good way, this value will be adopted for calculations.

$$\nu_{ci} = \frac{f_{ci} \cdot (\sin\alpha + \mu \cdot \cos\alpha)}{\cos\alpha - \mu \cdot \sin\alpha} \tag{3.43}$$

The shear stress ν_{ci} and normal stress f_{ci} are therefore computed thanks to the combination of Eq. (3.40), (3.42) and (3.43).

Comparison of crack models

Fig. 3.24 shows a comparison of shear and normal stresses in function of crack width and slip. In the figure, shear stresses are considered positive and normal compressive stresses negative. Generally speaking, for higher compressive strength of concrete all three models produce both higher shear and normal stresses. Shear stresses and normal stresses increase globally with slip and decrease with crack width.
It can be seen that the contact density model computes generally higher values compared to the other two models.
Shear stresses are smaller than normal stresses (in absolute value) for small crack width (0.1 and 0.8 mm), whereas in general, shear stresses are higher.
The PMCM model is the only model able to compute tensile normal stresses, for example for a slip of 0.8 mm and crack width of 1.5 mm or higher.

3.2.3 Stirrups

The investigated shear wall and short coupling beam are slightly reinforced by stirrups. Tensile stresses in the diagonal crack are redistributed to the shear rein-

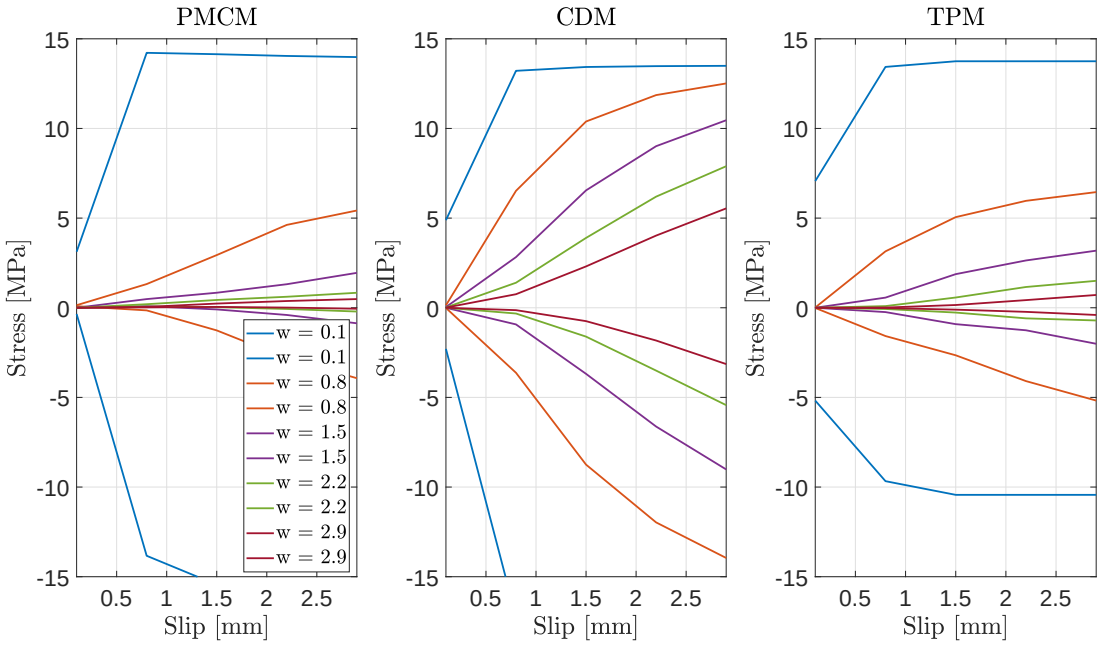

Figure 3.24: Interlock stresses (shear stress τ defined positive, compressive normal stress σ defined negative) according to the the Pure Mechanics Crack Model (PMCM), Contact Density Model (CDM) and Two-Phase Model (TPM) in function of slip and crack width (w). Maximum aggregate size = 16 mm, concrete compressive strength $f_c = 30\ MPa$.

forcement.

The shear force carried by a single stirrup is calculated as

$$V_{s,i} = \frac{\sigma_s \, \pi \, d^2}{4} \tag{3.44}$$

where d is the diameter of the stirrup and σ_s is the stress in the stirrup at the location of the crack. Campana et al. (2013) pointed out that even small crack width can cause the stirrups to yield. The shear test on the shear wall and the short coupling beam causes relatively wide cracks such that the stirrups are assumed to be yielding. However, stirrups very close to the end sections should not necessarily be accounted for because they are not crossing the critical shear crack and the crack width is much smaller in those regions. For yielding stirrups, the stress in the steel should be taken as the yielding stress. The total shear strength from the stirrups is calculated as the sum of the contribution of each stirrup.

Chapter 4

Results: Short Wall

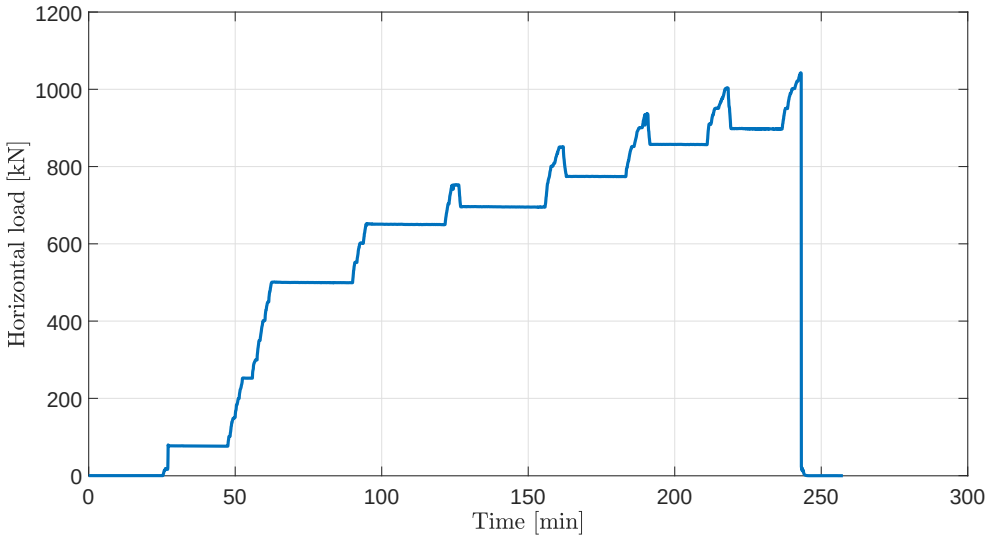

Figure 4.1: Evolution of applied horizontal load.

In this chapter, the behavior of the wall during the test will be described. The DIC measurements will be validated by comparing them with other experimental measurements. Then, the observed deformation of the wall will be compared to the kinematic model. In the last section, the shear-resisting mechanisms will be evaluated and compared to the applied shear force.

4.1 Global observed behavior

In this section, the global behavior of the wall under shear loading will be described. The load steps as well as the load-displacement curve will be presented. Finally, the failure mode will be illustrated.

In terms of load sequence, the wall was first loaded by an vertical load of 1200 kN followed by several load steps where the shear force increased step by step. The evolution of the applied horizontal force can be seen in Fig. 4.1.

The sequence of the test was as follows:

- Load step B0: During this reference step, no load is applied to the specimen. The cameras connected to the DIC system take photographs of the wall at rest.
- Load step B1: The wall was first gradually loaded by a vertical load up to 1200 kN. This force was kept constant during the following load steps.
- Load step B2: The horizontal load increased from 0 kN to 77 kN.
- Load step B3: The horizontal load increased up to 500 kN, with an intermediate pause at about 250 kN.
- Load step B4: The horizontal load increased up to 650 kN.

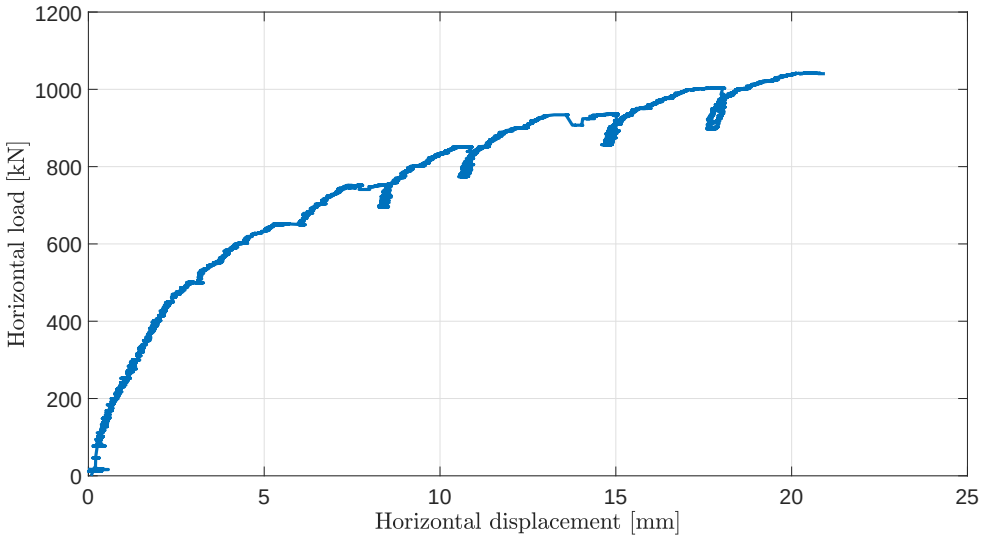

Figure 4.2: Load-displacement curve.

- Load step B5: The horizontal pressure was increased to 750 kN and then decreased to 700 kN for safety reasons during the load stop.
- Load step B6: The horizontal forces reached 850 kN, then was reduced to 775 kN during investigations.
- Load step B7: The horizontal force reached approximately 935 kN.
- Load step B8: The force increased from 857 kN to 1000 kN and was then reduced to 900 kN.
- Load step B9: The horizontal force increased gradually until reaching 1042 kN when a sudden and brittle failure took place. The vertical force was still at 1208 kN at that point. After failure, the forces both for the horizontal and vertical actuator were suddenly removed.

The load-displacement response in Fig. 4.2 shows the load in function of the measured horizontal displacement[1] at the top of the wall. In the beginning of the test, the wall was relatively stiff. However, when the shear force increased, cracks formed on the tension side of the wall. This led to a gradual loss of stiffness, which is represented by the flattening force-displacement curve. When the shear force reached 500 kN, 3 cracks initiated on the tensile side, in the lower part of the wall. When the load increased, more cracks formed, also in the middle part, and propagated towards the base as seen in Fig. 4.3a. When the load increased to 750 kN, many cracks arrived close to the foundation. A diagonal crack formed and reached almost the top corner. Up to a load of 850 kN, cracks become wider and new cracks formed below the diagonal crack. With an increased load (up to 935 kN), additional diagonal cracks formed reaching up to the top corner and down to the bottom block. When the load increased further, cracks became wider (see Fig. 4.3b).

[1]The top displacement was deduced from LED measurements.

(a) After load step B4.

(b) After load step B8.

Figure 4.3: Crack pattern at two different load steps.

When the force reached 1042 kN and the horizontal displacement was 21 mm, the wall failed. Since the experiment is force-controlled, which means that only the force of the actuators can be regulated, the applied force was immediately set to zero when failure occurred. The failure mode was diagonal tension failure. A major diagonal crack developed during loading. The wall finally failed in shear along this diagonal crack.

The cameras connected to the DIC system took photos every half a second. The pictures in Fig. 4.4 show the instant right before, during and after failure. It can be seen that the failure causes a block of concrete, located between the critical diagonal crack and a neighboring crack, to spall. Additional photos of the specimen after failure are shown in Fig. 4.5. It can be seen that the compression zone in the bottom left part of the wall was highly stressed in compression, as shown by the disintegration of concrete. The principal diagonal crack is slightly curved.

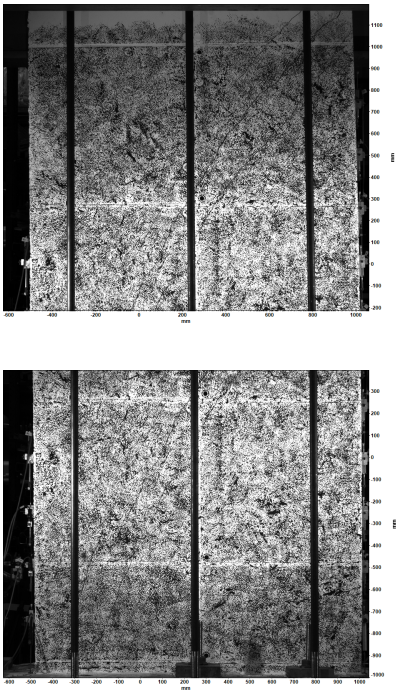

(a) Instant right before failure.

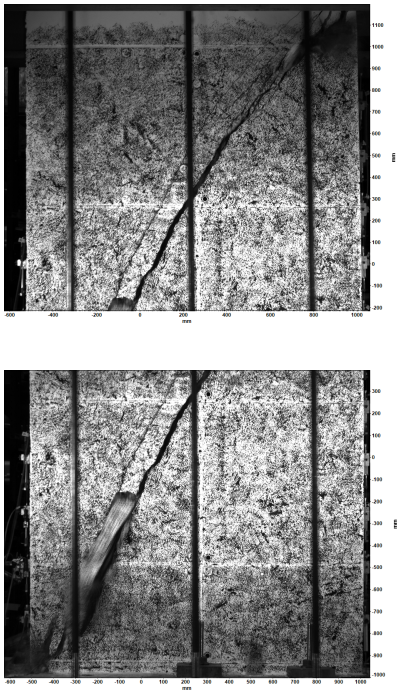

(b) At failure.

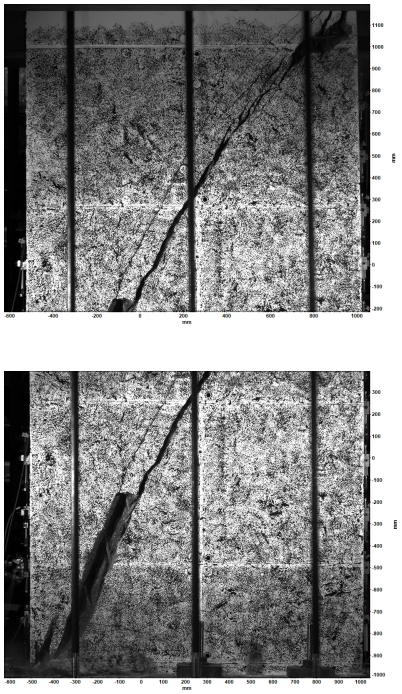

(c) Instant right after failure.

Figure 4.4: Pictures taken by DIC system before, during and after failure, within a span of 1,5 seconds. The top and bottom photographs correspond to the camera focusing respectively on the top and bottom part of the wall.

(a) Global view.

(b) Close-up of top right corner (tension side).

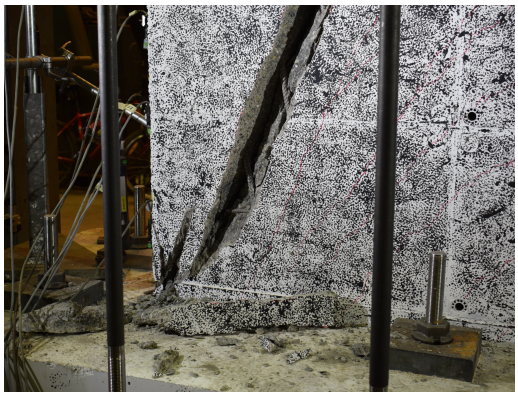

(c) Close-up of bottom left corner (compression side).

(d) Close-up of bottom compression side.

Figure 4.5: Specimen after failure.

4.2 Validation of DIC measurements

It is important to compare the DIC data with the recorded data from displacement transducers (DT). Indeed, this can help to validate the displacement field from DIC. In addition to DT measurements, a LED system consisting of 54 targets was installed. Tracking the displacement of each LED gives overall information about the displacement field and deformations. More precisely, the coordinates of the LEDs are recorded during the loading. Therefore, a comparison with LED targets could also be done for some measurements.

4.2.1 Processing of DIC data

The results in section 4.2 are based on the original calibration with the following parameters:

- The experimental setup was defined as 2 independent cameras.
- 6 views per camera.
- Camera 1 : Scale factor = 1.46784 px/mm, thus a pixel size of 0.68127 mm; RMS of the fit = 0.483 px.
- Camera 2 : Scale factor = 1.46706 px/mm, thus a pixel size of 0.68164 mm; RMS of the fit = 0.503 px.

The RMS (root-mean-square) of the fit reflects the quality of the calibration. As recommended by Lavision (2015), the average deviation of the dewarped mark positions to the ideal regular grid (RMS) should preferably be lower than 1 pixel. A value lower than 0.3 pixel is excellent, whereas values bigger than 2 pixel are questionable.

The results are obtained with following processing parameters:

- Subset size: 51 px
- Step size: 13 px
- Accuracy: medium
- Smoothing filter and outlier filter enabled
- Maximum expected displacement: 200 px

Other comparisons were done with the same parameters, but smaller subset sizes (e.g. 31 px and 15 px) and respective step sizes (e.g. 8 px and 4 px). The data points in the bottom frame, for a step size of 13 px and a pixel size of 0.68127 mm/px are at a distance of 8.86 mm.

The DIC data is computed for 36 instants. To do so, the pictures from load step B9 (864 pictures) were appended to the pictures of the reference step B0 (60 pictures). In this set of pictures (in total 924 pictures), every 25th picture (every 12.5 seconds) in the range 1-876 was processed. Failure occurred at picture 870. The processed data set thus comprises 36 instants. The data from the different systems are compared for the 32 instants during cycle B9 and before failure.

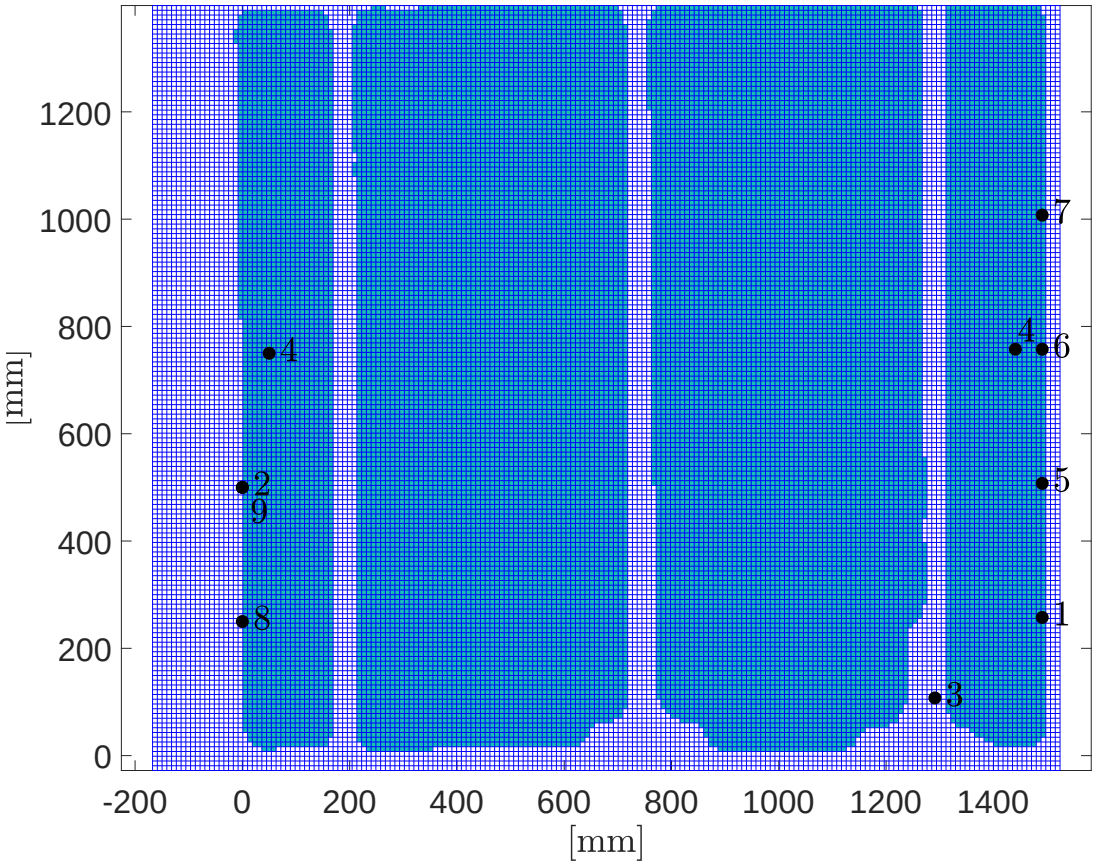

Figure 4.6: Location of points used to compare DIC measurements to DT measurements.

4.2.2 Comparison with DT and LED measurements

The comparison between DIC and DT measurements is done for discrete points. In fact, the displacement transducers measure the relative displacement between two points. In order to compare DIC to DT, the relative displacement between two data points from DIC analysis should be considered. These data points should be close to the measurement points of the DTs. Fig. 4.6 shows the mask (region of interest) used for the bottom frame of the wall in the DIC software. The grid of blue lines represents the grid of data points, such that at each intersection, the displacement field is calculated. The black dots show the location of the DIC data points used for comparison.

The second comparison is between DIC and LED measurements. The numbering of the LED targets is given in Fig. 4.7. The output data from LED consists of the coordinates of each LED. The coordinates were recorded for each load step separately. The theoretical grid of targets is shown by horizontal and vertical lines in Fig. 4.8. It can be seen that the blue crosses corresponding to the measured coordinates in load step B0 (no loading) slightly deviate from the theoretical regular 2D grid. The measured coordinates were corrected by a uniform translation and rotation about the bottom left target position. The corrected coordinates are

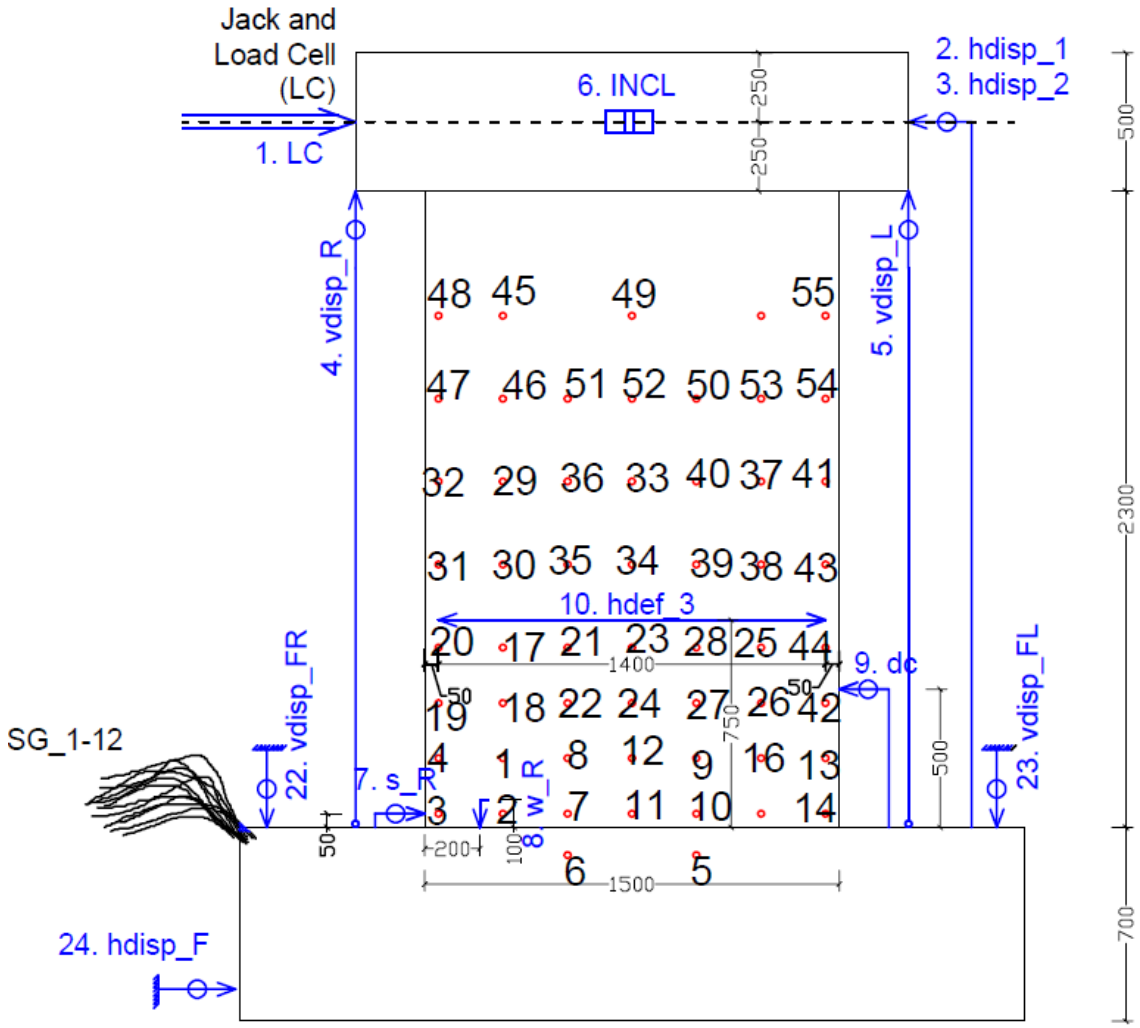

Figure 4.7: Numbering of LED targets.

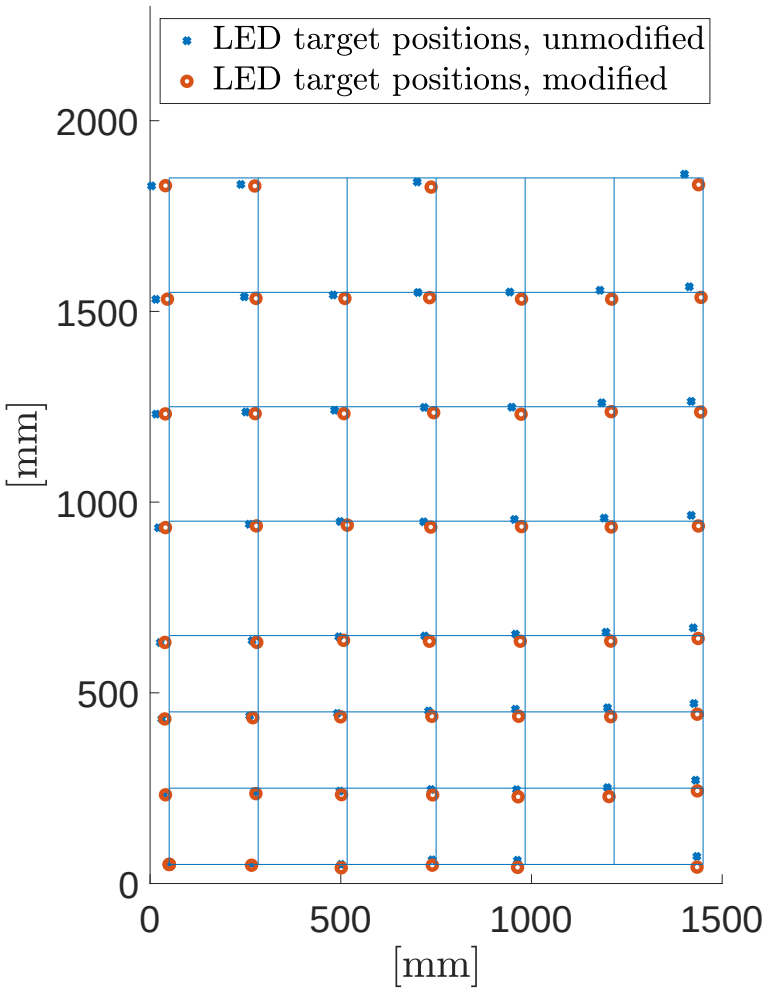

Figure 4.8: LED target positions on theoretical position grid.

represented by red circles. This correction was applied to all data from LED. The displacement of one LED target at a given load step is simply computed from the difference in coordinates (position) between the load step and the reference coordinates (reference position).

The position of the LED is recorded every half a second. The data is saved to a separate file for each load step. The start and the end of the recording is not synchronous with the DIC data acquisition, which complicates a good correlation between the data from those systems.

The following measurements were compared. The *measurement point* refers to the numbering of the data point (DIC system) in Fig. 4.6, while the number of the DTs and the LEDs are shown in Fig. 4.7.

- At measurement point 1, the absolute vertical displacement will be calculated and compared to DT n°11 ($vdef\_R1$) and to the vertical displacement of LED n°4.
- At measurement point 2, the absolute horizontal displacement will be calculated and compared to DT n°9 (dc) and to an interpolation of the horizontal displacement between LED n°44 and LED n°42.
- At measurement point 3, the vertical displacement will be compared to DT n°8 (w_R). Since the point 3 is not in the mask, the displacement of the closest point to it's right will be used.
- At measurement points 4, the relative displacement of those two points will be compared to DT n°10 ($hdef\_3$). The measurement from LEDs is obtained by interpolating vertically between the the relative horizontal displacement measured by LED n°44 and n°20 and the relative horizontal displacement measured with LED n°43 and n°31.
- For measurement points 5 and 1, their relative vertical displacement will be compared to DT n°12 ($vdef\_R2$).
- In the same way, the relative vertical displacement of points 6 and 5 will be used for comparison with DT n°13 ($vdef\_R3$).
- Similarly, the deformation between points 7 and 6 is compared to DT n°14 ($vdef\_R4$).
- On the compression side, the vertical displacement of point 8 will be compared to DT n°18 ($vdef\_L1$) and LED n°13.
- The vertical deformation between points 9 and 8 is compared to DT n°19 ($vdef\_L2$).

Some important points need to be kept in mind when analyzing the results. Regarding the comparison between DIC and DT, one should know that the displacement field from DIC is based on the deformations measured at the surface with the speckle pattern. The instrumentation is installed on the opposite face and on

the sides. The deformations measured at the two opposite faces is not necessarily identical. Furthermore, the DIC points are only approximately located in the same position as the DT. For example, deformations on the sides (measured by the DTs named $vdef\_L_i$ and $vdef\_R_i$) are compared to data points situated in the mask of the face. The mask is slightly cropped compared to the specimen such that an outer point of the mask is not exactly situated at the edge of the wall. In addition, the installed instrumentation can deviate from their intended position due to manual installation.

Regarding the comparison with the data from the LED system, the location of the targets due to handcraft is not a hundred percent accurate. Another uncertainty factor are the previously described interpolations between targets in order to obtain the displacement in another point. Therefore, differences in displacements/deformations between the three different systems are likely.

The results of the comparison are presented in Fig. 4.9.

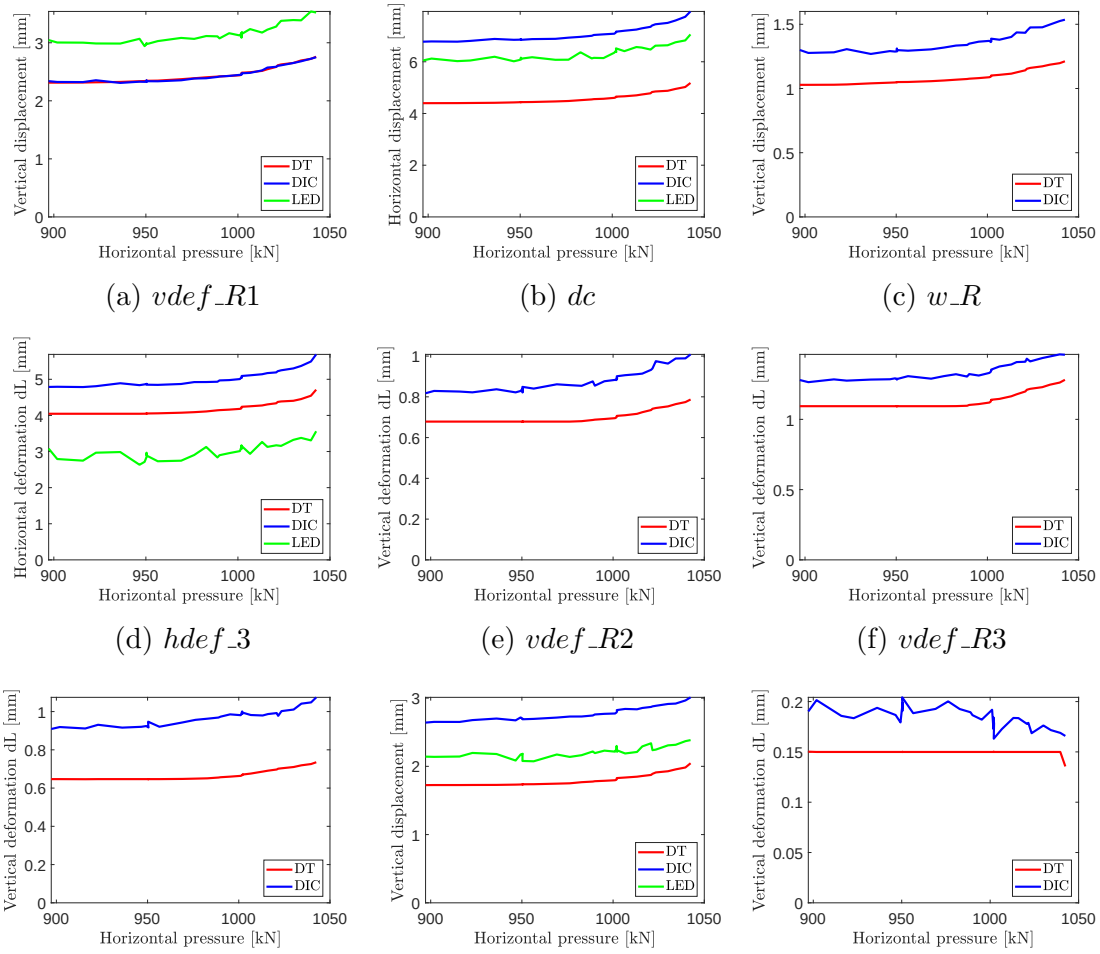

(a) $vdef\_R1$ (b) dc (c) w_R

(d) $hdef\_3$ (e) $vdef\_R2$ (f) $vdef\_R3$

(g) $vdef\_R4$ (h) $vdef\_L1$ (i) $vdef\_L2$

Figure 4.9: Comparison between DIC (subset = 51 px, step = 13 px), DT and LED at load step B9, before failure, in absolute values.

As can be seen in Fig. 4.9, the curves corresponding to different systems are similar in shape. However, they differ in terms of absolute value. The deformations or

Subset/ Step	$vdef\_R1$	dc	w_R	$hdef\_3$	$vdef\_R2$	$vdef\_R3$	$vdef\_R4$	$vdef\_L1$	$vdef\_L2$
51/13	-0,10	54,20	25,06	19,79	25,49	17,95	44,66	53,75	23,00
15/4	1,00	53,31	28,48	19,87	16,78	23,75	44,04	51,28	49,66
31/8	1,85	53,56	33,97	20,08	15,53	23,20	38,31	53,84	26,79

Table 4.1: Mean deviation in percent [%] between DIC and DT data for different subsets (and steps) [px].

displacements computed from DIC are mostly higher than measured by DT. Deformations computed with LED are in 3 out of 4 cases smaller than DIC measurements. The comparison between DIC and DT for different subset sizes is summarized in Tab. 4.1. It can be noted that different subset sizes do not lead to very different results. However, the DIC deformations and displacements are generally higher than recorded by the DT.

4.3 Comparison with kinematic model

One objective of the thesis is to validate the kinematic models. To do so, the deformation pattern from 3PKT is compared to the deformation computed with DIC at the instant right before failure (at peak).

4.3.1 Processing of DIC data

For the following sections, where the kinematics and shear mechanisms are analyzed for the whole wall, the displacement fields needed to be mapped. It has been chosen to redo the calibration with the advanced setting, using three views per camera and choosing the same marker when calibrating both cameras. That marker will become the (0,0) coordinate position, so the two cameras, even if analyzed separately, should have a correct mapping of the results. Since the same images were used, one should not expect a fundamental difference between the calibrations. The calibration parameters are

- 3 views per camera.
- Camera 1 : Scale factor = 1.46602 px/mm, thus a pixel size of 0.68212 mm; RMS of the fit = 0.364 px.
- Camera 2 : Scale factor = 1.4524 px/mm, thus a pixel size of 0.68852 mm; RMS of the fit = 0.239 px.

Compared to the original calibration, the RMS value improved, reflecting an even better calibration quality.

The DIC computation was done for the bottom frame and top frame separately. Both displacement fields were then merged and the complete displacement field is obtained.

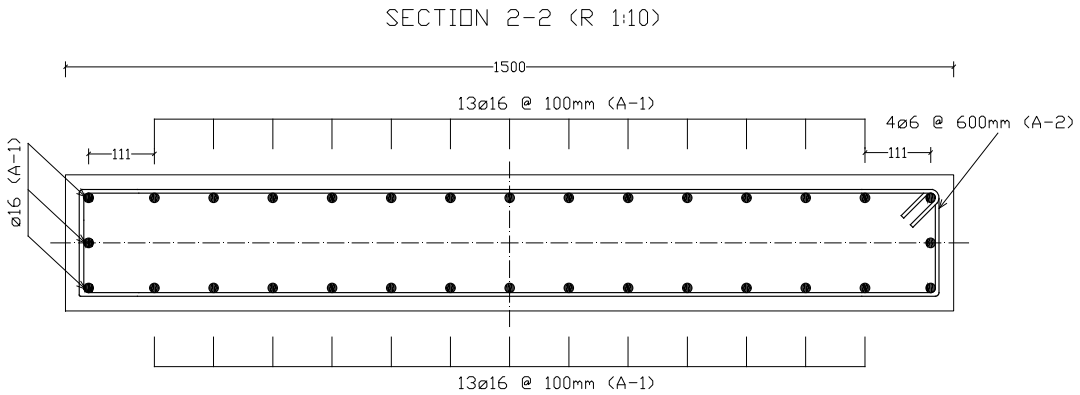

Figure 4.10: Longitudinal reinforcement of the wall.

4.3.2 Measured geometry and DOFs of kinematic model

The three-parameter kinematic model is based on 3 DOFs. These DOFs will be computed from experimental measurements (displacement transducers). The predicted deformation pattern is also a function of the angle of the critical crack. These 4 elements necessary for the computation of the deformation pattern will be presented in this section.

The critical crack angle is determined based on the crack pattern at failure. From pictures, it can be seen that the critical crack angle reaches the top corner of the wall (see Fig. 4.4) such that the crack can be idealized by a straight line, reaching from the bottom left corner to the top right corner. The angle of the critical crack α_1 is thus equal to the angle of the wall diagonal α with respect to the vertical axis. Therefore,

$$\alpha_1 = \alpha = \arctan\left(\frac{h}{a - 250}\right), \tag{4.1}$$

with

- h = depth of the wall = 1500mm
- a = wall height subjected to shear = 2300 (height) + 250 (distance from top edge to point of application of the horizontal actuator) = 2550 mm,

which yields $\alpha_1 = 33°$.

To compute the first DOF $\varepsilon_{t,avg}$, one has to know the effective depth of the section because the strain is evaluated at the effective depth of the wall d. The depth of the section is calculated by considering the longitudinal reinforcement (Fig. 4.10) in one half of the section and by calculating its centroid, which yields $d = 1088.4\ mm$. The DTs n°4 ($vdisp\_R$) and n°5 ($vdisp\_L$) measure the vertical displacement of the top block respectively on the tension side and compression. The vertical displacement at d is obtained by linear interpolation between those two measurements, since the block is considered to be rigid and does not deform. At peak, $vdisp\_R$ measured -10.98 mm (upwards) and $vdisp\_L$ measured 4.09 mm (downwards). By interpolation, the vertical displacement of the top block at a distance d from the left edge

(compression side) is -4.11 mm (upwards). The length over which the strains are averaged (l_t) corresponds to the height of the wall (2300 mm). The first DOF is thus

$$\varepsilon_{t,avg} = \frac{4.11}{2300} = 0.0018. \tag{4.2}$$

The second DOF is the horizontal displacement in the critical loading zone $\Delta_c = 5.391\ mm$ measured by DT n°9.

The third DOF Δ_{cx} representing the vertical displacement in the CLZ is not measured directly. If the concrete block above the critical crack is assumed to remain undeformed, as described in the 3PKT, the vertical displacement in the CLZ is supposed to be equal to the vertical displacement of the top block at the same location. The vertical displacement of the top block at the edge of the wall is obtained by interpolating between *vdisp_R* and *vdisp_L*. The downward displacement at the edge yields 2.16 mm.

With these DOFs, the deformation pattern is calculated according to Eqs. (3.1)-(3.4) presented in section 3.1.2.

4.3.3 Comparison of displacement fields

The displacement field computed with DIC will be compared to the deformation pattern predicted by the kinematic model. DIC measurements are valid in a grid of discrete data points, two neighboring points being separated by a distance equal to the step size. The grid of points will be transformed into a mesh of triangles suitable for further strain calculations. The mesh is also well adapted for visualizing deformations. However, the mesh can become very dense, especially for small step sizes. For applications related to kinematics, the mesh will be made coarser. For example, for a step size of 4 pixels, the "coarseness factor" is chosen to be 15 such that every 15th data point (horizontally and vertically) will be taken as a vertex of the triangular mesh. For a step of 13 pixels, the coarseness factor is 5. Generally speaking, it is convenient to construct the mesh such that the triangles have their diagonal edge parallel to expected cracks. In addition, the deformed shapes are generally amplified by an "amplification factor" (AF), usually taken as 15. In this way, the relatively small displacements become more visible.

The deformation pattern from DIC as a direct result of the analysis as well as the kinematic model determined with the 3 DOFs are represented in Fig. 4.11a and 4.11b, amplified by a factor 15.

The horizontal displacement components δ_z from DOF 1 to 3 for a point in the top left corner of the mask (coordinates x=11.95 mm, y=2072 mm) are listed below. One has to keep in mind that the mask used for DIC analysis is not reaching up to the top edge of the wall due to processing reasons.

- δ_z DOF1 = 7.82 mm.
- δ_z DOF2 = 5.39 mm.
- δ_z DOF3 = 4.21 mm.

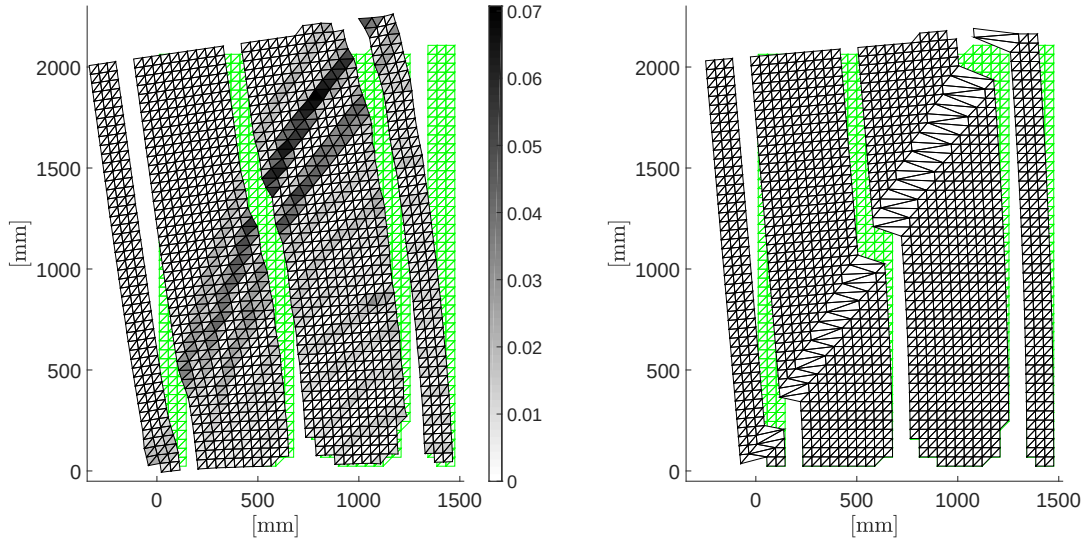

(a) Deformation pattern from DIC analysis with colorbar representing $|\varepsilon_1| + |\varepsilon_2|$ to illustrate damage, AF = 15.

(b) Deformation pattern from kinematic model (3PKT), AF = 15.

Figure 4.11: Deformation patterns at peak.

The total horizontal displacement of the top left point according to 3PKT is thus the sum of the contributions from each DOF, which gives 17.12 mm. For DIC, the horizontal displacement of the data point in the same position is 23.2 mm. The difference between DIC and 3PKT is quite high, namely 6.08 mm (26.2%). These horizontal displacements can also be compared to the displacement of the top block determined with LED, which was 21 mm at peak.

While the DIC cameras capture the absolute displacement field of the speckle pattern, the kinematic model only describes the deformation of the wall itself, disregarding any secondary movement. Therefore, in order to validate the kinematic model, every secondary movement that is obviously not taken into consideration by the kinematic model, should be removed from the output of DIC. The following movements and their respective values at peak were taken into account in the DIC analysis but not in the 3PKT:

- The slip of the foundation with respect to the floor, measured by *hdisp_F*: 0.2478 mm.
- The slip in the crack at the interface between the wall and the foundation, measured by *s_R*: 0.7712 mm.
- The pull-out of the reinforcing longitudinal bars on the tension side, estimated from strain gages values: 1.10 mm.
- The rotation of the foundation, measured indirectly by *vdisp_FL* and *vdisp_FR*, giving values at peak of respectively -1.513 mm (downwards, compression side) and 0.2066 mm (upwards, tension side).

These deformations are illustrated in Fig. 4.12. The pull-out of the longitudinal

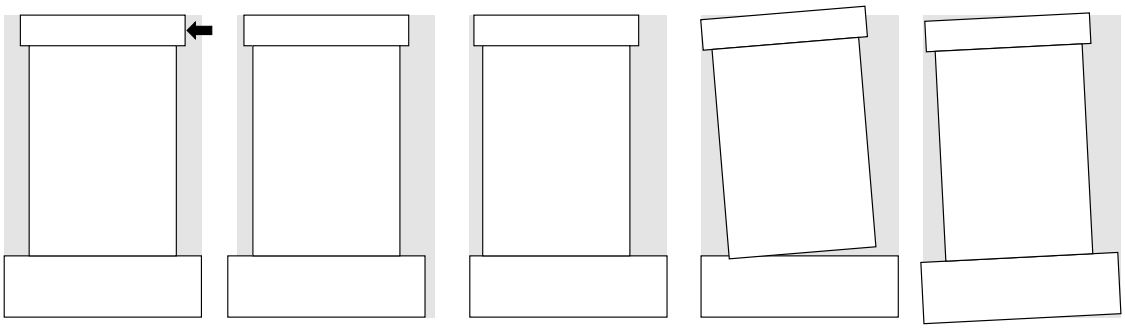

Figure 4.12: Secondary movements accounted for in DIC. From left to right: initial position, slip foundation-floor, slip at interface wall-foundation, pull-out, rotation of foundation.

reinforcement is related to strains in the footing. The shear wall is supposed to be rigidly fixed to the foundation. Under shear loading, the longitudinal reinforcement is highly stressed on the tension side at the basis of the wall. The strains do not become directly zero at the footing. The reinforcing bars still carry strains into the footing over a certain length. This phenomenon is called "strain penetration effect". The pull-out of the rebars results in a rotation of the wall about a certain point. The point of rotation can be considered as the point dividing the base into a compression and tension zone, which can be interpreted in terms of vertical strains ε_y. The compression zone would thus be the zone with negative values for ε_y. Another way to define the point in question is to look at the displacement field and define it as the point where the vertical displacement on either side is of different sign (e.g. points moving down to its left and up to its right). From Fig. 4.13, it can be seen that the pure compression zone represented as a black color ends at abscissa x = 230 mm. It was also observed that points close to the bottom edge move upwards to the right of this abscissa. The point of rotation of the wall due to pull-out will thus be defined at x=230 mm and y =0 mm. Consequently, the displacement field caused by the pull-out is calculated by small rotations. The angle of rotation is given by

$$\theta_{PO} = \frac{1.10}{(1500 - 39) - 230} = 8.94 \times 10^{-4}, \tag{4.3}$$

Similarly, the rotation of the bottom block, the foundation, causes a displacement field captured by DIC technology, but not by the kinematic model. The rotation of the bottom block should thus be deducted from the DIC result for proper validation. The angle of rotation is computed as

$$\theta_R = \frac{1.513 + 0.207}{1500 + 2 \cdot 570} = 6.51 \times 10^{-4}. \tag{4.4}$$

The x-coordinate of the point of rotation is 1752.9 mm and is therefore situated right of the wall. Consequently, every data point moves downwards due to the rotation of the foundation. The horizontal and vertical displacement for each data point based on a rigid body rotation about the point of rotation will then be deducted from DIC.

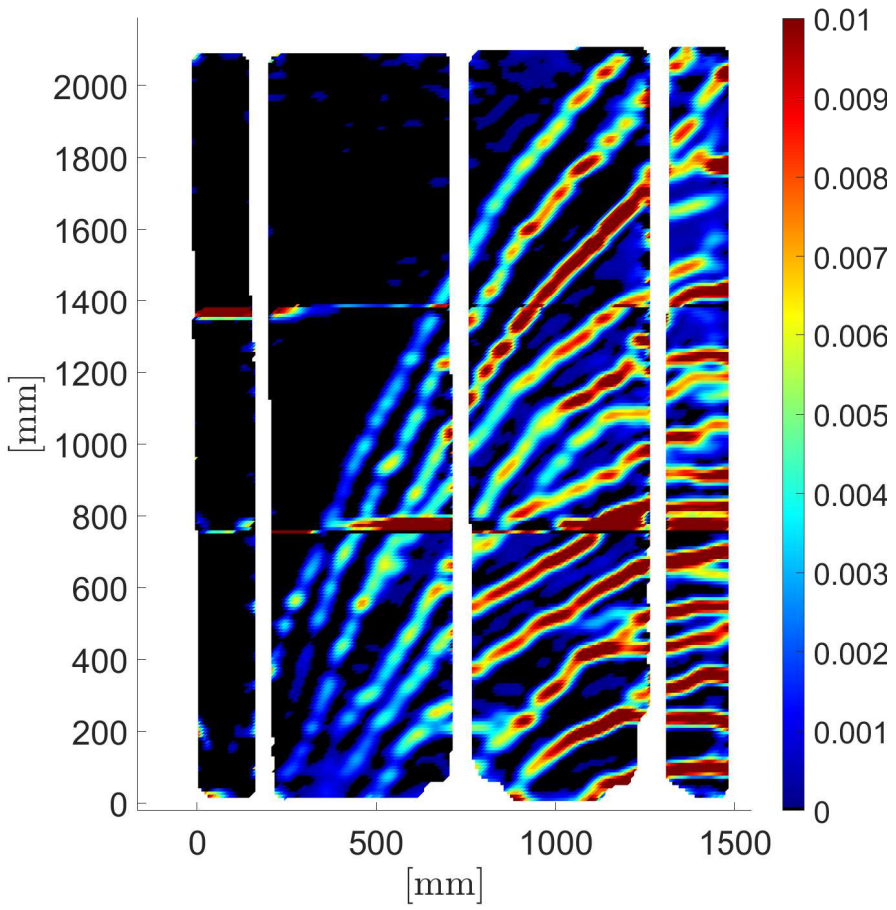

Figure 4.13: Vertical strains ε_y with a colorbar representing negative values (compression) in black.

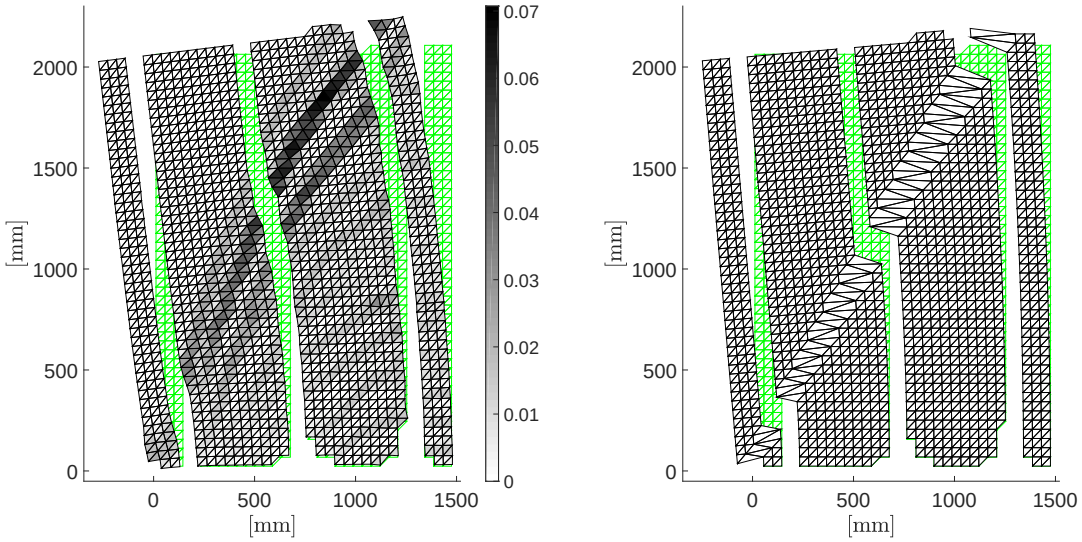

(a) Deformation pattern from DIC analysis with colorbar representing $|\varepsilon_1| + |\varepsilon_2|$ to illustrate damage, AF = 15, modified by removing the displacement due to pull-out, rotation and slip of the bottom block and the slip in the crack.

(b) Deformation pattern from kinematic model (3PKT), AF = 15.

Figure 4.14: Deformation patterns at peak.

A new comparison between the kinematic model and the modified DIC deformation pattern is shown in Fig. 4.14.

The horizontal displacement of a point in the top left corner of the mask will once again be compared to the displacement from 3PKT. In the following, the secondary displacements for the top left point are computed and removed:

- Data point of coordinates x = 11.95 mm and y = 2072 mm.
- The horizontal displacement of this point from DIC is 23.2 mm.
- The horizontal displacement due to pull-out is $8.94 \times 10^{-4} \cdot 2072 = 1.852\ mm$.
- The horizontal displacement due to rotation of foundation is $6.51 \times 10^{-4} \cdot 2072 = 1.350\ mm$.
- By deducting also the slip in the crack and the slip of the foundation, the corrected horizontal displacement becomes $23.2 - 1.35 - 1.85 - 0.248 - 0.771 = 19.02\ mm$.

The difference between the corrected value from DIC and the kinematic model is 19.02-17.12 = 1.90 mm (10%). The top horizontal displacement determined with the 3 measured degrees of freedom is thus very close to the actual displacement. In addition, it is important to visualize the shape of the missing deformation. To do so, the displacement field computed with 3PKT will be subtracted from the displacement field from DIC. Fig. 4.15 shows the difference in displacement field, both for the unmodified DIC and for the modified DIC deformation pattern.

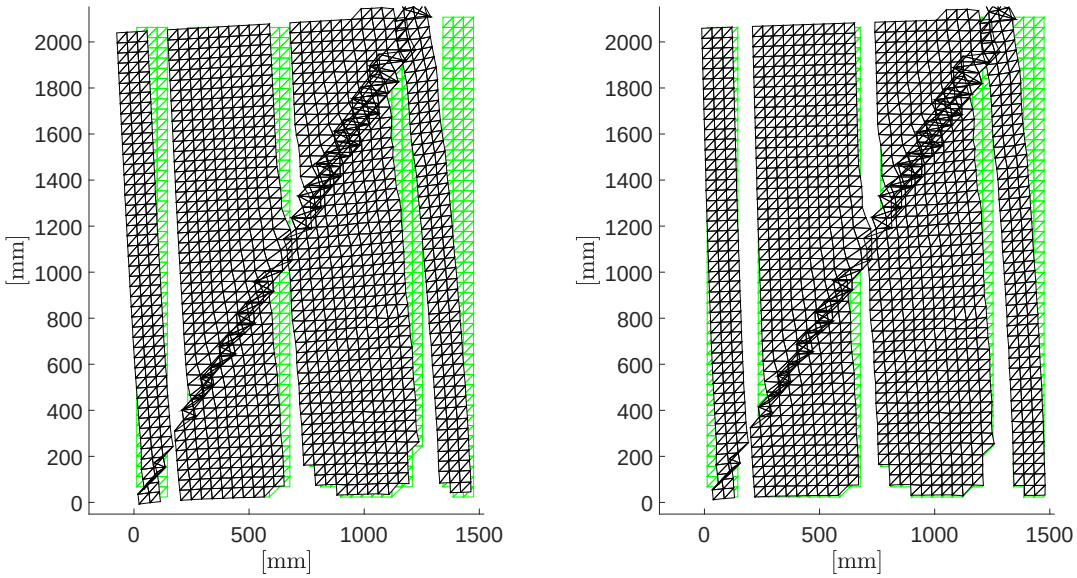

(a) Difference in displacement fields between DIC and kinematic model, unmodified DIC, AF = 15.

(b) Difference in displacement fields between DIC and kinematic model, modified DIC, AF = 15.

Figure 4.15: Comparison of displacement fields at peak (deformed positions of DIC subtracted by deformed positions of kinematic model).

Comparing Fig. 4.15a with Fig. 4.15b shows that removing well known components from DIC improves the estimation of the kinematic model. The interest of the kinematic model remains in its simplicity. Therefore, the main interest in this chapter is to check missing degrees of freedom, which were not yet accounted for.

It can be observed that the right edge of the wall curves more than predicted by the 3PKT. The missing deformation in the bottom concrete body is also visible when comparing the edges of the mask in the middle (discontinuity due to steel bar). One reason might be the assumption of rigid struts between the cracks. In fact, the zone below the critical crack is represented by a series of rigid radial struts pinned at the bottom left edge and connected to the tension reinforcement. The rotation of each strut about the pinning point is proportional to the elongation of the reinforcement such that the displacements in the fan depend only on the first DOF $\varepsilon_{t,avg}$. If the struts were not assumed to be rigid, they could deform and become shorter and the deformation of the block below the crack predicted by 3PKT would be higher.
The concrete block above the critical crack remains globally undeformed, which confirms the hypothesis of 3PKT. But close to the critical crack, another crack formed such that the assumption of one uncracked concrete block above the critical crack is not completely verified. As a consequence, the slip in the crack is not only concentrated in one single crack.
Another factor is the shape of the critical crack. While in the kinematic model, the critical crack is modeled with a straight line, the real crack is more curved. This choice might lead to higher lateral displacement in the lower part of the top concrete block than actually observed in reality.

4.3.4 Comparison of crack displacements

The 3PK model provides formulas for crack width and slip halfway along the crack. They will be compared to the crack width and slip computed based on DIC.

Regarding the crack opening, the kinematic model suggests to check if the crack width will be distributed among n_{cr} several major cracks. According to the model, this must be taken into account if the longitudinal web reinforcement $\rho_{l,web} \geq 0.2\%$. In the present case, referring to Fig. 4.10, the longitudinal web reinforcement ratio is similar to the total reinforcement ratio since the reinforcement is almost uniformly distributed.

Since $\rho_{l,web} = 1.86\%$ is much bigger than 0.2%, n_{cr} will be taken bigger than 1 and can be estimated by the number of cracks within the transition zone between the fan and the rigid block:

$$n_{cr} = \frac{l_k}{s_{cr}} \tag{4.5}$$

with l_k being the length of the transition zone and s_{cr} being the crack spacing in the effective tension zone. The latter one is computed with

$$s_{cr} = 0.28\,\frac{d_b}{\rho_{l1}}, \tag{4.6}$$

where ρ_{l1} is the reinforcement ratio in the effective tension zone. Since the longitudinal reinforcement is uniformly distributed, $\rho_{l1} = \rho_l = 1.86\%$. With a bar diameter d_b of 16 mm for the main flexural reinforcement, the crack spacing is equal to $s_{cr} = 240\ mm$. Since the critical crack reaches up to the top corner, $l_k = l_0$ where

$$l_0 = s_{cr} \geq \min\left(1.5(h-d), d - h/2\right) \cdot \cot\alpha_1 = 519\ mm. \tag{4.7}$$

The crack width should thus be distributed among $n_{cr} = 519/240 = 2.16$ cracks. $\varepsilon_{t,min}$ is assumed to be $\sim 0.5\varepsilon_{t,avg}$. With the previously determined parameters, the crack width is $w = 3.09\ mm$. By ignoring the term Δ_{ci0} in the formula for slip, the slip halfway along the crack is $\Delta_{ci} = 5.45\ mm$.

The term Δ_{ci0} can be estimated from DIC. In fact, it corresponds to the shortening of the bottom half of the top strut from the fan. The shortening can be estimated by having a look at the displacements of a point halfway along the critical crack in the strut that formed just below it. In the present case, a point with coordinates x = 686 mm and y = 1141 mm is suitable. Its horizontal displacement is -11.48 mm and vertical displacement is 2.384 mm. The displacement parallel to the crack of crack angle $\alpha_1 \sim 33°$ is determined with trigonometry, which yields 4.26 mm. Taking Δ_{ci0} as 4.26 mm, the theoretical slip of the kinematic model reduces to 1.174 mm.

A detailed description of the crack displacements along the entire crack based on DIC is given in section 4.4.1. The crack width and slip based on DIC measurement halfway along the crack are 1.97 mm and 1.39 mm.

In conclusion, the crack width determined by 3PKT is about 56.9% higher than the one measured thanks to DIC. The slip from 3PKT is only 15.54% smaller than the slip based on DIC.

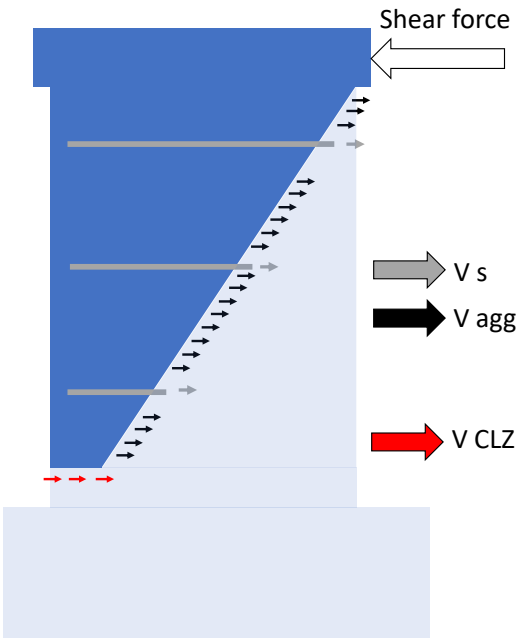

Figure 4.16: Free-body diagram of a wall with applied horizontal shear force and horizontal components of internal stresses.

4.4 Mechanisms of shear resistance

In this section, the shear-resisting mechanism presented in chapter 3 will be computed. First, the aggregate interlock will be evaluated. Then, the shear resisted in the critical loading zone is evaluated. Finally, the contribution of the shear reinforcement is determined. In the last section, the total shear resistance will be evaluated and compared to the maximum applied shear force.

These three contributions are pointed out in Fig. 4.16.

4.4.1 Aggregate interlock

The interlock stresses are calculated thanks to three different models based on crack displacements. These crack kinematics, namely crack width and slip, should be evaluated along the critical diagonal crack.

Measured crack kinematics

The crack kinematics from DIC will be presented in this section. By dividing the height of the wall into approximately 100 mm segments and selecting manually the end points of each segment as well as the point in the crack and the 4 points to evaluate the movement of each face of the crack, we can compute the crack width and slip. In practice, those points are situated as presented in Fig. 4.17, in agreement with the crack kinematics methodology presented in Appendix A.

The computed crack width and slip are represented in Fig. 4.18 by polygons. Larger polygons indicate higher slip in the crack or larger crack opening.

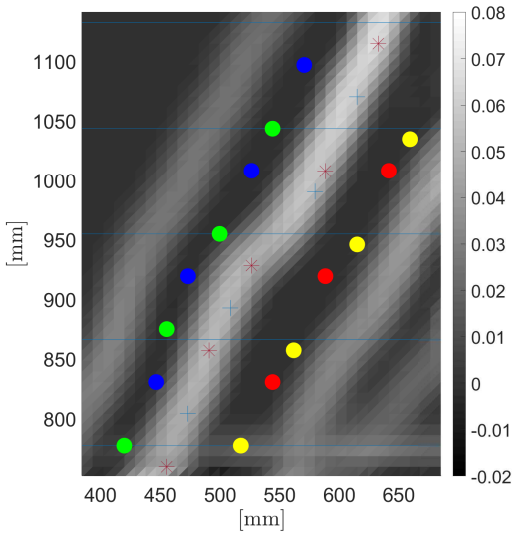

Figure 4.17: Zoom on crack (plot of maximum principal strain). $*$ = end points of crack, $+$ = crack point, bullets in blue, green, red, yellow = P1 to P4.

Interlock stresses and shear contribution

In chapter 3, three crack models were presented, each of them computing interlock stresses based on crack width and slip. Thus, for each crack segment visible in Fig. 4.18, a normal and shear stress is determined. The total shear trasferred through the crack is then calculated by integrating the horizontal components of the stress normal to the crack and tangent to the crack with Eq. (3.34). In the present case, the integral consists of the sum of the shear contribution from each segment. In fact, the interlock stresses for a given crack segment are considered constant along the segment. As a consequence, the stresses and thus the shear force vary stepwise along the crack.

These following shear forces are obtained with the crack models for crack width and slip represented in Fig. 4.18:

- Two-phase model (TPM): 122.80 kN.
- Contact Density Model (CDM): 47.406 kN.
- Pure Mechanics Crack Model (PMCM): 208.75 kN.

As an example, the evolution of the contribution of shear stress and normal stress from PMCM is shown in Fig. 4.19. Those contributions correspond to the segments represented in Fig. 4.18, from bottom to top. Generally speaking, shear stresses are higher than normal stresses. However, the steep angle of the crack plays an important role since shear and normal stresses must be projected horizontally in order to check for horizontal equilibrium. The total shear force for PMCM is obtained by integrating the dashed curve over the total crack length. As an example, the first segment, at the bottom of the crack, is characterized by a very small crack width (0.34 mm) and slip (0.53 mm). Combined with a crack angle (angle of the crack with respect to the vertical axis) of only 21.7 °, the interlock contributes

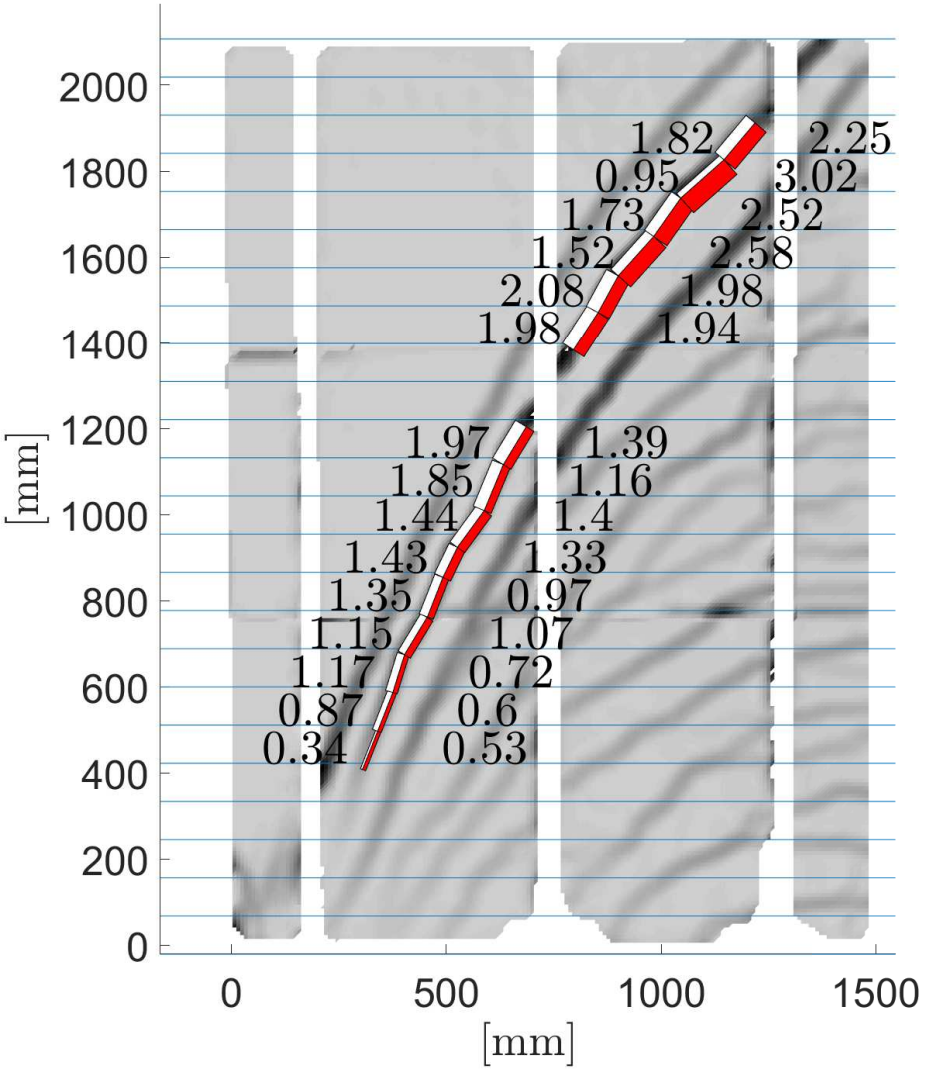

Figure 4.18: Crack width (white) and slip (red) [mm].

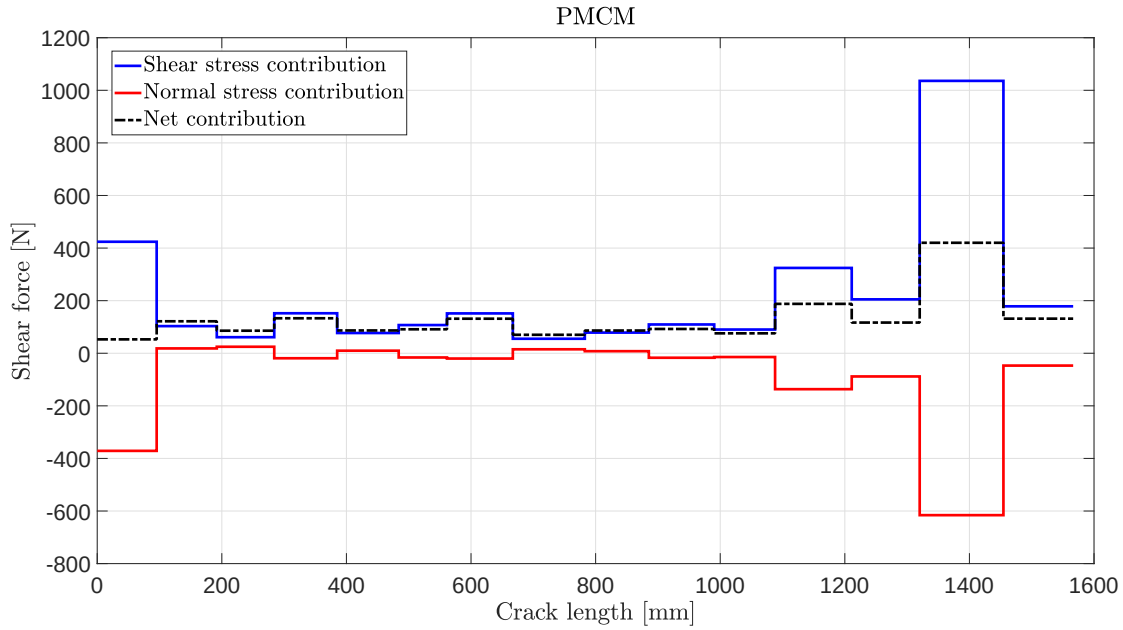

Figure 4.19: Stress contributions to total shear force transferred in the crack for PMCM model.

only little to V_{agg} for PMCM. For TPM and CDM, it provides even an unfavorable contribution (reduction).

Since the displacement field is not computed over the whole specimen because of experimental construction conditions, the interlock stresses between segment 9 and 10 in the middle of the specimen as well as the contribution of the top right crack part should be estimated.
For the middle part, it has been decided to compute the crack angle and crack segment length from the end points of the adjacent segments, here defined by points with coordinates (686;1204) and (796;1383). The shear stress and normal stress is taken as the average of the stresses of the adjacent segments. Projecting those stresses horizontally and integration over the crack surface, the additional contribution is estimated. The crack part in the middle is estimated to increase the previously determined value by 8.78% (based on PMCM model).
Similarly, interlock stresses of the missing top part are considered to be equal to the stresses developing in the adjacent segment below. The crack angle and length of the segment are computed with end points (1217;1912) and (1380;2107). The calculation yields that the contribution to V_{agg} is consequently increasing by 15.94%. By taking into account those two contributions, V_{agg} yields 260.4 kN according to PMCM.

4.4.2 Critical loading zone

The shear transferred in the critical loading zone is evaluated by integration the shear stresses over a horizontal plane, as illustrated in Fig. 4.16. The location of the horizontal plane should be discussed. In fact, the ideal situation would be to cut horizontally when the critical diagonal crack becomes more dispersed and little

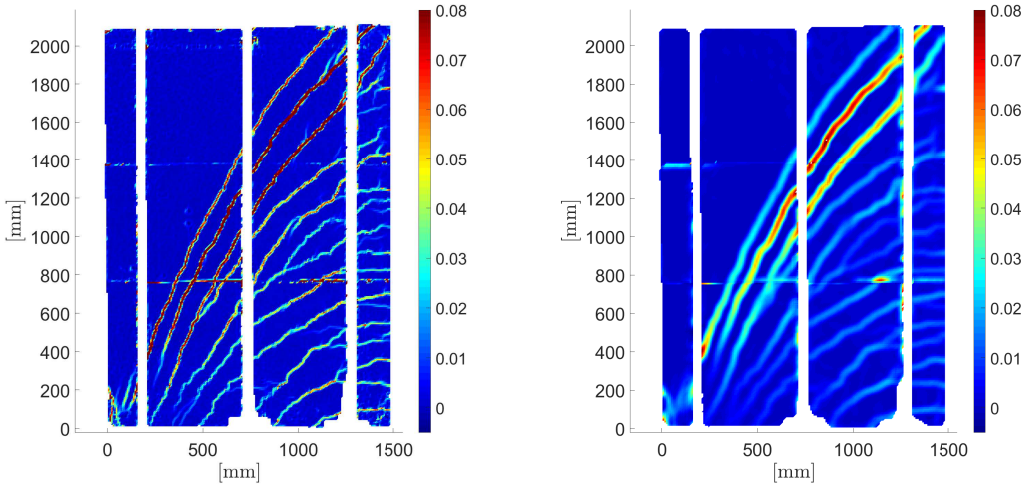

(a) Maximum principal strain ε_1 for a subset of 15 px (factor 3).

(b) Maximum principal strain ε_1 for subset of 51 px.

Figure 4.20: Maximum principal strains.

cracks are present. However, from experimental data, defining the region with little cracks is not straightforward as will be explained in the following sections.

Strains

Strain fields are determined with the constant strain triangle method described in chapter 3.

In this application, for a subset of 51 pixels and a step of 13 pixels, no factor is applied to the mesh. However, for a subset of 15 pixels and a step of 4 pixels, a coarseness factor of 3 is applied such that a right-angled mesh triangle has its two perpendicular legs of length $3 \times 4 = 12$ *pixels*. As a consequence, the density of the mesh is similar to the one obtained with a step of 13 pixels. Furthermore, the computation time is limited (order of magnitude: 10 seconds, for 113400 elements).

Strain calculations for a small subset (e.g. 15 px) give a maximum principal strain field, which allows for easy tracking of the cracks, as can be seen in Fig. 4.20a. Higher subset lead to smoother strain fields as can be seen in Fig. 4.20b. Fig. 4.20a and 4.20b show that the strain field is a bit discontinuous and disturbed along a horizontal line at height 760 and 1370. These are the limits of the overlapping area, in which the vector field from the bottom frame and from the top frame are interpolated and merged. These are the locations where the masks ends. Close to the ends of the mask, irregularities are more common, which enhances the probability of discontinuities in the merged vector field. This is also the case close to the steel bars where the mask had to be disconnected.

The critical loading zone is situated at the bottom left corner, where the maximum principal strains are disturbed and do not reveal clear cracks as can be seen in Fig. 4.21a. It should be noted that the critical diagonal crack is the one emerging from the top right corner of Fig. 4.21a. As already mentioned earlier, an addi-

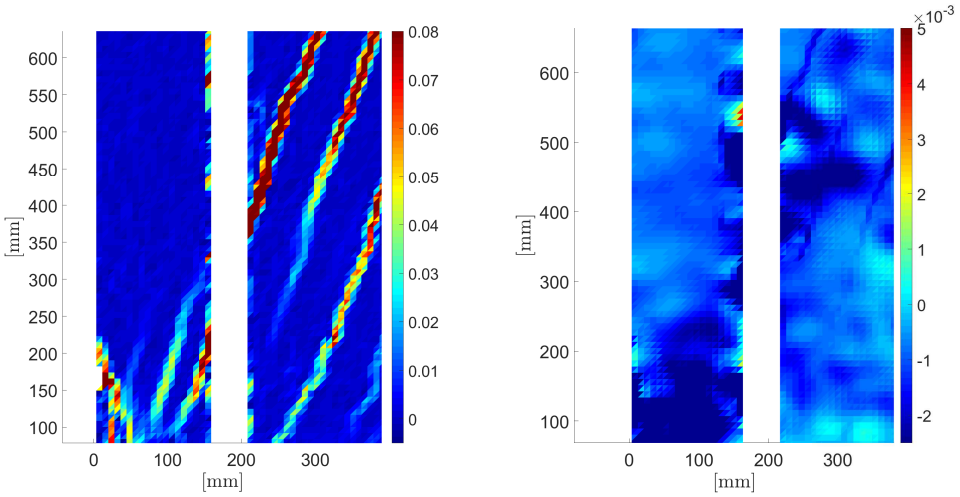

(a) Close-up of area close to CLZ (ε_1). (b) Close-up of area close to CLZ (ε_2).

Figure 4.21: Principal strains in disturbed area (CLZ) at the bottom left of the wall.

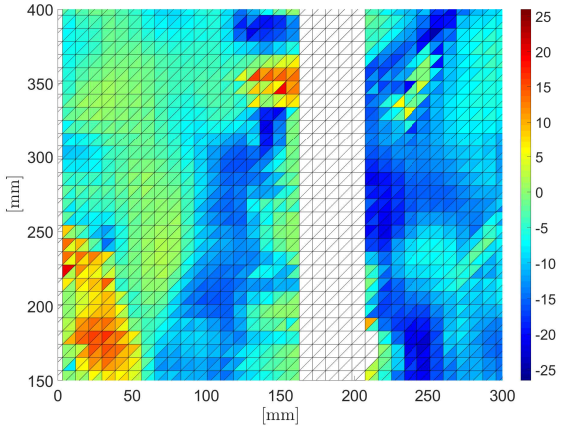

Figure 4.22: Shear stresses τ_{xy} for V_{CLZ}, based on the biaxial failure criterion.

tional crack left to it becomes visible and wide especially in the zone close to the bottom. The exact plane where the critical crack gets dispersed can not be identified straightaway from Fig. 4.21a. Another indicator might be minimum principal strains. High principal compressive strains are observed in the zone as shown in Fig. 4.21b, where the lower limit of ε_2 is set to the crushing strain of approximately 2.5×10^{-3}. Crushing strains are present up to a level of y = 150 mm. Considering both Fig. 4.21a and 4.21b, the horizontal plane is assumed to be somewhere in the area defined by $x \in [0, 300]$ and $y \in [150, 400]$. The criterion for the horizontal cut of the FBD is the maximization of V_{CLZ}. Therefore, the shear resistance is computed for different planes in the previously defined area and the value of V_{CLZ} is chosen to be the maximum value.

Stresses and shear contribution

The shear stresses in the previously defined zone are shown in Fig. 4.22. The planes are defined in a row of triangles. Therefore, the value of τ_{xy} along the x-axis (horizontal axis) for a given plane is chosen to be the average value of τ_{xy} from the

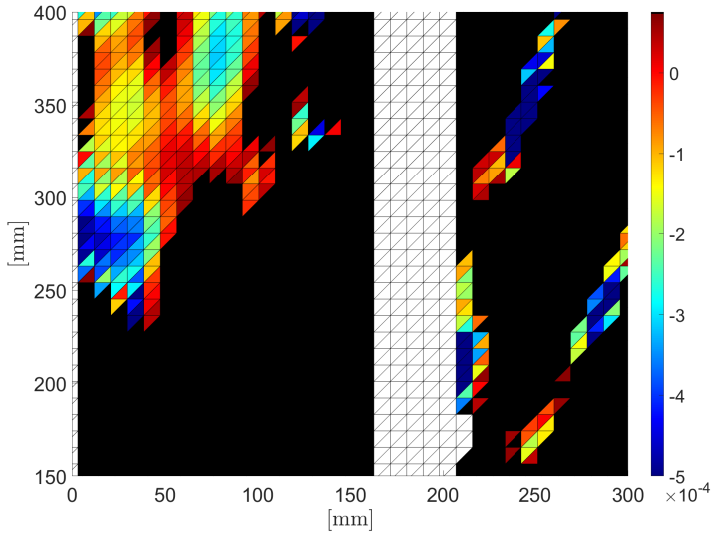

Figure 4.23: Maximum principal strains ε_1 in zone, with $\varepsilon_1 \geq \varepsilon_{cr}$ being colored in black.

upper and lower triangle. V_{CLZ} is obtained by integrating τ_{xy} over the plane.

Since most of the maximum principal strains are higher than ε_{cr} (see black triangles in Fig. 4.23), the three different constitutive laws presented in chapter 3, namely "biaxial failure criterion", "uniaxial compression" and "compression-softening" give different values for σ_2 and therefore for τ_{xy} and V_{CLZ}.

The shear force transferred in different planes is shown in Fig. 4.24 for the 3 different models, in function of the height of the row. It can be seen that they do not differ very much in shape but in value. While the compression-softening effect gives generally lower shear forces due to reduced compressive strength, uniaxial compression gives the highest shear force because no biaxial effect is considered and higher compressive stresses are accepted. The biaxial failure criterion produces intermediate values.

For the preferred constitutive law, including compression-softening, the maximum shear is transferred at the plane at height 303 mm with a maximum value of 539 kN. The evolution of stresses along the horizontal axis for this row is represented at Fig. 4.25. Maximum principal stresses σ_1 are mostly 0 since the maximum strain is often larger than ε_{cr}. Principal compressive strain directions in the analyzed zone are shown in Fig. 4.26. They are mostly close to vertical, slightly inclined.

As can be seen in Fig. 4.25, shear stresses are zero close to and behind the metal bar which causes a discontinuity in the stress fields. To estimate a more correct value of the shear force resisted in the critical loading zone, an interpolation will be done between abscissa 140.5 with shear stress τ_{xy} = -14.7 MPa and 211.5 with τ_{xy} = -16.3 MPa to account for shear stresses in the discontinuous zone. Integrating the mean value over the plane, the additional shear force to be considered would be:

$$V_{CLZ,add} = \frac{(-14.7) + (-16.3)}{2} \cdot 230 \cdot (211.5 - 140.5) = -253\,kN, \qquad (4.8)$$

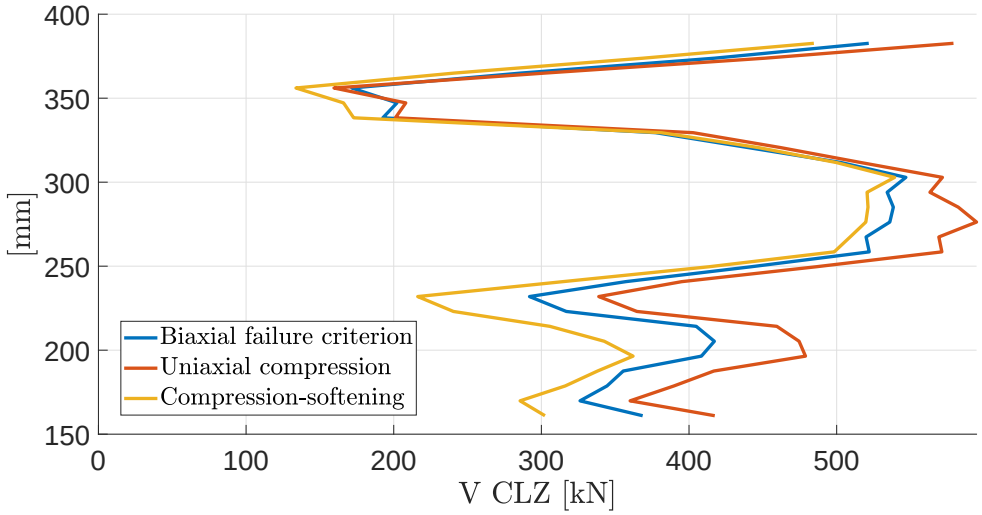

Figure 4.24: Evolution of V_{CLZ} along the y-axis according to the 3 proposed models.

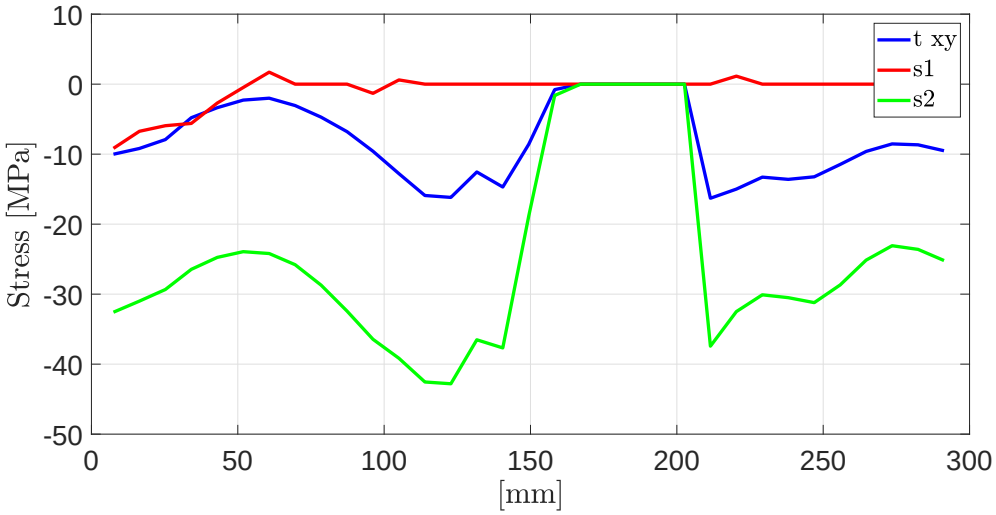

Figure 4.25: Principal stresses ($\sigma_1 = s1$ and $\sigma_2 = s2$) and horizontal shear stress $\tau_{xy} = txy$ at plane of maximum V_{CLZ} according to compression-softening model.

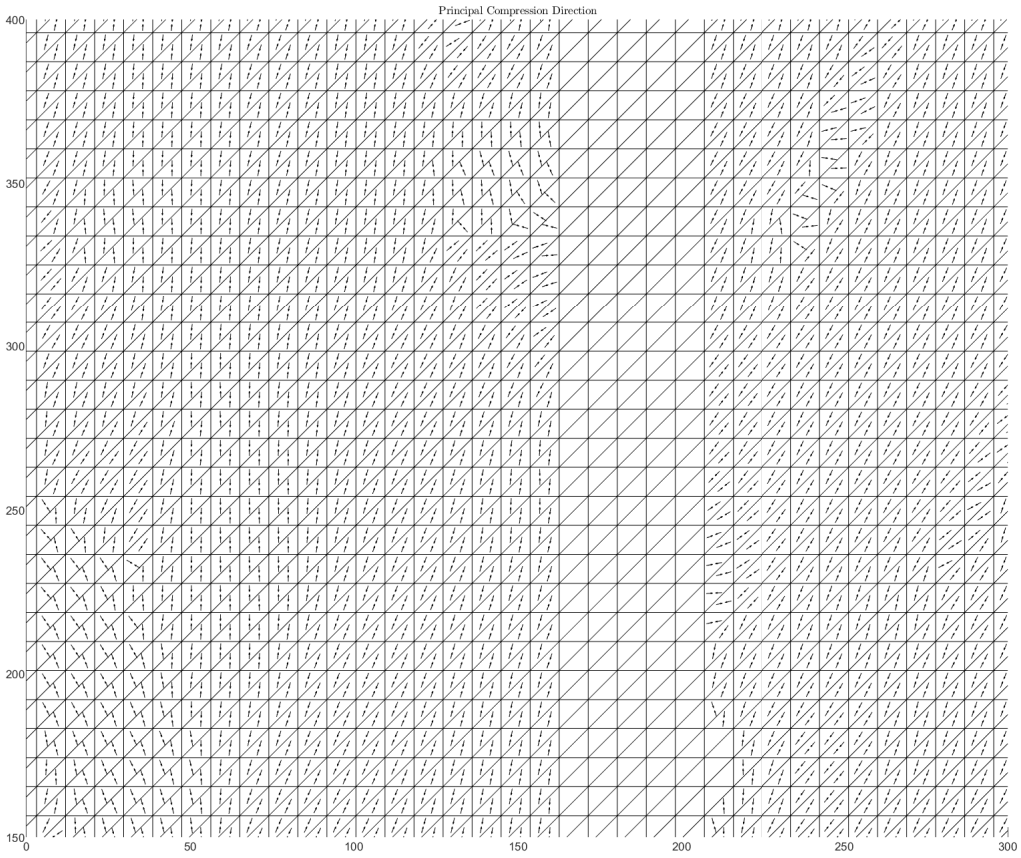

Figure 4.26: Principal compressive strain/stress directions in CLZ.

which results in a total shear force transferred in the CLZ (in absolute values) of $539 + 253 = 792\ kN$. One should also note that the critical loading zone is thus defined by a plane at height 303 mm reaching from the left edge of the wall to abscissa 291.3 mm. This should be considered in the overall body equilibrium.

4.4.3 Stirrups

The contribution from tensile stresses in the stirrups to the resisting shear force is calculated in this section.

As shown in Fig. 2.2, 4 layers of stirrups are placed. According to the plan, stirrups of diameter 6 mm should be placed, but diameter 8 mm were delivered and placed. Assuming a yield stress of 540 MPa in each stirrup, the shear transferred by the stirrups is estimated to be 217.2 kN. If we take into account the fact, that the lowest level of stirrups is not intersected by the free-body diagram, the shear resistance provided by the stirrups drops to 163 kN.

4.4.4 Total shear force

To evaluate the total shear force, the now defined free-body diagram should be examined. The horizontal cut for V_{CLZ} was decided to be at height y = 303 mm. However, the aggregate interlock is only evaluated down to height y = 408 mm. Therefore, the interlock along approximately 100 mm is missing, but it was observed that the lowest crack segment considered in the calculation barely contributed. Therefore, the missing segment is assumed to be negligible.

By adding the previously defined load-bearing mechanisms, with PMCM model for aggregate interlock, we obtain a total transferred shear force of

$$V_{tot} = V_{CLZ} + V_{agg} + V_s = 792 + 260 + 163 = 1215\ kN, \tag{4.9}$$

, which is larger than the applied shear force at peak of 1042 kN. The computed shear resistance is 173 kN higher, which corresponds to 16.6%.

The same calculation is done for the other two aggregate interlock models:

- TPM: $V_{agg} = 122.8\ kN$. With an increase of 8.78% and 15.94% for the missing crack segments, V_{agg} yields 155 kN. The total shear force yields $V_{tot} = 1110\ kN$, which is 68 kN larger than the applied force (6.53%).
- CDM: $V_{agg} = 47.4\ kN$. With an increase of 8.78% and 15.94% for the missing crack segments, V_{agg} yields 59.1 kN. The total shear force yields $V_{tot} = 1014\ kN$, which is 28 kN smaller than the applied force (-2.69%).

In conclusion, the sum of the contributions from aggregate interlock, critical loading zone and stirrups give a shear resistance of the same order of magnitude as the applied force. The Contact Density Model produces the smallest aggregate interlock, but the total resisted shear force is the closest to the applied load.

The critical loading zone is shown to be the dominant mechanism in this application, accounting for 76% of the applied force. The contribution from stirrups is estimated to be about 16%. The missing 8% come thus from aggregate interlock.

Chapter 5

Results: Coupling Beam

In this chapter, the behavior of the coupling beam during the test will be described. The DIC measurements will be analyzed and validated by comparing them with measurements from displacement transducers (potentiometers). Then, deformations will be analyzed and compared to the deformation pattern predicted by the 2PK kinematic model. In the last section, the shear-resisting mechanisms will be evaluated and compared to the applied shear force at peak.

5.1 Global observed behavior

The load-displacement response is obtained with measurements from potentiometers. The horizontal load corresponds to the sum of the applied force of the two horizontal actuators. The horizontal displacement is defined as the displacement of the top block and will be taken as the average of the measurements from the displacement transducers installed at either side of the top block. They measure the displacement with respect to the bottom block. Therefore, one should keep in mind that in case of a slip of the bottom block with respect to the floor, the absolute horizontal displacement is actually higher than the one measured by DT. Fig. 5.1 shows the load-displacement curve for the short coupling beam.

The pre-peak behavior can be described as follows. As the load increases, cracks initiate in the end sections, soon followed by inclined cracks that propagate from the side edges towards the compression zones in the end sections. The latter are referred to as flexure-shear cracks and develop due to tension along most of the shear span caused by the double curvature. At a load slightly higher than 300 kN, a major diagonal crack forms. The crack extends from the top right corner to the bottom left corner. This crack causes a sudden displacement of the concrete above the formed crack and the applied force is suddenly decreased. At that point, a load stop takes place to allow crack measurements by hand. Cracking leads to a gradual decrease in stiffness represented by a diminishing slope of the load-displacement curve.

The maximum horizontal load applied to the beam is 456 kN. The horizontal displacement of the top block reaches 6.63 mm at peak. Since the experiment is displacement-controlled, the post-peak behavior is well described. In fact, the actuators apply the exact amount of force to produce a certain increment of displacement. The curve decreases after the peak, reflecting a gradual decrease in resistance of the beam. The failure is defined at the point when the applied force

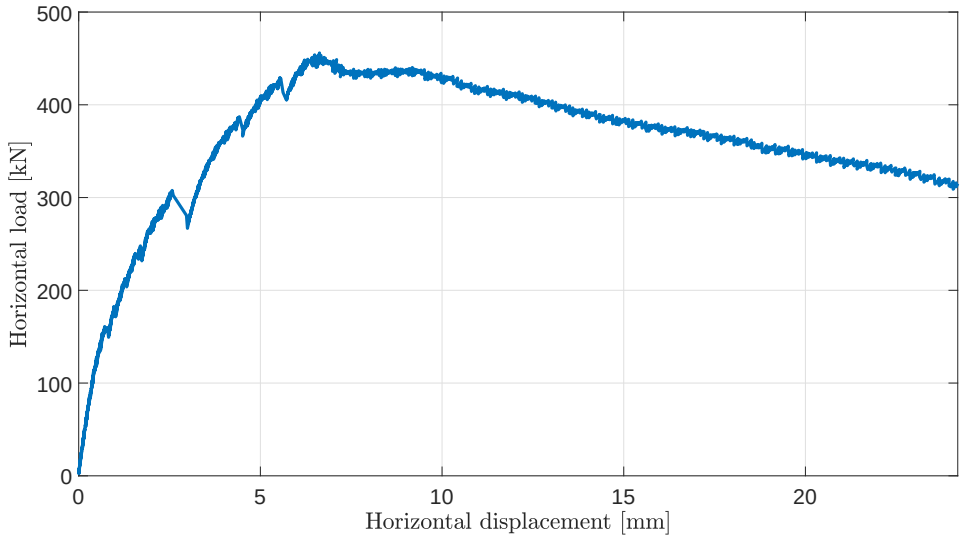

Figure 5.1: Load-displacement response of the short coupling beam.

can not be increased further. A photograph of the specimen close to peak is shown in Fig. 5.2. The failure is described as diagonal tension failure along the major diagonal crack. After failure, the major crack continues opening gradually and the shear mechanisms become less effective. During the post-peak, it is also observed that concrete in the compression zones is highly stressed, leading to gradual damage and disintegration. Towards the end of the test, several other inclined cracks start to widen significantly and in the bottom compression zone, big pieces of concrete are likely to spall due to high compressive stresses, as can be seen in Fig. 5.3.

The vertical displacement of the top block during the test can be seen in Fig. 5.4. With increasing horizontal force, the beam elongates vertically. At 45% of the test duration, the peak force is reached. Simultaneously, the vertical displacement is maximum. This is explained by the fact that afterwards, the load decreases gradually and the tensile reinforcement is less stressed. As a consequence, the longitudinal reinforcement and the beam shorten. The vertical actuators do not influence the vertical deformation. In fact, they prevent the top block from rotating, but allow for free elongation. Therefore, they are regulated such that the displacement of both actuators is identical. The force in the actuator on the side of the horizontal actuators remains constant at about -21.3 kN (push), while the pulling force applied by the second vertical actuator increases gradually from the initial force of 21.3 kN to approximately 55 kN (pull) at peak. Afterwards, the force remains nearly constant. The pull exerted by the second actuator is thus the driving force that prevents the top block from rotating.

5.2 Validation of DIC measurements

In this section, the DIC measurements will be analyzed and the load sequence will be traced back. The data will also be compared to measurements from displacement transducers (DT).

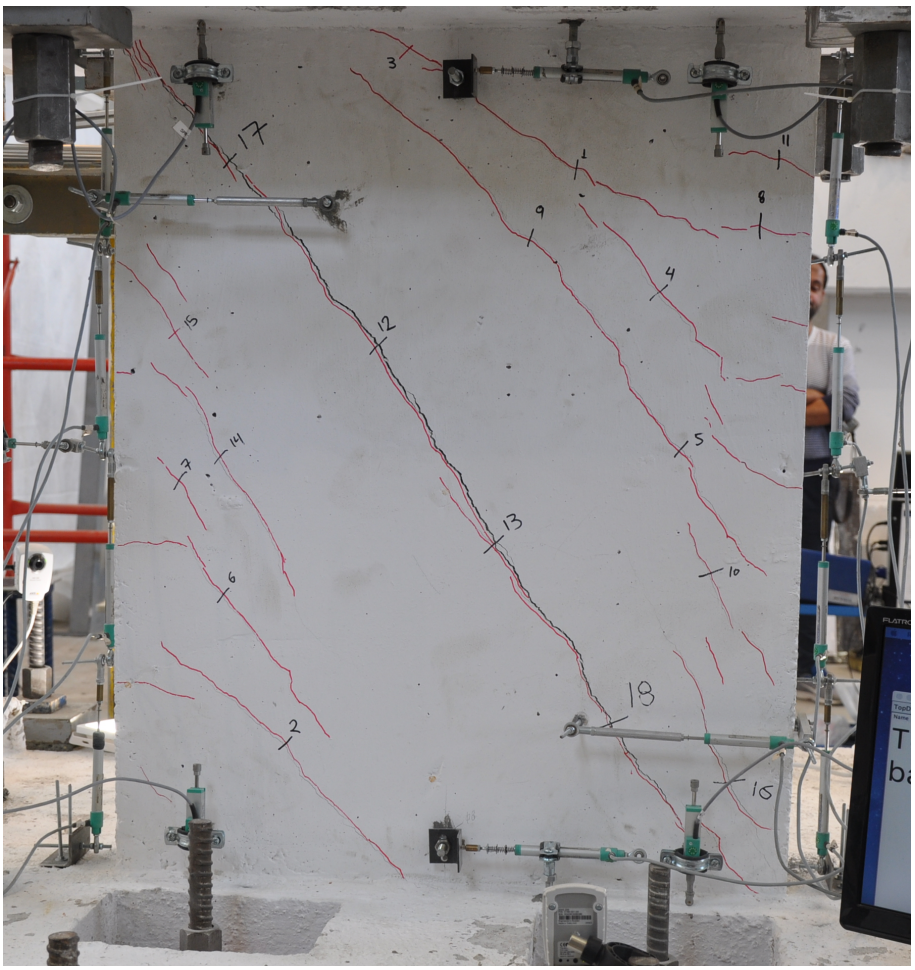

Figure 5.2: Test specimen (opposite side of DIC frame) at a horizontal load of 452 kN and a horizontal displacement of 6.74 mm.

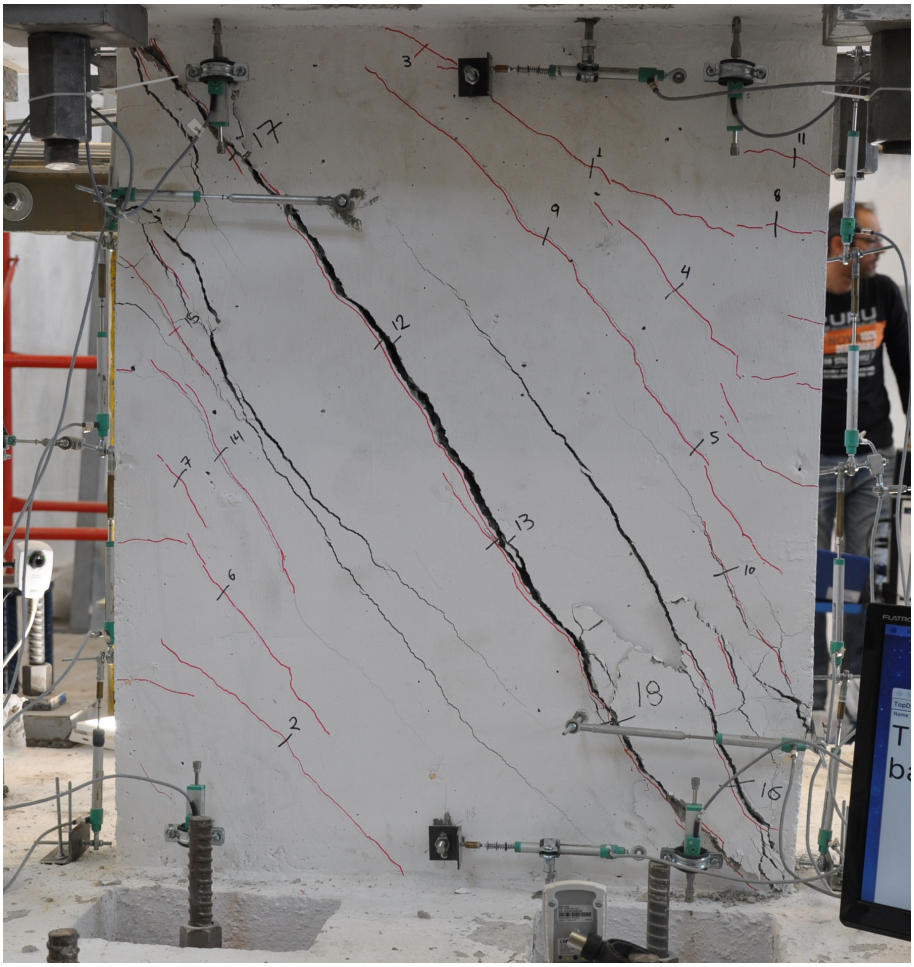

Figure 5.3: Last photograph of the time-lapse (end of test) at a horizontal load of 312 kN and a horizontal displacement of 24.1 mm.

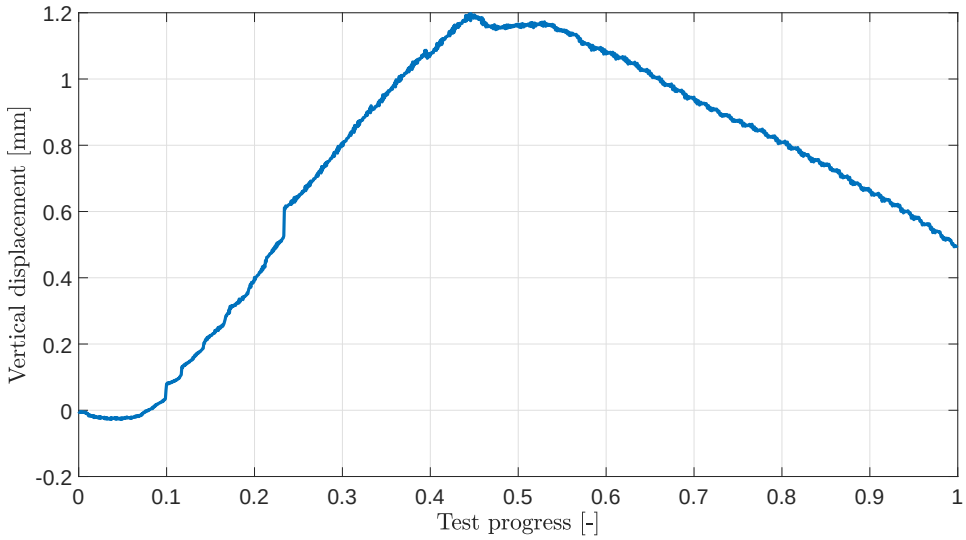

Figure 5.4: Mean vertical displacement of top block.

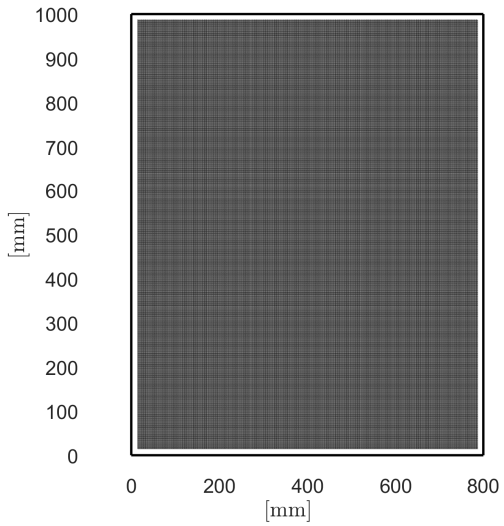

Figure 5.5: Region of interest within the dimensions of the specimen (black lines).

5.2.1 Processing of DIC data

The output of the DIC processing performed by the University of Patras is a displacement field at 1312 instants. Since pictures were taken every 5 seconds during the test, the steps give the displacement field for every fifth second. The region of interest in represented in Fig. 5.5. The mask defining the region where DIC will be analyzed has a size of 771.49×971.58 mm and therefore does not cover the whole beam (of size 1000×800 mm) to reduce the risk of bad calculations at the edges. We assume that the region is centered.

Load cycle identification

Three different systems can be distinguished. The first one is the DIC system, which provides the displacement field for the whole test, at 1313 steps, which corresponds to a time interval of 109,33 min (1 h and 49 minutes). The second system is a camera that took photos at a constant frequency of 1/20 Hz (one picture every 20 seconds) of the other side of the specimen without speckles. The camera captured also the current applied force and the horizontal top displacement. A total of 331 pictures were taken in the same time interval as for the DIC system. Both recording systems, DIC camera and second camera, took photos continuously, even during load stops. The third system is the recording of the deformation of each sensor (DT), strain gage and applied forces. The data acquisition is not continuous, such that no recording takes place during load stops.

A perfect match between the DIC and the DT measurements is therefore not possible in an accurate way. However, it was possible to identify the load steps among the 1312 steps from DIC analysis thanks to the second camera systems. From the camera taking pictures of the specimen and a screen with the applied load and horizontal displacement, the beginning and the end of an time interval, e.g. load step or load stop, could be defined with a 20 seconds-accuracy (respectively 4 DIC steps). The following cycle duration were estimated (LS = load step interval,

LB = load stop (break) interval):

- LS1 : 400 s
- LB1 : 240 s
- LS2 : 260 s
- LB2 : 360 s
- LS3 : 220 s
- LB3 : 700 s
- LS4 : 340 s
- LB4 : 440 s
- LS5 : 220 s
- LB5 : 560 s
- LS6 : 2580 s (43 min)

A specific number of DIC steps could be assigned to those time intervals by dividing each interval by 5 seconds (time interval of two consecutive DIC steps).

Once the number of steps belonging to each load step or stop is identified, which steps correspond to each interval should be determined. To do so, one particular event was taken into account: the occurrence of the major diagonal crack. From camera pictures, it is observed that the crack occurs at a load of approximately 309 kN and a horizontal displacement of about 2.61 mm. This rapid formation results in a deformation of sensor POT66 and POT59, which capture the relative displacement of points situated on the two sides of the crack. The relative displacement between two points on either side of the crack, based on the first 900 DIC steps, is represented in Fig. 5.6. It can be observed that a sudden deformation between the two selected points take place from step 344 to step 345. From pictures and experimental data it could be concluded that due to the occurrence of the diagonal crack, the force dropped suddenly and the loading was stopped in order to allow crack measurements, marking the start of a load stop interval. Therefore, the vertical lines delimiting load steps and stops (red vertical lines) are shifted in a way that a new load stop begins at step 345.

The previously estimated loading and load stop sequence seem to match well to the recorded deformation from DIC: The relative displacement in Fig. 5.6 increases during loading and remains globally constant during load stops.

It should also be noted that the spreadsheet containing DT and force measurements does not reveal the data acquisition rate. However it can be estimated as follows:

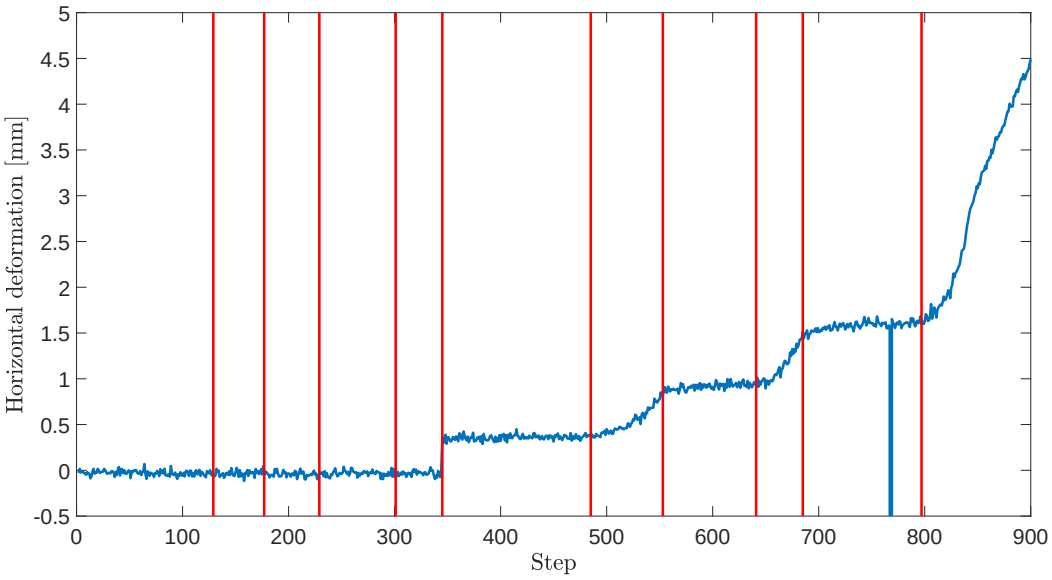

Figure 5.6: Relative displacement of two data points (DIC) representing the sensor POT66.

- For load step 4, about 142 DT measurements were recorded. For the same cycle, 68 DIC steps are available. The ratio is 2.09. Therefore, the data acquisition frequency is about 2.09 times higher than for DIC, which would correspond to a mean time interval of 2.39 seconds.

- For load cycle 5, about 89 measurements were recorded and 44 DIC steps are available. The ratio yields 2.02, which gives a mean time interval of 2.47 seconds.

It can be concluded that the data acquisition rate of experimental data is in the order of magnitude of 1/2.4 Hz.

Quality of DIC measurements

The displacement field is relatively noisy. The subset radius might have been chosen too small. A larger subset radius would have given a smoothing effect. Furthermore, the pictures used for DIC analysis are not completely stable. In fact, the image is slightly moving from one step to another. An immovable camera setup is crucial for good images. At step 768, a person ran in front of the DIC camera, which results in an aberrant measure. Aberrant displacements are also common during steps in the post-peak, which can be explained by big deformations and disintegration of concrete.

Another important observation could be made. From displacement field calculation it could be seen that around step 650, the camera connected to the DIC system moved considerably. This affects also the results of displacement field calculations. Fig. 5.7a and 5.7b illustrate the difference in displacement between step 645 and 650. This displacement, which is only due to a movement of the camera and not a deformation of the specimen, should thus be accounted for in the following steps. To

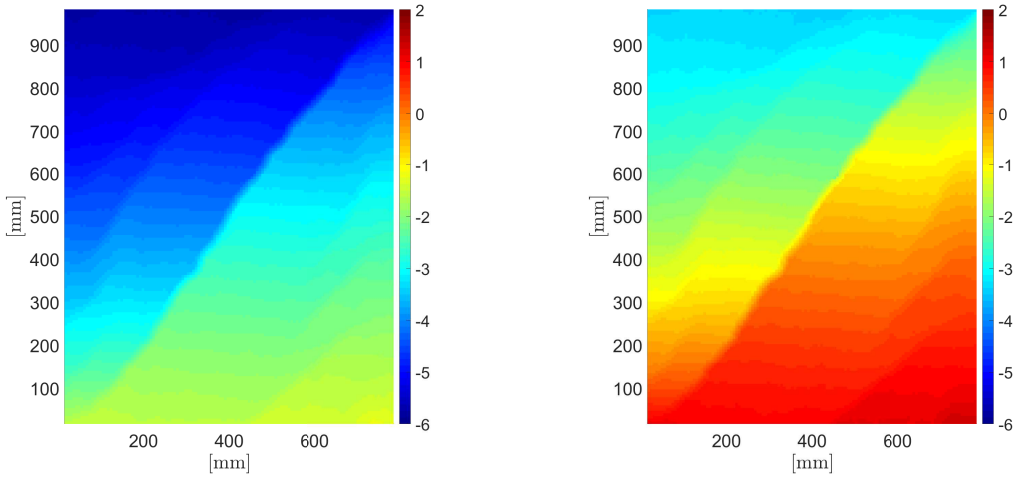

(a) Horizontal displacement field [mm] at step 645.

(b) Horizontal displacement field [mm] at step 650.

Figure 5.7: Horizontal displacement field before and after discontinuity.

do so, the difference between the mean horizontal displacement of steps 653 to 655 and steps 646 to 648 is computed for each data point. Every displacement field after step 649 will be corrected by subtracting the erroneous displacement, noted Δ_{vx}, from the DIC calculation. One should keep in mind that this camera movement was the most pronounced. However, photographs are not always stable throughout the complete test as mentioned earlier.

Peak load step

In order to compute shear mechanisms and to compare the kinematics from DIC to the 2PKT model, the peak load step should be identified. As described earlier, the matching of the different systems can not be done in a perfectly accurate way. The following estimation is done to estimate the peak load step:

- From time-lapse photos it could be seen that the development of the critical diagonal crack occurs between photo 88 and 89.
- Thanks to the monitor displaying the applied shear force and horizontal top displacement, it could be concluded that the peak is probably reached between photo 209 (displacement: 6.45 mm, shear force: 438.73 kN) and photo 210 (displacement: 6.74 mm, shear force: 451.62 kN).
- The difference in time is thus estimated to be $(209 - 88) \cdot 20 = 2420$ seconds. In terms of DIC, this corresponds to $2420/5 = 484$ steps.
- As mentioned earlier, the development of the crack takes place between step 344 and 345. Therefore, the peak load should be reached around step $345 + 484 = 829$.

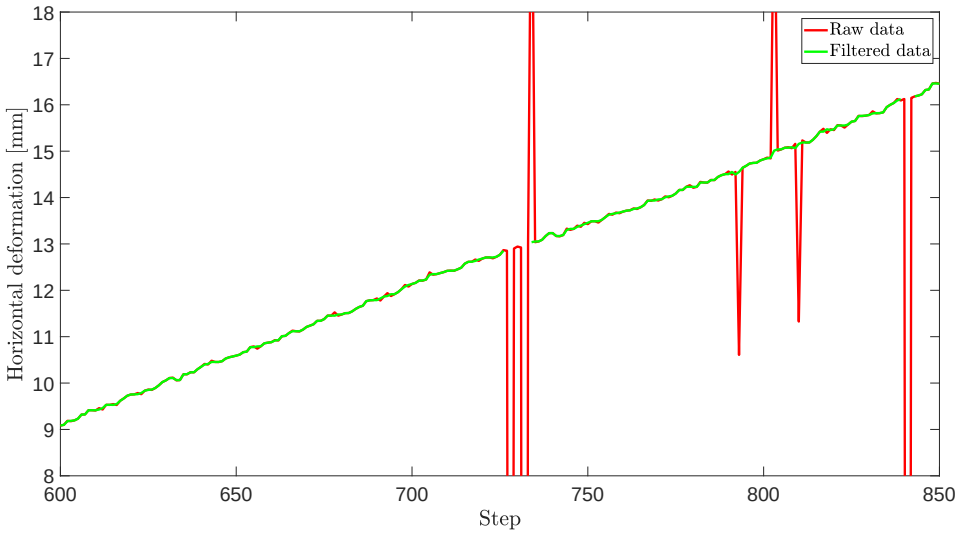

Figure 5.8: Effect of filtering DIC data in the post-peak region. The deformation corresponds to the relative displacement between two points on either side of the crack.

5.2.2 Comparison with DT measurements

In order to compare DIC measurements with DT measurements, the load stop intervals will be removed from the DIC data as they are not included in the recording of DT. For comparison, DIC data will be filtered in a simple way to remove aberrant values and to reduce the noise. Aberrant values are set to NaN and noise is filtered with the Matlab function `medfilt1`[1]. An example of the filtered data in the post-peak can be seen in Fig. 5.8.

The comparison will be done for POT66, POT59, web expansion and base cracks (Fig. 5.9).

POT66

The sensor POT66 measures the relative displacement between two points on either side of the critical crack close to the upper compression zone. A comparison of DT and DIC is represented in Fig. 5.10. It is important to note that the horizontal force is synchronous with the DT measurement since their data acquisition is identical. The load steps for DIC are only estimated such that they do not match perfectly. However, it can be concluded that, especially before the peak, the deformation is similar for DIC and DT, sometimes shifted due to uncertainties in terms of load intervals. In the post-peak, DIC deformation reaches higher values.

POT59

The transducer POT59 measures the same deformation as POT66 but near the bottom compression zone. The comparison between DIC and DT is given in Fig. 5.11. DIC computation is not reliable towards the end of the experiment because the point at the edge is highly disturbed due to disintegration of concrete. The

[1]The Matlab function `medfilt1` applies a third-order one-dimensional median filter to the data.

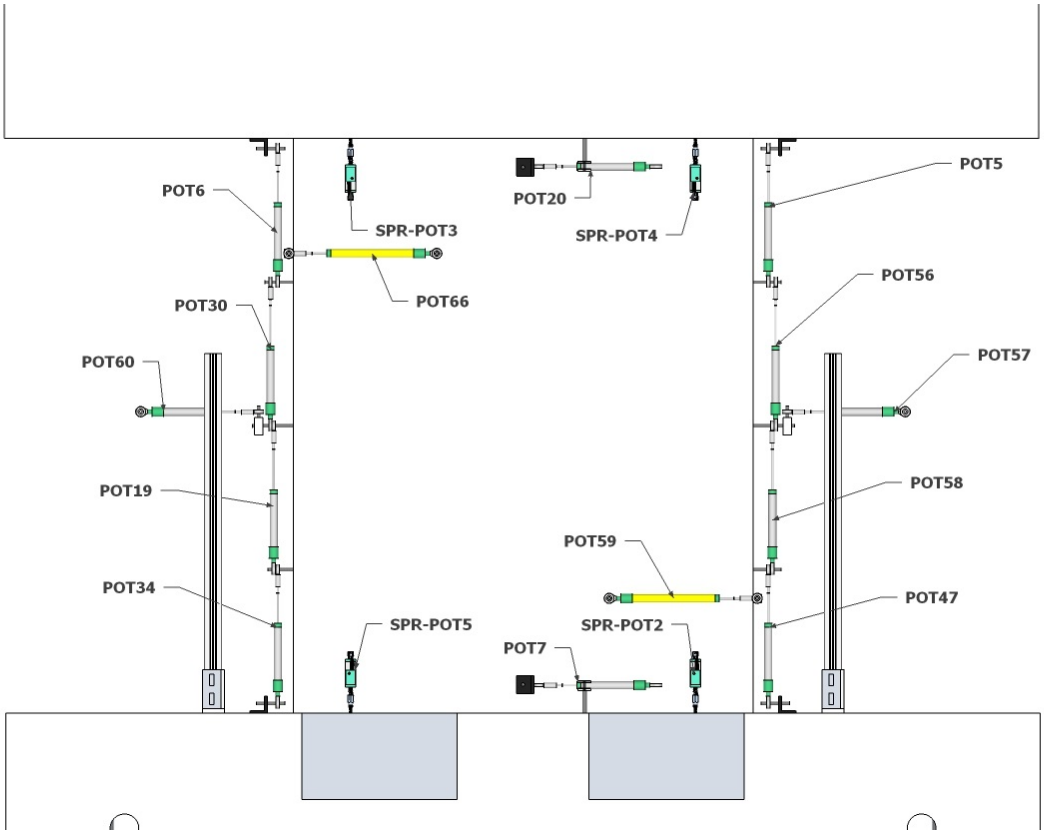

Figure 5.9: Implemented instrumentation of the coupling beam.

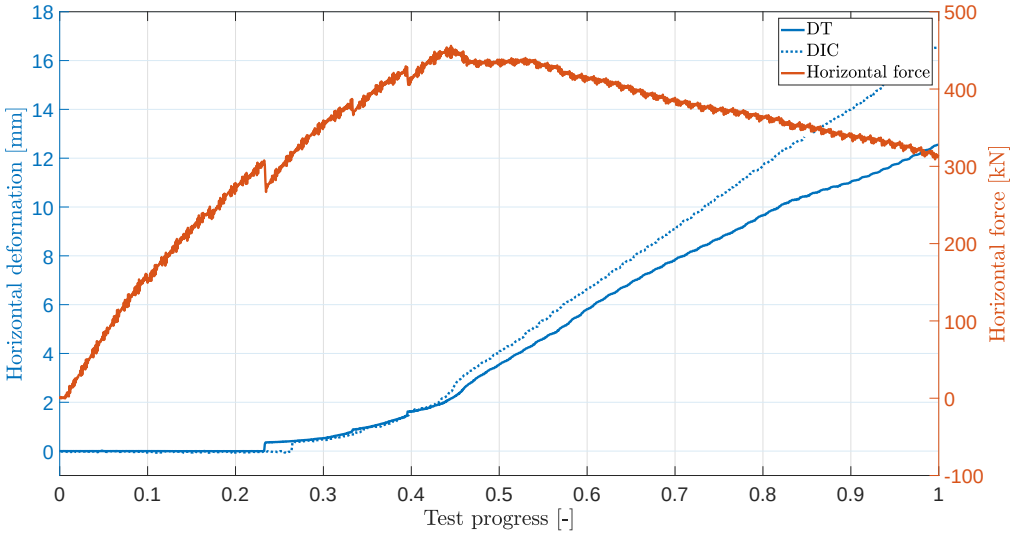

Figure 5.10: Comparison between DT and DIC for POT66.

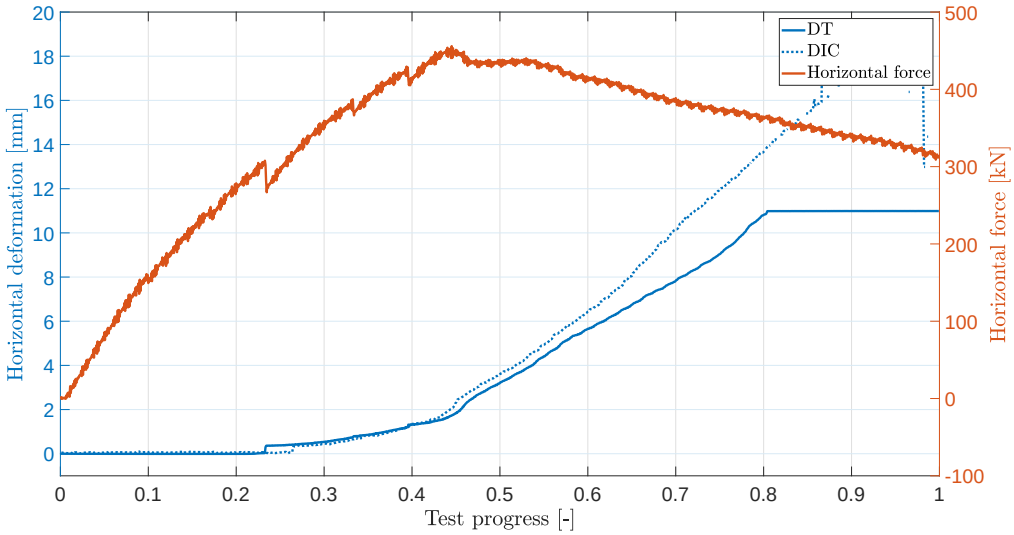

Figure 5.11: Comparison between DT and DIC for POT59.

same conclusions can be drawn as for POT66 as we have a good correlation between DT and DIC especially in the pre-peak zone. Towards the last 20% of the loading, POT59 stops recording additional displacement, because the transducer might have reached its deformation limit.

Web expansion

Sensor POT57 and POT60 measure the displacement of the sides during the test. The comparison between DIC and DT is given in Fig. 5.12. A surprising behavior takes place for the DTs. One can expect the POT57 to get shorter in a higher proportion than the POT60 to get longer, due to cracks that form in between. However, after 10% test progress, the web starts to contract according to the measurements from DTs. Indeed, from experimental data, we can see that POT60 starts recording a displacement earlier than POT57, which leads to the apparent contraction. The experimental setup might be the source of error. DIC computation, on the other hand, gives the expected evolution. A sudden increase in web expansion takes place at test progress 0.265, which corresponds actually to the development of the major diagonal crack. The global shape is similar for both curves.

Bottom base crack

The base crack is measured by SPR-POT5. It is compared to the vertical displacement of a point located in the theoretical position in the mask. The result is represented in Fig. 5.13. A large difference is visible. While the potentiometer measures a maximum crack opening of about 0.17 mm, the point from DIC computation moves vertically by ∼1.2 mm. This difference is significant and may be due to a different cracking pattern in the base region at the two faces of the specimen.

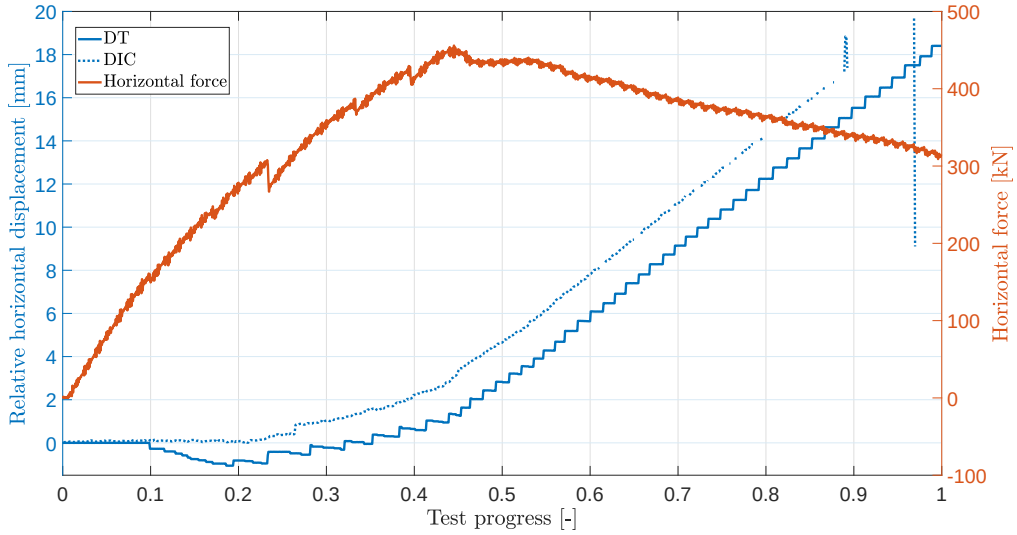

Figure 5.12: Comparison between DT and DIC for the web expansion.

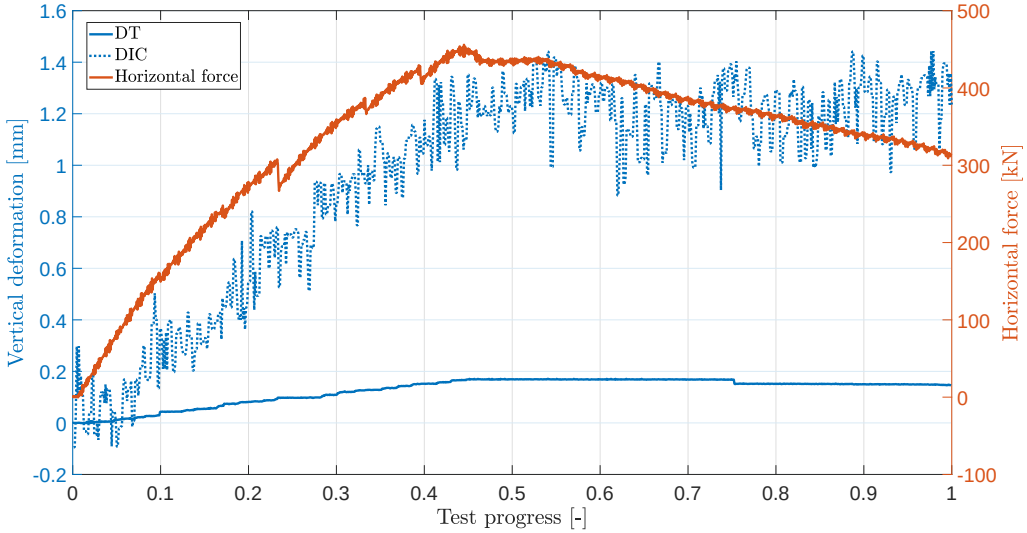

Figure 5.13: Comparison between DT and DIC for SPR-POT5.

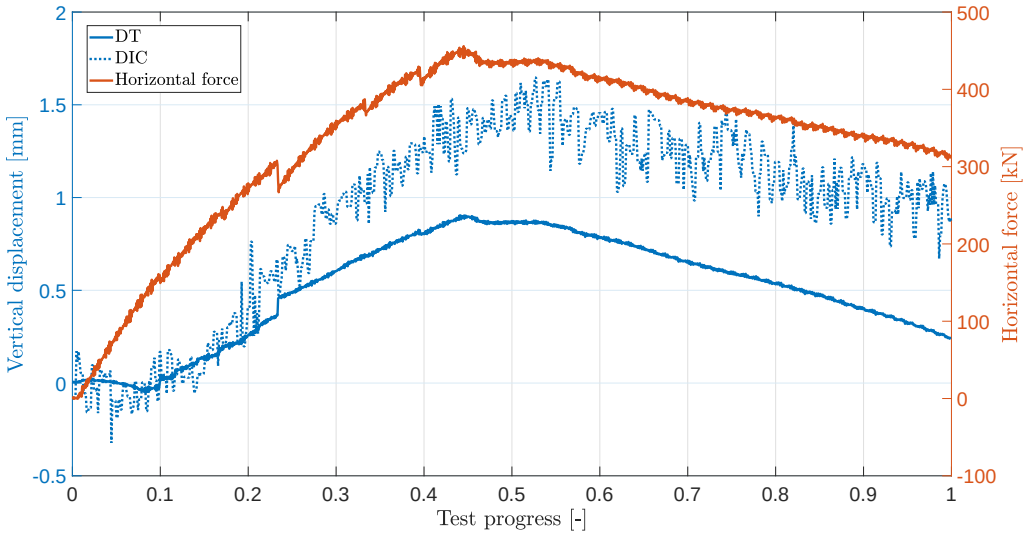

Figure 5.14: Comparison of absolute vertical displacement of point below crack, between DT and DIC.

Top base crack

A comparison with the crack opening of the top base crack, measured by SPR-POT4 is not straightforward. In fact, the potentiometer measures the relative displacement of two points: a point situated on the top block and a point below the supposed crack. From DIC computation, we obtain the absolute displacement for a grid of point. Therefore, we can compare the absolute vertical displacement of the point below the crack. To do so, we have to combine the DT measuring the vertical displacement of the top block with SPR-POT4. The result is represented in Fig. 5.14. At peak, the measured vertical displacement of the top block is 1.2 mm, and the relative displacement of the two measuring points of SPR-POT4 equals approximately 0.3 mm, which corresponds theoretically to the top base crack opening. Therefore, at peak, the vertical displacement of the measuring point on the specimen yields 0.9 mm. The DIC computation yields higher values, up to 1.5 mm. Apart from that, the overall shape of the curve is similar for both systems.

Top horizontal and vertical displacement

Fig. 5.15a and 5.15b show the horizontal and vertical displacement field at peak, obtained by averaging the displacements over steps 827 to 831 for noise reasons, having taken into account the displacement correction Δ_{vx}. Horizontal displacements are counted positive to the right. Vertical displacements are counted positive upwards.

The mean horizontal and vertical displacement of the top block at peak were measured by DT and their values are respectively 6.628 mm and 1.197 mm.

In terms of vertical displacement, a direct comparison between the displacements of the top edge of the mask and the measured displacement from DT is not straightforward. Indeed, local deformations like crack opening of the top base crack

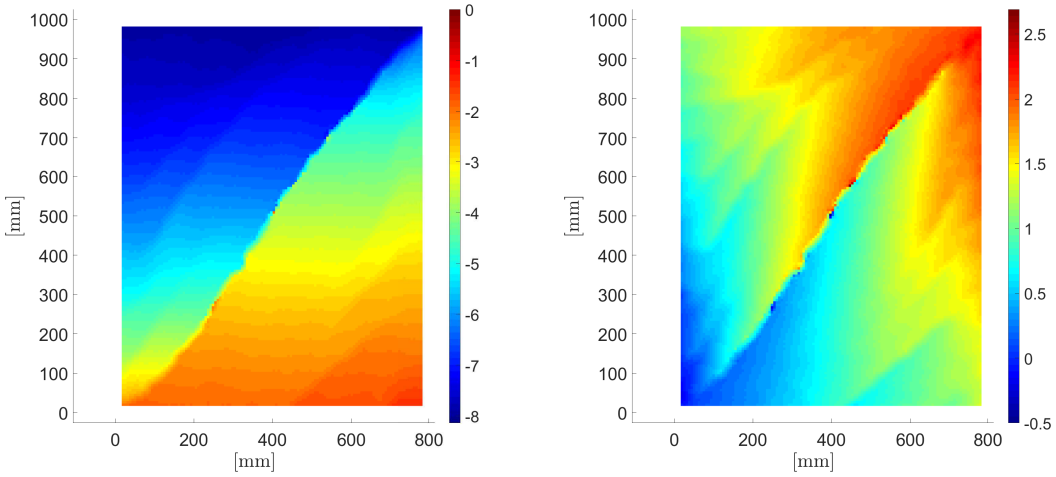

(a) Horizontal displacement field [mm] at peak.

(b) Vertical displacement field [mm] at peak.

Figure 5.15: Displacement fields at peak.

and compression of concrete in the right zone of the beam result in a nonuniform displacement along a horizontal line. On the contrary, displacement transducers measures a single value for the top block.

In terms of horizontal displacement, DIC values at the top of the mask are close to 8 mm while the measured horizontal displacement of the top block from DT is 6.63 mm. First of all, the measured displacement corresponds to the displacement of the top block with respect to the bottom block. However, a slip of the bottom block with respect to the floor could be measured (0.3308 mm) such that the absolute mean displacement, with respect to the floor, would be 6.96 mm. The DT measurement also accounts for the slip between the top block and the beam, measured by POT20. At peak, the slip reaches 0.43 mm. This slip is not accounted for in the DIC analysis. Finally, the absolute horizontal displacement of the top block reduced by the slip at the top interface is 6.53 mm. Thus, the difference between DT and DIC in terms of horizontal displacement at the top of the beam is of about 1.47 mm.
It should be noted that the values of the 2 displacement transducers measuring the horizontal displacement differ by almost 1 mm, which reveals uncertainties about the measurements. Furthermore, displacements from DIC analysis vary quite a lot around the peak. Unstable photographs and uncertainty regarding the chosen peak step may lead to slightly overestimated values.

5.3 Comparisons with kinematic model

In this section, the deformation pattern from 2PKT is compared to the deformation computed with DIC at peak.

5.3.1 Measured geometry and DOFs of kinematic model

The 2PKT predicts the deformation pattern of a short coupling beam based on 2 degrees of freedom. The deformation pattern is computed with the equations presented in Fig. 3.1. The DOFs are determined with experimental measurements and the angle of the critical crack is determined by observations.

The angle of the critical crack α_1 is estimated to be equal to the angle of the diagonal of the shear span with respect to the vertical axis:

$$\alpha = \arctan \frac{h}{a} = 38.66°, \tag{5.1}$$

where h is the depth of the beam and a corresponds to the shear span.

DOF 1 and 2 for 2PKT are concluded from potentiometers. DOF 1, $\varepsilon_{t,avg}$, corresponds to the average strain along the reinforcement. Thus, DOF 1 is taken as the vertical displacement of the top block at peak divided by the length of the beam:

$$\varepsilon_{t,avg} = \frac{v_{top}}{a} = \frac{1.197}{1000} = 0.001197. \tag{5.2}$$

DOF 2, Δ_c corresponds to the transverse displacement of the CLZ. It is taken as the mean value of the deformation measured in POT59 and POT66 at peak:

$$\Delta_c = \frac{POT59 + POT66}{2} = \frac{1.732 + 2.156}{2} = 1.944\ mm. \tag{5.3}$$

The kinematic model is computed by placing the origin of the 2PKT system of coordinates (x and z) in the bottom right corner of the face with speckles. Therefore, the CLZ is assumed to be at the bottom left corner of the specimen according to 2PKT. The x-axis is the longitudinal axis of the beam in the kinematic model.

5.3.2 Comparison of displacement fields

The displacement figures below are obtained with a coarseness factor of 15 such that every 15th data point will be taken as a vertex of the triangular mesh. The mesh becomes coarser and provides enhanced visibility.

The deformation pattern at peak from DIC and the kinematic model are represented in Fig. 5.16a and 5.16b, amplified by a factor of 15 (amplification factor = AF). As a reminder, the deformation computed with DIC is already corrected by $\Delta_v x$ (camera movement at step 649) and averaged over 5 steps.

The horizontal displacement δ_z of the top left point in the mask (with DIC-coordinates x = 14.44 mm, y = 986 mm) is the sum of the contribution from DOF 1 and DOF 2:

- δ_z DOF1: 1.496 mm.
- δ_z DOF2: 1.944 mm.

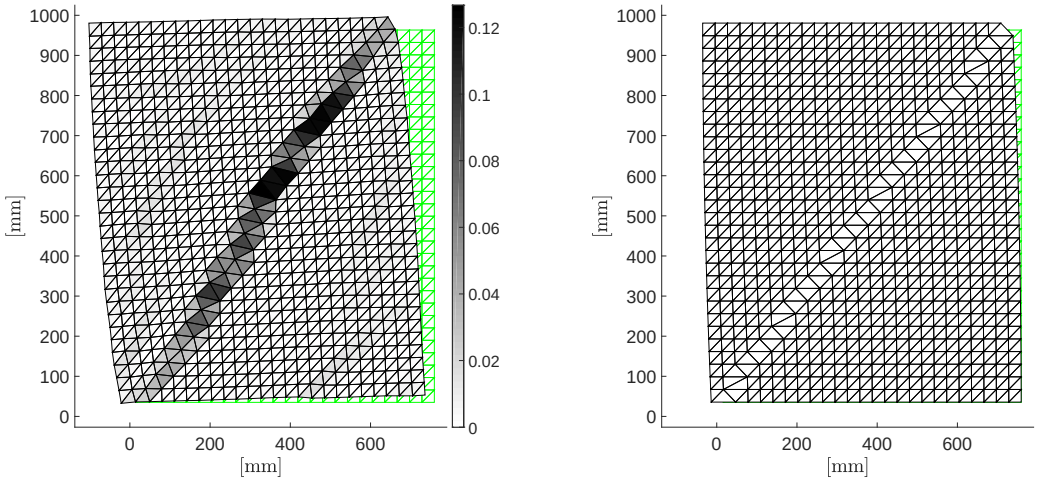

(a) Deformation pattern from DIC analysis with colorbar representing $|\varepsilon_1| + |\varepsilon_2|$ to illustrate damage, AF = 15.

(b) Deformation pattern from kinematic model (2PKT), AF = 15.

Figure 5.16: Deformation patterns at peak.

The difference between the predicted deformation pattern and the deformation from DIC is significant.

The following aspects must be taken into account for a proper comparison. While the DIC camera captures the absolute displacement field of the speckle pattern, the kinematic model only describes the deformation of the beam. The following movements were taken into account in the DIC analysis but not in the 2PKT, and their values at peak:

- The slip of the bottom block with respect to the floor: 0.331 mm [2].
- The slip in the crack of the beam with respect to the bottom block, measured by POT7: 0.670 mm.
- The pull-out of the reinforcing longitudinal bars on the tension side, estimated from strain gages values: 0.307 mm.

These deformations are illustrated in Fig. 5.17.

The pull-out of the longitudinal reinforcement is related to strains in the footing. The short coupling beam is supposed to be rigidly fixed to the wall. The wall is represented by the bottom block in the present experimental setup. When the beam is loaded, it deforms in a double curvature shape. At the basis, the longitudinal reinforcement is highly stressed on the tension side. The strains do not become directly zero at the footing. The reinforcing bars still carry strains into the footing over a certain length. This phenomenon is called "strain penetration effect". The pull-out of the reinforcing bars results in a rotation of the beam about a certain point. The point of rotation can be considered as the point dividing the lowest part of the beam in a compression and tension zone. Another way to define the point

[2] A second sensor measured 1.332 mm. Both sensors give different values for no obvious reason. The smaller one will be considered because it seems more probable to have only small slip.

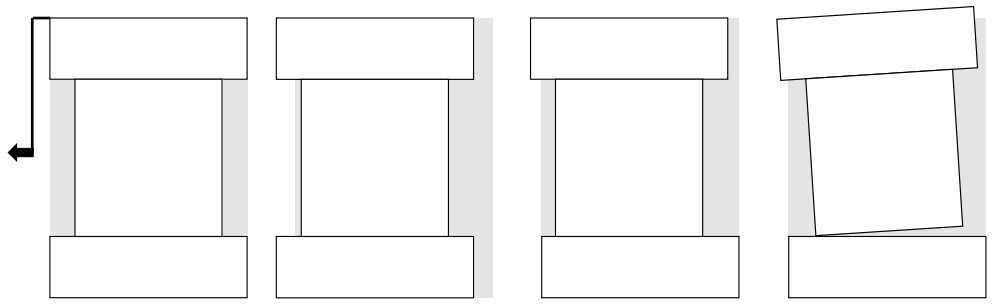

Figure 5.17: Secondary movements accounted for in DIC. From left to right: initial position, slip bottom block-floor, slip at interface beam-bottom block, pull-out.

in question is to look at the displacement field and define it as the point where the vertical displacement on either side is of different sign (e.g. points moving down to its left and up to its right). From Fig. 5.16a it can be seen that mostly every point tend to move upwards except for points very close to the left edge. For those reasons, the point of rotation is chosen at the bottom left corner of the beam. Consequently, the displacement field caused by the pull-out is calculated by small rotations. The angle of rotation is given by

$$\theta_{PO} = \frac{0.3074}{800 - 38} = 4.034 \times 10^{-4}. \tag{5.4}$$

The horizontal displacement due to pull-out for the top left point in the mask is then $-\theta_{Po}\, y = 0.398\ mm$.

The horizontal displacement of the top left data point (DIC) is -7.93 mm (already corrected by $\Delta_{vx} = 1.8311mm$). After removing the slip of the bottom block, the slip in the base crack and the horizontal displacement due to pull-out, the horizontal displacement of the top left point in the mask yields $-7.93 + 0.398 + 0.670 + 0.331 = -6.53\ mm$. The sum of displacement from DOF1 and DOF2 is only $1.496 + 1.944 = 3.44\ mm$, which corresponds to only 53% of the value from DIC. The modified deformation pattern from DIC is shown in Fig. 5.18.

In order to identify missing deformations in the kinematic model, the difference in deformations between DIC and 2PKT is shown in Fig. 5.19. They are obtained by subtracting the predicted kinematics from DIC deformation.

Comparing Fig. 5.19a with 5.19b shows that removing well known components from DIC improves the estimation of the kinematic model. The missing deformation can be interpreted as a shear deformation, as illustrated in Fig. 5.20.

5.3.3 Comparison of crack displacements

The 2PK model provides formulas for crack width (w) and slip (s) halfway along the crack (Eqs. (10)-(11) in Fig. 3.1). In order to compute w, l_k should be determined. Since the the angle of the critical diagonal crack is assumed to be equal to the angle of the diagonal of the shear span, l_k is equal to l_0. l_0 corresponds to the length of heavily cracked zone at the bottom of the critical diagonal crack when referring to the deformation patterns in Fig. 3.1. With l_k being equal to 118.1 mm and DOF 1 and 2, the crack width halfway along the crack yields 1.631 mm and the slip in the

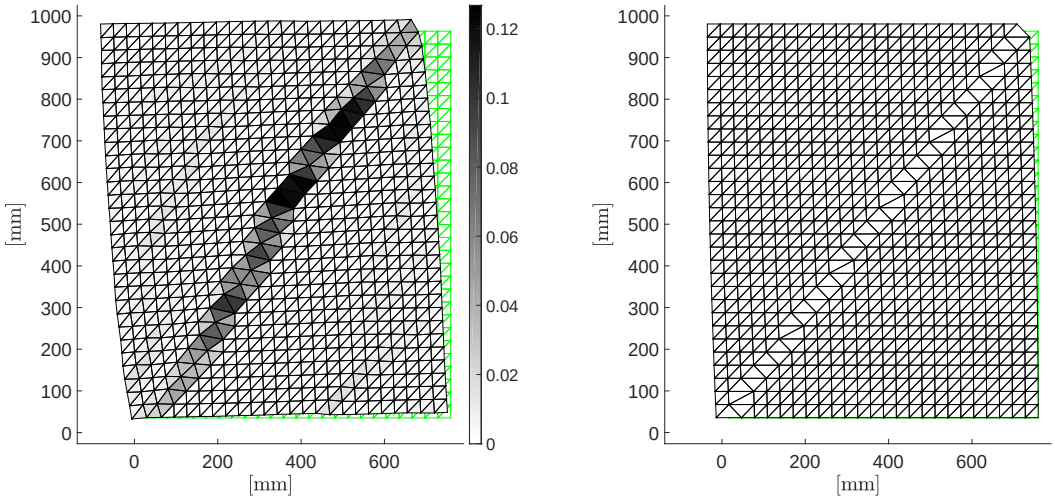

(a) Deformation pattern from DIC analysis with colorbar representing $|\varepsilon_1| + |\varepsilon_2|$ to illustrate damage, AF = 15, modified by removing the pull-out displacement, the slip in the crack and of the bottom block.

(b) Deformation pattern from kinematic model (2PKT), AF = 15.

Figure 5.18: Deformation patterns at peak.

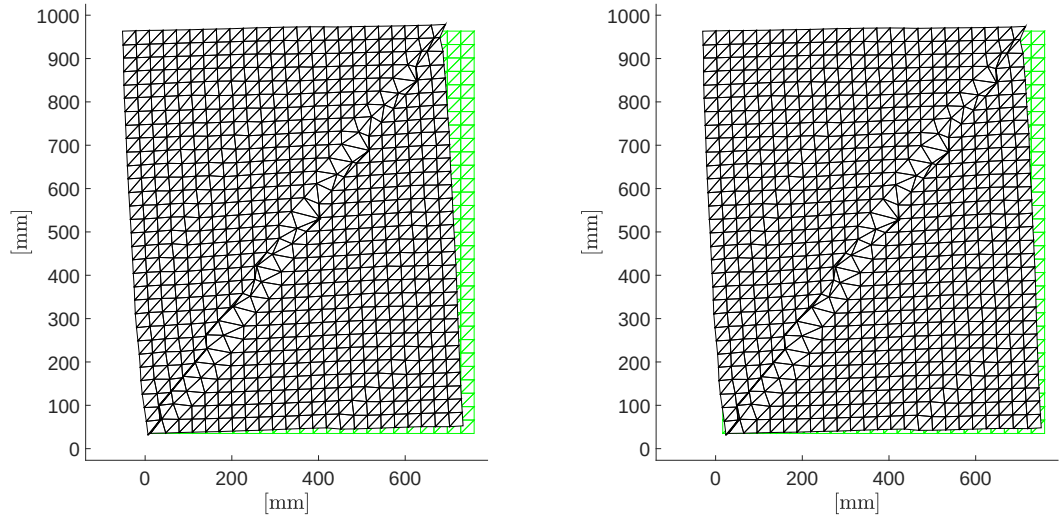

(a) Difference in displacement fields between DIC and kinematic model, unmodified DIC, AF = 15.

(b) Difference in displacement fields between DIC and kinematic model, modified DIC, AF = 15.

Figure 5.19: Comparison of displacement fields at peak (deformed positions of DIC subtracted by deformed positions of kinematic model).

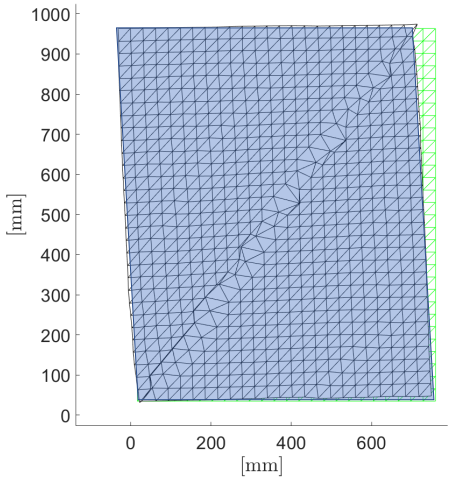

(a) Difference in displacement fields between DIC and kinematic model overlayed with missing shear deformation, AF = 15.

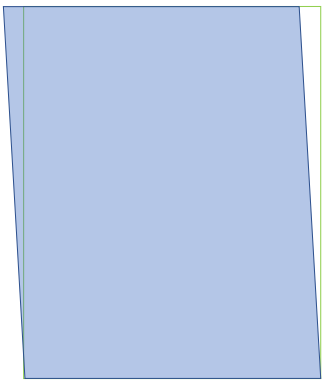

(b) Missing shear deformation, AF = 15.

Figure 5.20: Possible missing deformation in 2PKT.

crack yields 1.214 mm.

The crack kinematics based on DIC are computed along the critical crack in section 5.4.1. Halfway along the crack, the crack width is ~ 2.34 mm and crack slip is ~ 0.39 mm.

In conclusion, the crack width determined by 2PKT is about 30.3% smaller than measured with DIC. On the contrary, the slip is about 3 times higher compared to DIC.

5.4 Mechanisms of shear resistance

In this section, the shear-resisting mechanisms will be computed: aggregate interlock, shear transferred in the critical loading zone and shear contribution from stirrups. Finally, the total shear resistance is calculated and compared to the applied force at peak.

The free-body diagram illustrating the shear transfer mechanisms is depicted in Fig. 5.21.

5.4.1 Aggregate interlock

Interlock stresses are computed with three different crack models. The application of these models requires crack measurements, namely crack width and slip. Therefore, before stress calculation, the crack displacements are determined along the critical shear crack.

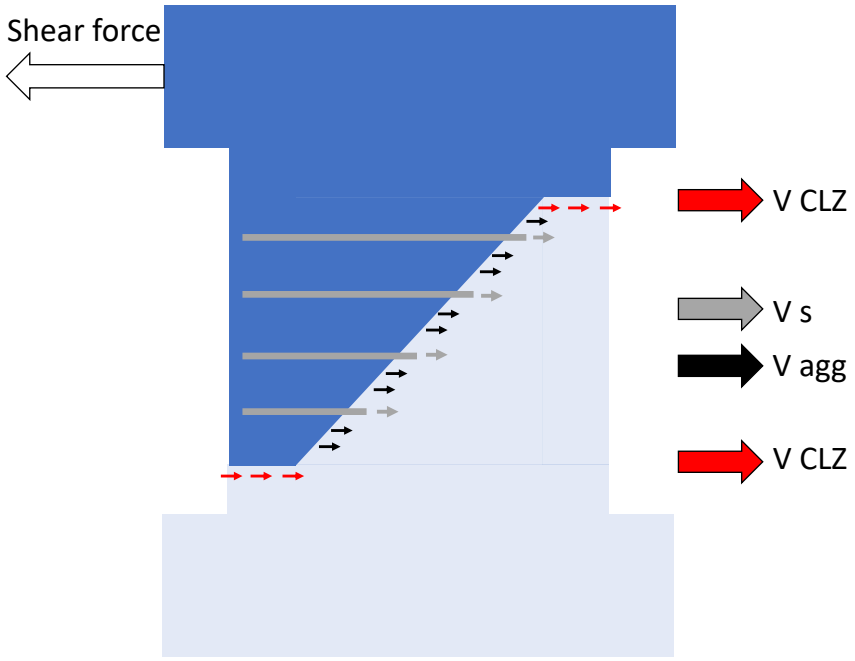

Figure 5.21: Free-body diagram with applied horizontal shear force and horizontal components of internal stresses.

Measured crack kinematics

Crack kinematics are computed from DIC for the displacement field at peak (averaged over step 827 to 831) according to the method explained in Appendix A. The critical diagonal crack is approximated by a polyline with segments approaching the crack over a vertical distance of about 31 mm. The crack is visualized thanks to the maximum principal strain field computed with the averaged displacement at peak for a coarseness factor of 3 (constant strain triangle mesh). The method could be applied for the main portion of the critical crack. However, in the end regions, where the crack is not very distinctive, the method is not applied. The crack width and slip are represented in Fig. 5.22.

It can be observed that crack width increases towards the mid-height of the beam and becomes smaller towards the bases. The slip, on the other hand, is mostly between 0.3 and 1 mm. The small slip values can be explained by the fact that the top block is not restrained by an axial force and can thus freely move vertically. Only the rotation of the block is prohibited and controlled by the two vertical actuators. As a consequence, when the crack forms, the two sides of the crack can open without bearing a significant sliding within the crack since the left part is not driven downwards due to an axial force.

Interlock stresses and shear contribution

Based on crack kinematics, interlock stresses are calculated with three different models presented in section 3.2.2: Contact Density Model (CDM), Pure Mechanics Crack Model (PMCM) and Two-phase model by Walraven (1980) (TPM). Each

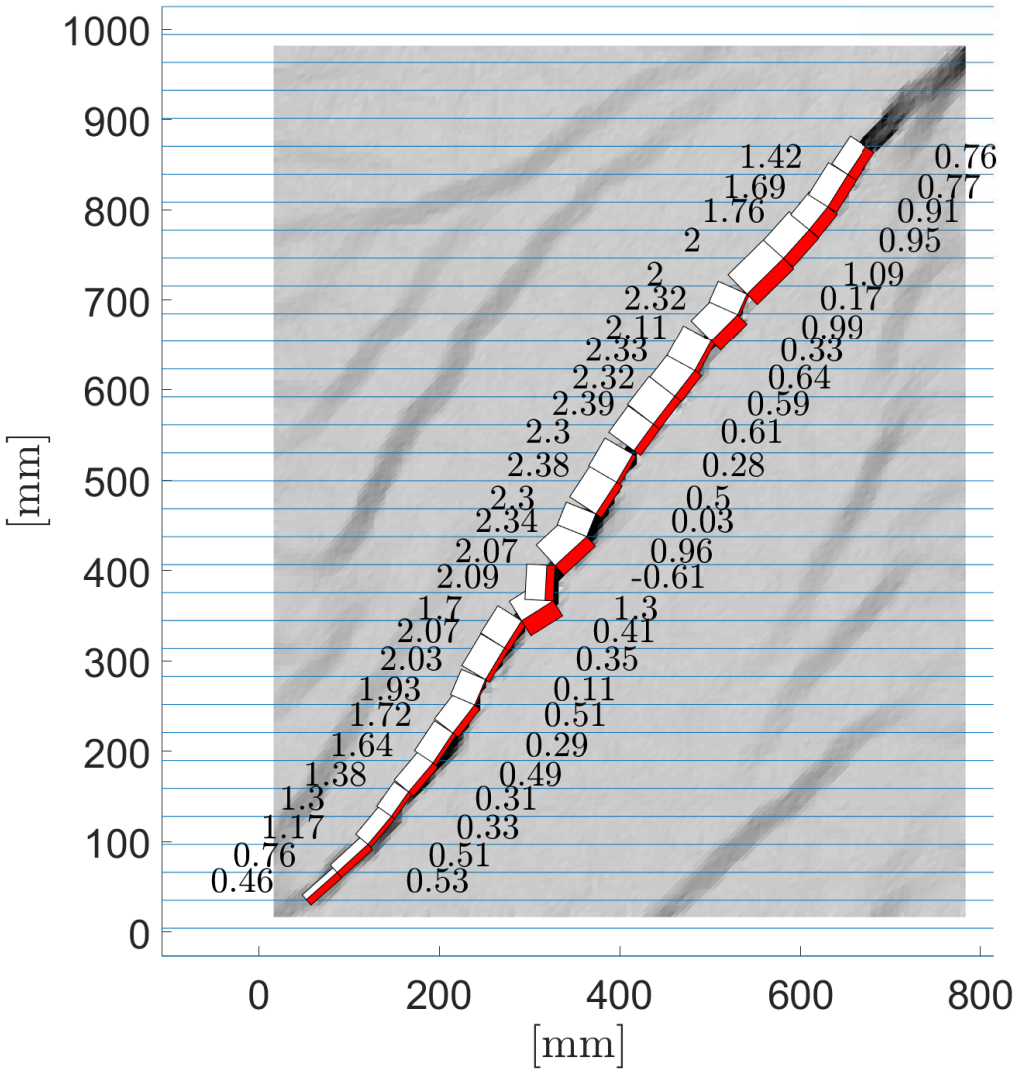

Figure 5.22: Crack width and slip computed from DIC at peak.

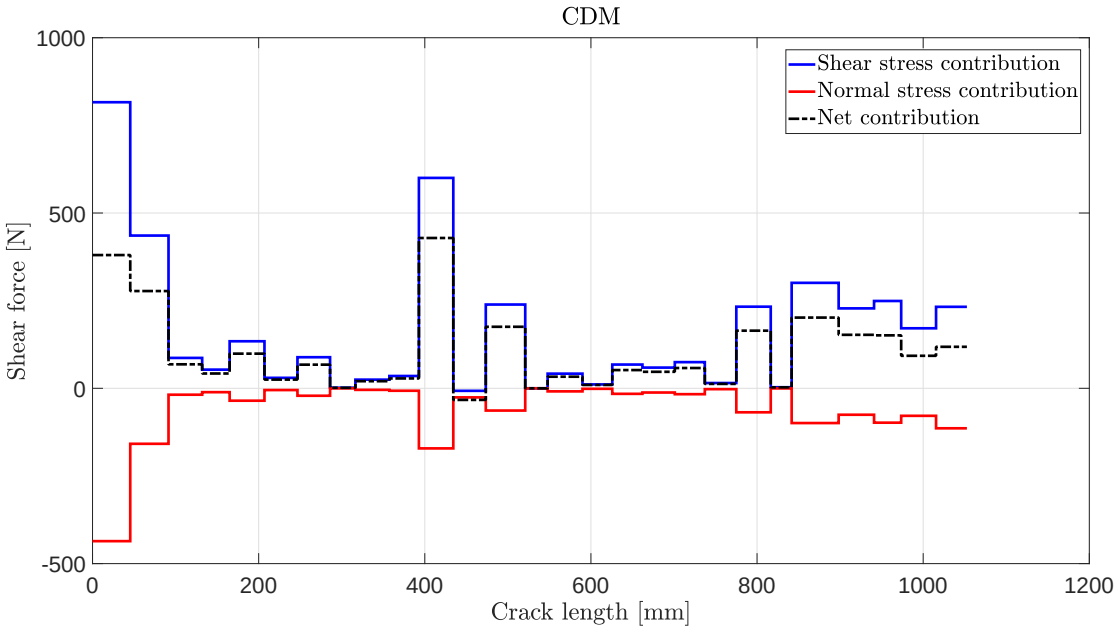

Figure 5.23: Stress contributions to total shear force transferred in the crack for CDM model.

model computes a shear stress and a normal stress for a crack segment. The shear force is then calculated by integrating the horizontal components of those stresses over the crack surface.

The following shear forces are obtained with the three models based on crack width and slip shown in Fig. 5.22:

- Contact Density Model (CDM): 114.7 kN.
- Pure Mechanics Crack Model (PMCM): 40.3 kN.
- Two-Phase Model (TPM): 28.6 kN.

Therefore, the contact density model achieves the highest value for V_{agg}. The shear stress contribution and normal stress contribution to the horizontal shear force is shown in Fig. 5.23, along the crack, starting at the bottom. High contributions are obtained for crack slips close to 1 mm in the top part of the crack and for small crack width at the two lowest crack segments (0.46 and 0.76 mm), but also for crack segments with a large crack angle.

5.4.2 Critical loading zone

Shear transferred in the critical loading zone is estimated by integrating shear stresses over a horizontal plane. For a coupling beam, the high compressive stresses are supposed to develop close to the end sections, to the left of the crack in the lower part and to the right of the crack in the top part. It is important to note that the 2PKT only accounts for one CLZ. However, in a symmetrical loading situation as in the test on the short coupling beam, there is no real reason for only one CLZ.

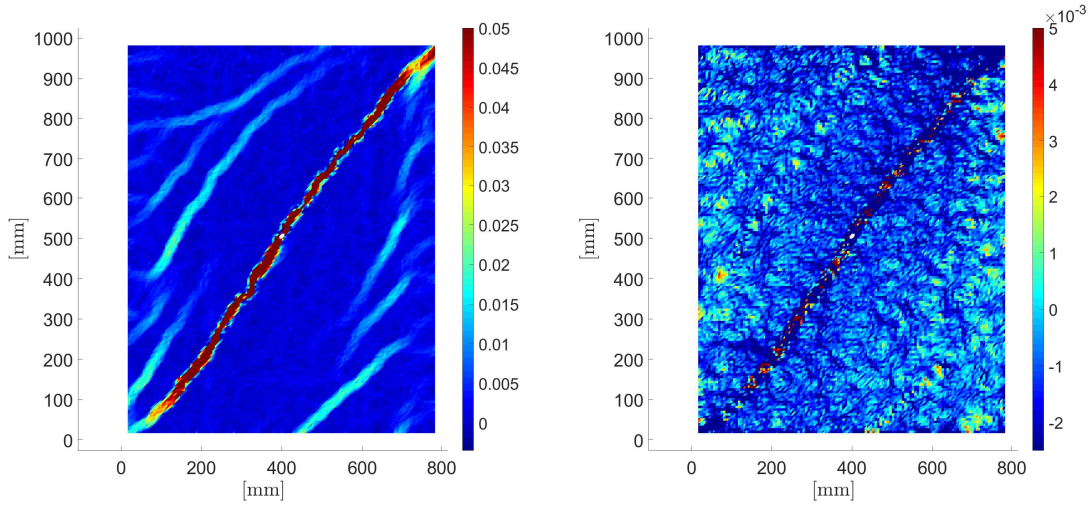

(a) Maximum principal strain field. (b) Minimum principal strain field.

Figure 5.24: Strain fields.

Hence, two critical loading zones are considered in the following.

To compute stresses, strains must first be evaluated. They are computed with the finite element formulation for constant strain triangles. Therefore, a mesh of triangles is formed based on the grid of data points.

Strains

As can be seen in Fig. 5.24, maximum and minimum principal strain calculation give a relative irregular strain field. This is partially due to the small step size used in the DIC analysis, which gives a high resolution (1 data point every ~ 2 mm), but the resulting strain fields are not smooth. The strain fields are obtained considering constant strain triangles with a length of $3\times$ the step size.
The minimum principal strain field does not reveal distinctive compression zones in the top right corner, right to the crack, or in the top left corner, left to crack. Indeed, in those zones, several triangular elements are not blue-colored, indicating tensile strains. The same phenomenon is observed for ε_y strain field depicted in Fig. 5.25. One could expect compressive vertical strains in those locations, which is not the case, especially in the top zone. Generally speaking, those zones can be described as disturbed, by the formation of several cracks (as seen in photos at that loading stage). This phenomenon is illustrated in Fig. 5.26, where several little cracks were identified and marked at the top during the previous load stop. In the bottom zone close to the critical crack, those little cracks were not traced. These results are consistent with the crack pattern revealed by the maximum principal strain field.

The location of the horizontal cuts (see FBD) in the beam should ideally be at the height where the critical crack starts to disperse and the shear transfer mode changes from aggregate interlock to shear transferred through high compression. Since the plots of strain fields do not reveal a clear indication of the location, stress fields are investigated. The criterion for the plane position is thus chosen to be the

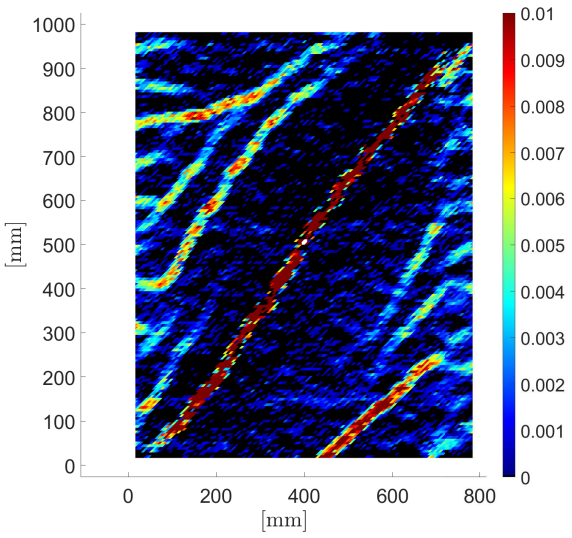

Figure 5.25: ε_y strain field. Negative (compressive) strains are represented in black.

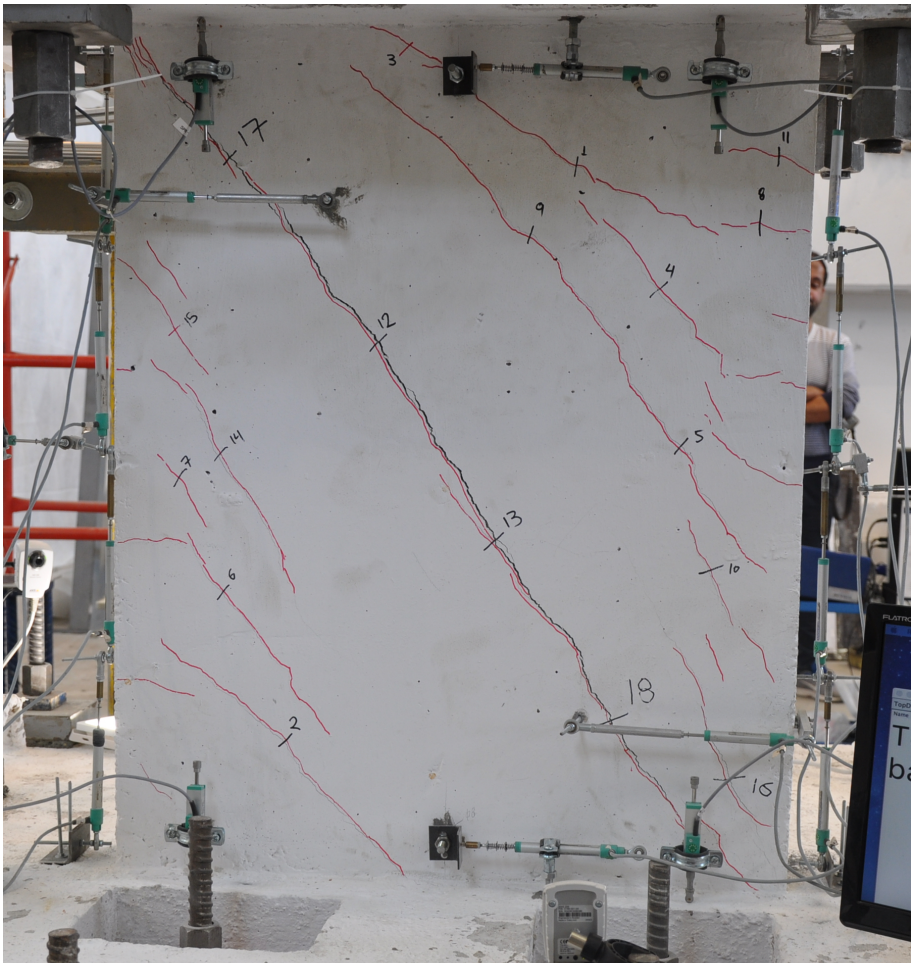

Figure 5.26: Test specimen (opposite side of DIC frame) close to peak force.

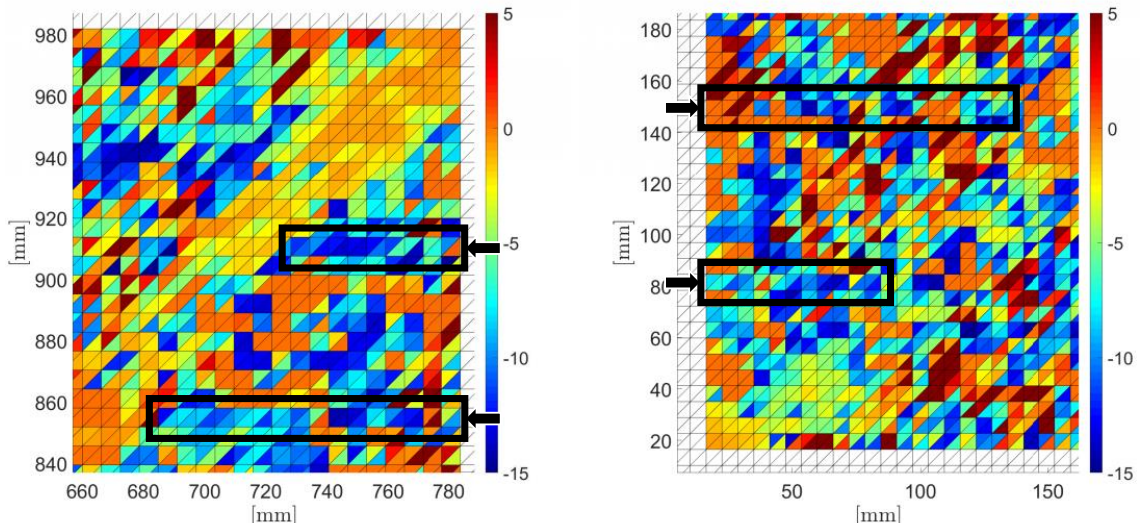

Figure 5.27: Shear stresses τ_{xy} in the top right corner (left figure) and in the bottom left corner (right figure).

plane, which maximizes the value of V_{CLZ}.

Stresses and shear contribution

Fig. 5.27 shows shear stresses τ_{xy} in the top right corner and in the bottom left corner of the mask. As can be seen, the finite element computation leads to a relatively noisy stress field, with high variability from one triangle to adjacent triangles. However, two horizontal planes could be identified with throughout negative shear stresses (blue triangles). One is located at height 911 mm and the other one at height 855 mm (see black rectangles in Fig. 5.27). Similarly, two planes in the bottom left corner are promising for a high shear force because of relatively high (negative) shear stresses. In order to find the maximum V_{CLZ} close to the CLZ, the shear force will be determined for these 4 discrete planes.

Thus, by integration of horizontal shear stresses over these planes reaching from the edge of the specimen to the critical diagonal crack, the following shear components are obtained. The smaller absolute value is generally obtained with compression-softening law and the highest absolute value according to uniaxial compression law.

- Top right corner:
  - Height = 911 mm : $V_{CLZ} \in [70; 96]$ kN, as shown in Fig. 5.28. The exact values are:
    - Biaxial failure criterion: 78.6 kN
    - Uniaxial compression: 95.3 kN
    - Compression-softening: 70.3 kN
  - Height = 855 mm : $V_{CLZ} \in [100; 140]$ kN.
- Bottom left corner:
  - Height = 150 mm : $V_{CLZ} \in [74; 100]$ kN.

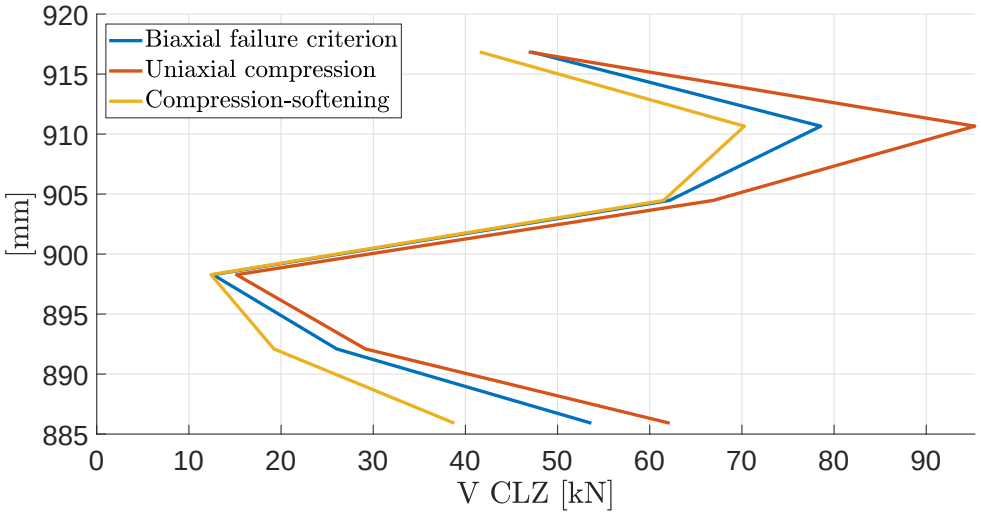

Figure 5.28: Evolution of shear in CLZ along height.

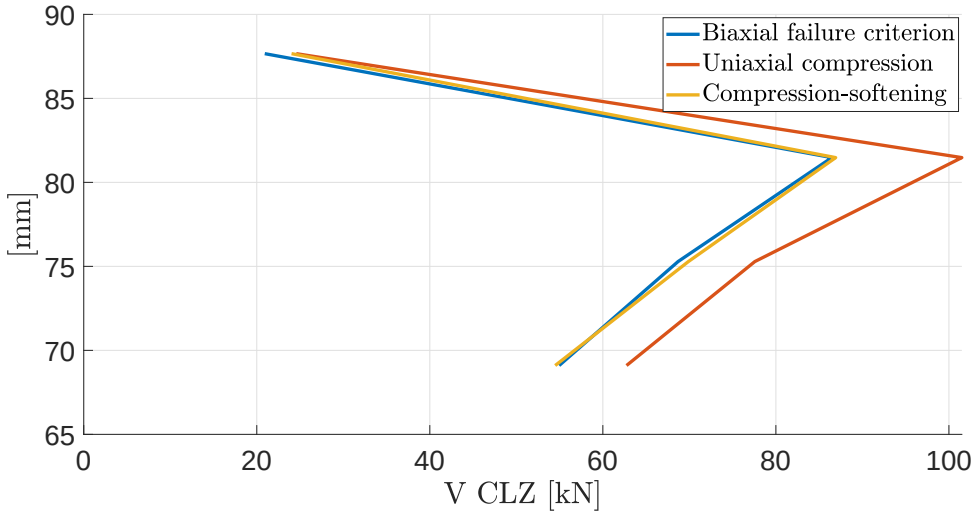

Figure 5.29: Evolution of shear in CLZ along height.

- Height = 81 mm : $V_{CLZ} \in [86; 102]$ kN. The exact values are:
  - Biaxial failure criterion: 86.5 kN
  - Uniaxial compression: 101.5 kN
  - Compression-softening: 86.9 kN

It is decided to select the planes at height 81 mm and 911 mm. The shear force according to compression-softening law are respectively 86.9 kN and 70.3 kN. The variation of shear stress along those planes is shown in Fig. 5.30.

5.4.3 Stirrups

The third shear-resisting mechanism taken into consideration is the tensile stress in the stirrups. As can be seen in Fig. 2.12, two stirrups are placed very close to the end sections and are therefore not intersected by the cut for the free-body

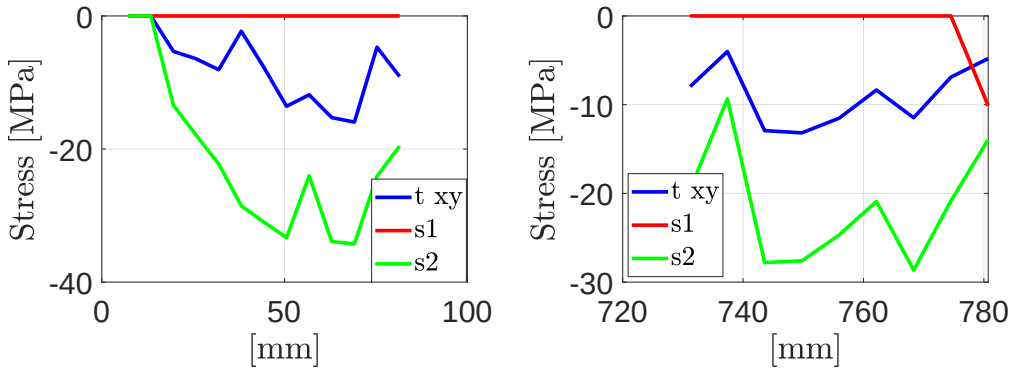

(a) Stresses along horizontal line at height 81 mm.

(b) Stresses along horizontal line at height 911 mm.

Figure 5.30: Stresses along chosen planes (max. principal strain s1 = σ_1; minimum principal strain s2 = σ_2; shear stress txy = τ_{xy}) computed with compression-softening law.

diagram. Hence, if only 4 among 6 layers of stirrups are considered to yield, the shear transferred across the crack through stirrups is $V_s = 204.7\ kN$.

5.4.4 Total shear force

The total shear force resisted by aggregate interlock, critical loading zone and stirrups is obtained by adding up all three contribution.

The free-body diagram (Fig. 5.21) should be recalled. The horizontal cuts were performed at height 81 mm and 911 mm for V_{CLZ}. Therefore, the aggregate interlock should only be computed for the crack reaching from the bottom horizontal plane to the top horizontal plane. The shear resisted through aggregate interlock was obtained for the crack reaching from height 35.8 mm to 869.9 mm. The crack length of the missing part at the top is very close to the crack segment that was mistakenly accounted for in the bottom. It is assumed that the aggregate interlock in the bottom part, below the CLZ plane, is balancing the missing aggregate interlock contribution in the top part. By choosing the aggregate interlock value from CDM, the 3 contributions to the shear force are summed up:

$$V_{tot} = V_{CLZ,1} + V_{CLZ,2} + V_{agg} + V_s = 70.3 + 86.9 + 114.7 + 204.7 = 476.6\ kN. \quad (5.5)$$

The applied shear force at peak was 455.9 kN. With the CDM for interlock stresses, the difference in shear force is only 4.54%.

Choosing PMCM instead of CDM, $V_{tot} = 402.2\ kN$. The total applied shear force at peak is 455.9 kN, which gives a difference of 11.78%.

With the two-phase model for aggregate interlock, $V_{tot} = 390.5\ kN$ (14.34% of difference).

Hence, the Contact Density Model gives the highest aggregate interlock and the best balance between total resisted shear force and applied shear force.

The contribution from stirrups is the largest (45%), followed by the sum of the critical loading zones (35%). The missing shear resistance comes from aggregate interlock (20%).

Chapter 6

Conclusion

This thesis aimed at analyzing DIC data from two tests, one test on a short shear wall and another test on a short coupling beam. The goal of the tests is to acquire new knowledge about the shear behavior of non-slender structural members. Both tests were completely independent from each other: They were tested in different labs, with different experimental setups and different DIC systems. Even though these tests originated from different experimental campaigns, the same questions were raised and should be answered. The thesis focused on the use of Digital Image Correlation in order to provide answers.

The technique allowing to compute displacements and deformations by means of a series of images had to be understood. The calibration procedure, which is crucial for obtaining reliable results, had to be reviewed for the shear wall. In fact, for specimens of large dimensions, two cameras are employed. The calibration should be adapted such that a good mapping of both camera frames is possible. The processing is the next step of the analysis. The processing of large amounts of data sets of images can be a time and storage space consuming procedure. General principles and notions regarding processing parameters were described and their practical applications on real tests illustrated.

The validation of DIC measurements is generally not a straightforward process. Different independent measurement systems are useful for validation of DIC and global comparison. However, in this thesis, it was also illustrated how complex comparisons between different systems can be. A major issue is the non-synchronous data acquisition. In fact, most systems have their proper measuring rate and not every system is measuring during the same time intervals. If synchronous data acquisition is not possible in a test, one should make sure that it will still be possible to place every measured data at the right position in time. For the test on the short coupling beam, the coordination of the different sets of data was particularly challenging. For both tests, the validation of DIC measurements was performed by comparing displacements of discrete points of the DIC grid with measurements from displacement transducers. For the shear wall, the displacements and deformations computed with DIC were generally higher compared to measurements from displacement transducers. For the coupling beam, most of the measurements were similar.

After the validation of the DIC measurements, the deformation patterns of the test specimens were studied. A coarse mesh of triangular finite elements is suitable for this purpose. One main objective was to validate the kinematic model of the 2PKT for coupling beams and of the 3PKT for shear walls. It is important to note that the displacement field from DIC could not directly be used for comparisons with the kinematic models. Indeed, DIC computes the absolute displacement field of the speckle pattern, while the kinematic model only predicts the deformation of the specimen independently from any experimental setup. Due to practical conditions, secondary movements were captured by DIC and could be quantified by well positioned displacement transducers. Those movements were first subtracted from the DIC data in order to get a proper comparison with the kinematic model. The application of the kinematic model requires 3 degrees of freedom for the shear wall and 2 DOFs for the coupling beam. The installation of displacement transducers in appropriate positions was necessary in order to measure the required degrees of freedom. Based on the measured DOFs, the whole deformation pattern is obtained from the kinematic model.

The difference between the kinematic model for shear walls and the DIC measurements was relatively small. The top horizontal displacement was only underestimated by about 10% with respect to the horizontal displacement from DIC. The overall shape of the predicted deformations is in a good agreement with the real deformation. In terms of crack width and slip halfway along the crack, 3PKT computes 57% higher crack width, whereas the slip is approximately the same as the one based on DIC.

Regarding the coupling beam, the difference between the predicted deformation and the deformation computed with DIC was higher. The top horizontal displacement is roughly half of the displacement from DIC. More importantly, the deformation missing in the 2PKT can be interpreted as shear deformation. This information is valuable for possible improvements of the 2PKT. In terms of crack kinematics, 2PKT predicts a slightly smaller crack width than DIC. On the contrary, the slip is about 3 times higher compared to DIC.

The thesis also aimed to compute shear-resisting mechanisms based on kinematics obtained with DIC. Similar studies were already performed for slender elements. In this thesis, similar approaches are used to evaluate the load-bearing mechanisms in the short coupling beam and wall. To do so, kinematics from DIC along failure planes were combined with local constitutive laws to evaluate the contribution from each shear mechanism. Three mechanisms are considered governing: aggregate interlock, stirrups and shear transferred close to the critical loading zones.

For the critical loading zone, a method to compute strains based on displacement fields had to be applied. The constant strain triangle formulation was presented and applied to both tests. It could be seen that this method has some disadvantages. It is, for example, highly sensible to noise in the original data. In the case of the shear wall, the mask was split in 4 regions because three steel bars disturbed the images of the speckle pattern. This caused unreliable strain data on the contours. The subsequent stress calculation is performed based on constitutive laws. Three

different laws were compared for the compression-tension regime in order to illustrate the differences. The law accounting for compression-softening in the critical loading zone was chosen for the calculation of V_{CLZ}. From experimental data, the horizontal failure planes could not be identified in a straightforward way. It has been chosen to choose the plane with the highest shear force close to the disturbed zone.

In terms of aggregate interlock, crack kinematics along the critical shear crack had to be determined. An approach for this computation was established based on the displacement of two rigid bodies on either side of the crack. Using the obtained crack width and slip, three crack models were implemented to evaluate shear and normal stresses on the crack. It could be seen that, for example, the Contact Density Model produces the lowest aggregate interlock for the wall but the highest for the coupling beam, compared to the other two models.

The shear contribution from stirrups was estimated based on the yield stress of the bars intercepted by the critical crack.

The total shear force resisted by these 3 mechanisms was, for both applications, in the same order of magnitude as the measured applied force. For the wall, the sum of all contributions was the closest to the applied shear force when considering the Contact Density Model for interlock stresses. The difference was only 2.69%. The same applies to the short coupling beam. With the Contact Density Model, the difference between applied shear force and resisted force is only of about 4.54%. From this point of view, this crack model seems to be adequate. In the coupling beam, about 45% of the applied shear force is estimated to be resisted by transverse reinforcement. The critical loading zones account for roughly 35%. The missing 20% is assumed to be transferred through aggregate interlock.
The shear wall was only provided with a few stirrups. The contribution from stirrups is estimated to be about 16%. The shear resisted in the critical loading zone is about 76% of the applied force. The missing 8% come from aggregate interlock.

6.1 Future work

The results in this thesis are based on DIC measurements. Further understanding of the DIC systems, their practical applications and limitations would be useful to improve the accuracy and the reliability of the measurements.

The kinematic models can be reviewed based on the findings of this thesis. Especially for the short coupling beam, the deformation pattern predicted by the model could possibly be improved. It could also be interesting to point out the differences in shear mechanisms between the kinematic models and the results based on DIC.

The strain calculation was performed with a finite element formulation. It could be seen that the computation of the strain fields is sensible to noise in the data. Therefore, the application of techniques for smoothening of strain fields could be

investigated in the future.

The performed evaluation of shear mechanisms is suitable for deep members like short coupling beams and shear walls, presenting a critical diagonal crack and highly stressed regions close to the end sections. The evaluation of each contribution is based on different approaches, constitutive laws and crack models. Even though the Contact Density Model for aggregate interlock appears to give the best result, one should keep in mind that several assumptions regarding the other two mechanisms can have big impacts. For future work, the sensibility of each shear mechanisms in function of the assumptions could be evaluated in order to become more confident about the results.

One main concern is the definition of the contours of the critical loading zones. Hence, developing a general criterion that is applicable to the data from DIC could be considered. The computation of stresses in the CLZ needs constitutive relations. Enhanced constitutive modelling of concrete in the CLZ could be done in order to get reliable results.
Regarding aggregate interlock, further comparisons and validation of different models can be done.
Furthermore, the computation of the contribution of the stirrups can be improved by, for example, accounting for a more complex yielding behavior.
In addition to the three presented mechanisms, a forth contribution to shear resistance could be considered and calculated in the future: the contribution from the dowel action.

Appendix A

Crack kinematics methodology

The inclined crack is approximated by a polyline. One crack segment is delimited by two points c. The angle of the crack with respect to the vertical axis is defined as α_{cr} and determined thanks to the coordinates of points c_i and c_{i+1}. The displacement fields of two rigid bodies located at both sides of the investigated crack are determined separately, based on the displacement vectors of two discrete points (P1 and P2 for the left body, P3 and P4 for the right body).

Fig. A.1 shows a schematic of the crack model. The displacement field calculation is only described for the rigid body on the left side of the crack (rigid body 1). The approach is identical for the right one (rigid body 2), by replacing the subscripts 1 and 2 (corresponding to points $P1$ and $P2$) by 3 and 4.

The displacement field for the rigid body 1 is computed as a uniform translation of $(dP_{2,x}, dP_{2,y})$ combined with a rotation about point $P2$.

The rotation θ_1 (positive counter-clockwise) about point $P2$ can be approximated by the mean value of

$$\theta_x = -\frac{dP_{1,x} - dP_{2,x}}{\Delta y_{1,2}} \tag{A.1}$$

and

$$\theta_y = \frac{dP_{1,y} - dP_{2,y}}{\Delta x_{1,2}} \tag{A.2}$$

The displacement of the point in the crack computed with the previously described displacement field for rigid body 1 gives

$$df_{1,x} = dP_{2,x} - \theta_1 \, \Delta y_{2f} \tag{A.3}$$

$$df_{1,y} = dP_{2,y} + \theta_1 \, \Delta x_{2f}. \tag{A.4}$$

The coordinates of the point in the critical crack in the deformed position yields

$$f_{1,x} = f_x + df_{1,x} \tag{A.5}$$

$$f_{1,y} = f_y + df_{1,y}. \tag{A.6}$$

The displacement of the point in the crack computed with the displacement field for rigid body 2 gives

$$df_{2,x} = dP_{4,x} - \theta_2 \, \Delta y_{4f} \tag{A.7}$$

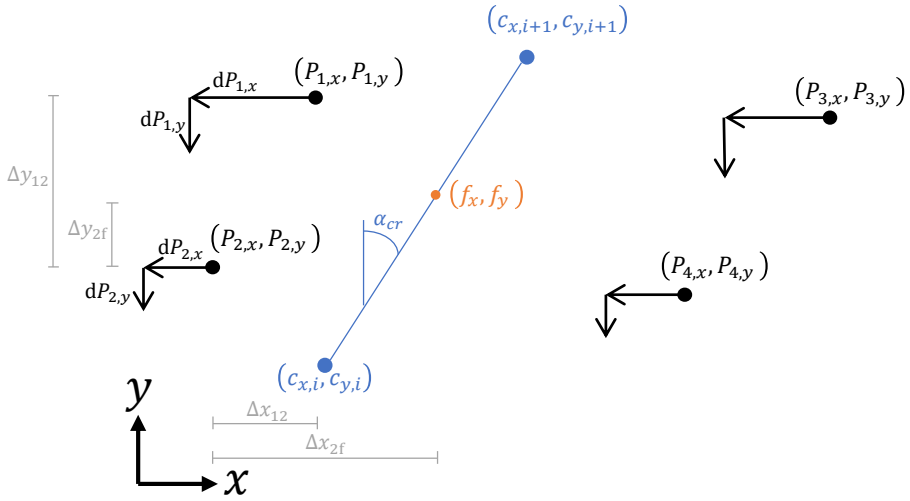

Figure A.1: Modelled crack segment and rigid body displacement. The arrows are displacement vectors (e.g. output of DIC analysis).

$$df_{2,y} = dP_{4,y} + \theta_2 \, \Delta x_{4f}. \tag{A.8}$$

The coordinates of the point in the critical crack in the deformed position yields

$$f_{2,x} = f_x + df_{2,x} \tag{A.9}$$

$$f_{2,y} = f_y + df_{2,y}. \tag{A.10}$$

The schematics in Fig. A.2 illustrate two different scenarios resulting from the previous computation of the displacement of the two sides of the crack. One can determine

$$\phi = \arctan\left(\frac{\Delta y f_{12}}{\Delta x f_{12}}\right) \tag{A.11}$$

$$d = \sqrt{\Delta y f_{12}^2 + \Delta x f_{12}^2} \tag{A.12}$$

$$\delta = \frac{\pi}{2} - \phi - \alpha_{hor}. \tag{A.13}$$

δ can be negative if the right side of the crack slides downwards with respect to the left side and positive otherwise. Crack opening and crack sliding are given by

$$w = d \, \cos \delta \tag{A.14}$$

$$s = d \, \sin \delta. \tag{A.15}$$

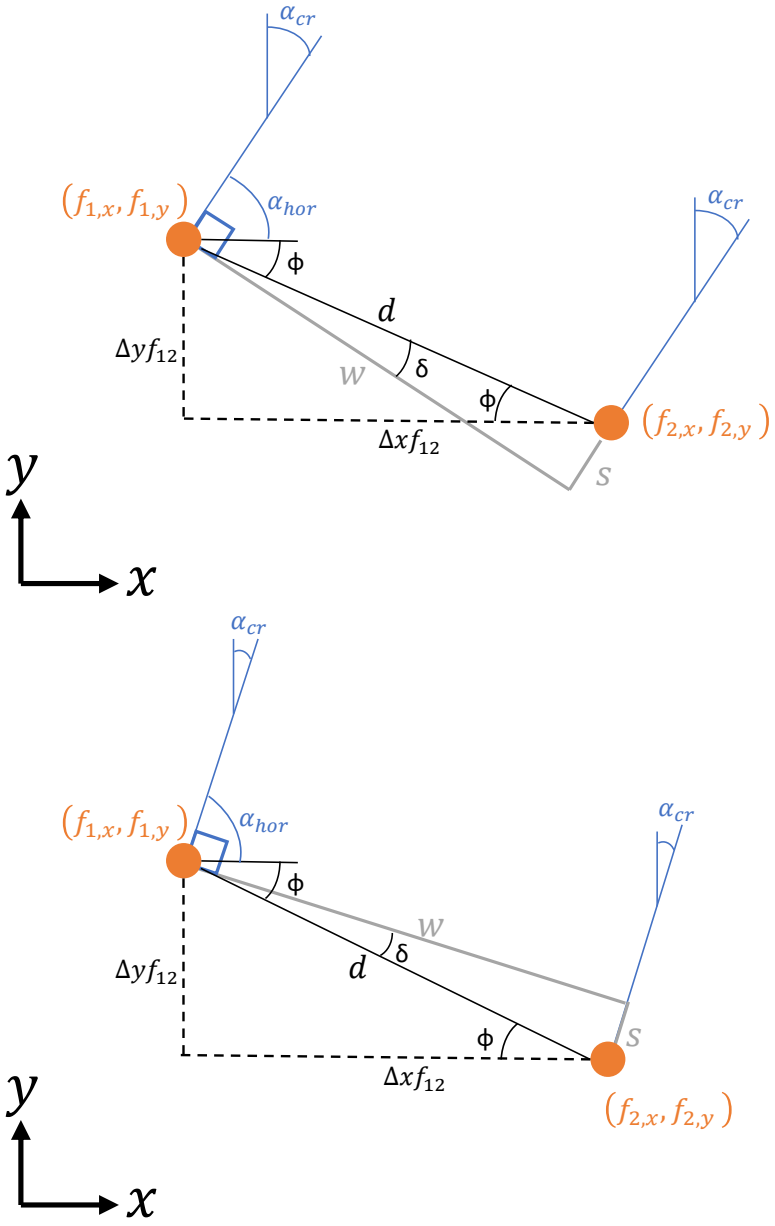

Figure A.2: Schematic for crack opening w and slip s calculation.

Bibliography

Blaber, J., & Antoniou, A. (2017). Ncorr instruction manual. http://www.ncorr.com/index.php/downloads. Accessed: 2019-05-03.

Calvi, P. M., Bentz, E. C., & Collins, M. P. (2017). Pure mechanics crack model for shear stress transfer in cracked reinforced concrete. ACI Structural Journal, 114, 545–554.

Campana, S., Anastasi, A., Ruiz, M. F., & Muttoni, A. (2013). Analysis of shear-transfer actions on one-way rc members based on measured cracking pattern and failure kinematics. Magazine of Concrete Research, 65(6), 386–404. doi:10.1680/macr.12.00142

Cavagnis, F., Ruiz, M. F., & Muttoni, A. (2018). An analysis of the shear-transfer actions in reinforced concrete members without transverse reinforcement based on refined experimental measurements. Structural Concrete, Journal of the fib, 19, 49–64. Retrieved from https://doi.org/10.1002/suco.201700145

Correlated Solutions. (n.d.). Strain calculation in vic-3d. www.correlatedsolutions.com/supportcontent/strain.pdf. Accessed: 2019-05-29.

Correlated Solutions. (2009). Digital image correlation : Overview of principles and software. https://www.researchgate.net/.../Correlated-Solutions-SEM-2009-DIC-overview.pdf. Accessed: 2019-04-20.

Correlated Solutions. (2014a). Application note - heat waves in digital image correlation.

Correlated Solutions. (2014b). Application note - subset, step size and strain filter selection.

Huber, P., Huber, T., & Kollegger, J. (2016). Investigation of the shear behavior of rc beams on the basis of measured crack kinematics. Engineering Structures, 113, 41–58.

Kupfer, H., Hilsdorf, H. K., & Rusch, H. (1969). Behavior of concrete under biaxial stresses. Journal Proceedings, 66(8), 656–666.

Lavision. (2015). Product-manual strainmaster. Göttingen, Germany.

Li, B., Maekawa, K., & Okamura, H. (1989). Contact density model for stress transfer across cracks in concrete. Journal of Faculty of Engineering, The University of Tokyo, 40, 9–52.

Mihaylov, B. I., Bentz, E. C., & Collins, M. P. (2013). Two-parameter kinematic theory for shear behavior of deep beams. ACI Structural Journal, 110, 447–456.

Mihaylov, B. I., Hannewald, P., & Beyer, K. (2016). Three-parameter kinematic theory for shear-dominated reinforced concrete walls. Journal of Structural Engineering, 142. Retrieved from https://doi.org/10.1061/(ASCE)ST.1943-541X.0001489

Mihaylov, B., Liu, J., & Lobet, R. (2018). A kinematic approach for the complete shear behavior of short frc coupling beams. ACI Structural Journal, 328. Retrieved from http://hdl.handle.net/2268/221360

Ponthot, J.-P. (2016). F.e.m. - chapter 10 kinematically admissible finite elements. Belgium: University of Liège.

Popovics, S. (1973). A numerical approach to the complete stress-strain curve of concrete. Cement and Concrete Research, 3, 583–599. Retrieved from https://doi.org/10.1016/0008-8846(73)90096-3

Ruiz, M. F., Muttoni, A., & Gambarova, P. G. (2007). Relationship between nonlinear creep and cracking of concrete under uniaxial compression. J. Adv. Concr. Technol. 5, 383–393. doi:10.3151/jact.5.383

Vecchio, F. J., & Collins, M. P. (1986). The modified compression-field theory for reinforced concrete elements subjected to shear. ACI Journal, 83(2), 219–231.

Walraven, J. C. (1980). Aggregate interlock : A theoretical and experimental analysis. Netherlands: Delft University of Technology.